INVESTIGATING THE ROLE OF BECN2 CCD INTERACTIONS IN CANONICAL AND NON-CANONICAL AUTOPHAGY

A Dissertation
Submitted to the Graduate Faculty
of the
North Dakota State University
of Agriculture and Applied Science

By

Elizabeth Ann Bueno

In Partial Fulfillment of the Requirements
for the Degree of
DOCTOR OF PHILOSOPHY

Major Department:
Chemistry and Biochemistry

June 2023

Fargo, North Dakota

North Dakota State University
Graduate School

Title

INVESTIGATING THE ROLE OF BECN2 CCD INTERACTIONS IN CANONICAL AND NON-CANONICAL AUTOPHAGY

By

Elizabeth Ann Bueno

The Supervisory Committee certifies that this ***disquisition*** complies with North Dakota State University's regulations and meets the accepted standards for the degree of

DOCTOR OF PHILOSOPHY

SUPERVISORY COMMITTEE:

Dr. Sangita Sinha
Chair

Dr. Christopher Colbert

Dr. Kenton Rodgers

Dr. Estelle Leclerc

Approved:

03/07/2024
Date

Dr. Gregory Cook
Department Chair

ABSTRACT

Autophagy is a conserved cell-survival pathway wherein old, damaged or harmful cellular components are surrounded by a double membrane vesicle called the autophagosome for lysosomal degradation and recycling. All eukaryotes have a conserved BECN homolog, a key coiled-coil domain (CCD)-containing autophagy protein. Mammals are unique as they have two BECN homologs, BECN1 and BECN2, both of which have the same domain architecture and function in autophagy. BECN2 has been shown to also function in non-canonical autophagy. My research focused primarily on investigating selected interactions of the BECN2 CCD.

We investigated interactions of the BECN2 CCD with two CCD-containing proteins known to bind to BECN1: UVRAG, an important autophagy protein, and TAB2, a protein important for inflammatory responses. We show that the BECN2 and UVRAG CCDs interact, but were unable to purify stable complexes for structural studies. In comparison, the CCDs of BECN2 and TAB2 bind with an affinity tighter than that of BECN2 homodimerization, forming a well-folded elongated heterodimer. These preliminary results provide information regarding interactions that enable BECN2 to regulate autophagy, in a manner analogous to BECN1.

We also show that, unlike BECN1, BECN2 facilitates non-canonical autophagy involving ATG9A-bearing vesicles, via interactions with the STX6 SNARE domain. We show that the STX6 SNARE domain binds to BECN2 residues 181-250 (BECN2(181-250)) within the BECN2 CCD. The STX6 SNARE is disordered in the absence of interacting partners but becomes helical when in complex with BECN2. The BECN2(181-250):STX6 SNARE complex is also more stable than either the BECN2(181-250) or the BECN2 CCD homodimer. We determined the 2.65 Å X-ray crystal structure of the STX6 SNARE bound to BECN2, showing that the complex is a heterotrimeric helical bundle, consisting of one helix comprising BECN2(181-250) and two

STX6 SNAREs that are anti-parallel to each other. The heterotrimer interface is stabilized by 15 layers of three residues, each contributed by a different helix, of which, six layers are entirely hydrophobic, including two consisting of three leucines each. We verified the importance of these hydrophobic layers using point mutations and affinity pulldowns, showing that mutations of the hydrophobic layers either significantly or completely disrupt the interaction between BECN2(181-250) and STX6 SNARE domain. This 3-helix bundle likely represents an intermediate during the formation of the full SNARE complex, thereby providing mechanistic insights into the process by which ATG9A-bearing vesicles transport lipids to the growing phagophore.

Together these studies help explain the role of the BECN2 CCD in canonical and non-canonical autophagy, providing clues as to why mammals have two BECN paralogs.

ACKNOWLEDGMENTS

I am grateful to my adviser Dr. Sangita Sinha for her support, guidance, and mentorship. She helped me become a better scientist.

I would also like to thank my committee members Dr. Christopher Colbert, Dr. Kenton Rodgers, and Dr. Estelle Leclerc. Dr. Colbert is also a collaborator of our lab, I would like to express thanks for the guidance and feedback from lab meetings and the one-on-one meetings.

I would extend my thanks to our collaborator Dr. David Belnap from the University of Utah. For setting up the Cryo-EM grids and obtaining the micrographs used in this dissertation. Also for all the advice and support in analyzing the data.

I would like to extend my thanks to my previous and current lab members of the Sinha lab, including Dr. Karen Glover, Dr. Yue Li, Dr. Shreya Mukhopadhyay, Dr. Srinivas Dasanna, Samuel Wyatt, Robyn Duttenhefner, Subeksha Subedi, and Tyeaba Dipti and from the Colbert lab Dr. Jaime Jensen, Dr. Shane Wyborny, Benjamin LeVahn, Dr. Beau Jernberg, Tajnin Sultana, Victor Arnold, and Robin Kutsi. Thank you for your support and guidance inside and outside the lab. Thank you for making the lab a joyful and friendly place. I am so grateful that I had all of you as my lab mates throughout my years here.

This work was supported wholly or in part by NIH grants to SCS: R15 GM146232, R15 GM122035, a National Science Foundation grant MCB-1413525. Work performed at Bio-CAT was supported by NIH NIGMS 9P41 GM103622 and use of the Pilatus 3 1M detector funded by NIH NIGMS 1S10OD018090-01. This work incorporates research conducted at the APS NE-CAT beamlines, which are funded by NIH NIGMS P41 GM103403. This research used resources of the APS, a US DOE Office of Science User Facility operated for the DOE Office of Science by Argonne National Laboratory under Contract No. DE-AC02-06CH11357.

DEDICATION

For my Husband, Fernando, who has supported me, loved me, continued to motivate me, and kept me sane.

For my parents, who have always supported my dreams and pushed me to achieve them.

For my brother and sister-in-law, for the love and support even through their own struggles.

For my inspiration, you will forever be missed.

TABLE OF CONTENTS

LIST OF TABLES

LIST OF FIGURES

LIST OF ABBREVIATIONS

AFM.....Aromatic finger mutation

ANL .....Argonne National Laboratory

APS .....Advanced Photon Source

Atg .....Autophagy-related genes

BARAD.....β-α-repeated autophagy-specific domain

Beclin/BECN .....Bcl-2 interacting protein 1

BH3D .....BCL2 homology 3 domain

CCD .....Coiled-coil domain

CD.....Circular dichroism

D_{max} .....Maximum particle dimension

DTT.....Dithiothreitol

EM.....Electron microscopy

FHD.....Flexible helical domain

GST .....Glutathione S-transferase

His_6.....Hexa-histidine

HOPS .....Homotypic fusion and protein sorting complex

IDR.....Intrinsically disordered region

IL-1 .....Interleukin-1

IPTG.....Isopropyl thio-β-D-galactoside

IR.....Infrared

ITC .....Isothermal titration calorimetry

K_a .....Association constant

MAD .....Multi-wavelength anomalous dispersion

MEKK3 .....Mitogen-activated protein kinase kinase kinase 3

MIR .....Multiple isomorphous replacement

MR .....Molecular replacement

MST .....Microscale Thermophoresis

n.....Stoichiometry

P(r) .....Pairwise-distance distribution function

PI3KC3 .....Class III phosphatidylinositol-3-kinase

R_{free}.....Free R-factor

R_g.....Radius of gyration

R_{work} .....Work R-factor

SAXS .....Small Angel X-ray Scattering

SEC .....Size exclusion chromatography

STX.....Syntaxin

TAB2 and TAB3.....TAK1 binding protein 2 and 3

TAK1 .....Transforming growth factor β-activated kinase 1

TEV.....Tobacco etch virus

TFE .....2,2,2- Trifluoroethanol

T_m.....Melting temperature

TNF .....Tumor necrosis factor-α

ULK .....Unc-51-like kinase

UVRAG .....UV radiation resistance-associated gene

VPS .....Vacuolar protein sorting protein

βME .....B-mercaptoethanol

ΔH .....Change of enthalpy

CHAPTER 1. INTRODUCTION

1.1. Autophagy

Autophagy, which means 'self-eating' is a cell-survival pathway conserved in all eukaryotes[1,2]. Autophagy involves the engulfing of cellular components including old or damaged proteins, organelles, and pathogens, in double-membraned vesicles called autophagosomes, prior to the fusion with the lysosomes that leads to the degradation and recycling of the contents[1]. A basal level of autophagy is needed to keep cells at homeostasis. During stress conditions such as nutrient deprivation and intracellular stress like the accumulation of damaged proteins, autophagy is upregulated leading to the recycling of nutrients and energy[1]. Autophagy plays a role in many physiological and pathophysiological processes like aging, immunity and differentiation, and development[1, 2]. Autophagy also plays a crucial role in many diseases like cancers, neuronal degeneration, liver disease, and heart disease[2, 3, 4]. Within these diseases, autophagy can lead to either a beneficial or negative effect[3]. The autophagy pathway has been broken down into multiple steps (Figure 1.1), 1) initiation signaling 2) vesicle nucleation, 3) vesicle elongation, and 4) autophagosome maturation[5]. After the initiation signaling, vesicle nucleation leads to the formation of autophagosomes, after which the autophagosome elongates around the cargo selected for degradation. After autophagosome formation, it fuses to the lysosome in a step called autophagosome maturation[6] which leads to the degradation of the sequestered cargo.

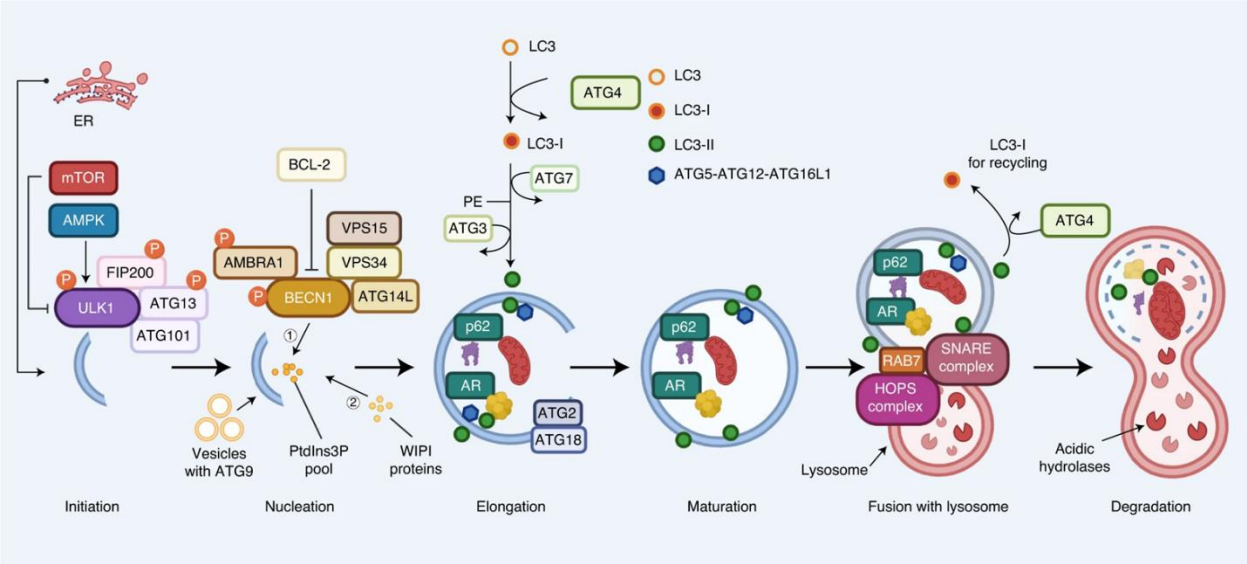

Figure 1.1: Steps of Autophagy. After the initiation of autophagy, the isolation membrane begins to form in the vesicle nucleation step. The vesicle then elongates around the sequestered content, to form the autophagosome. After the formation of the autophagosome or maturation, the autophagosome fuses with the lysosome to form the autolysosome. Within the autolysosome the degradation of the sequestered content takes place. This figure was adapted from Aman Y, et. al [7].

Each of these different steps of the autophagy pathway is highly regulated and involves different protein complexes. The initiation signal of autophagy is regulated by the Unc-51-like kinase (ULK) complex that consists of ULK1 or ULK2, Autophagy-related genes (Atg)13, and RB1-inducible coiled-coil protein 1. This complex is further regulated by the mechanistic target of rapamycin complex 1, which during nutrient-rich conditions associates with and inhibits the Unc-51-like kinase ULK complex and during starvation conditions dissociates from the ULK complex. In the vesicle nucleation step, the class III phosphatidylinositol-3-kinase (PI3KC3) complex helps regulate the formation of the autophagosome. The PI3KC3 complex 1 contains vacuolar protein sorting protein (VPS)34, VPS15, Bcl-2 interacting protein 1 (Beclin 1/BECN1), and ATG14, while complex 2 contains the same proteins except ATG14 is replaced with UV radiation resistance-associated gene (UVRAG). For the elongation step of the autophagy pathway, the complex of Atg12-Atg5-Atg16 is needed for the regulation of the elongation of the

autophagosome[1, 6]. Autophagosome maturation, i.e. fusion of the autophagosome to the lysosome to form the autolysosome involves the homotypic fusion and protein sorting (HOPS) complex, a SNARE complex, and the PI3KC3 complex 2. The HOPS complex consists of the VPS11, Vps16, VPS18, Vps33A, VPS39, and Vps41 proteins. The other complex shown to function in the autophagosome maturation is a SNARE complex that contains syntaxin (STX)17, SNAP29, VAMP7, or VAMP8[8]. All of these different complexes have other proteins that help regulate autophagy, by interacting with proteins within the complex to either up- or down-regulate autophagy.

1.2. Non-Canonical Autophagy

The autophagy pathway described above is also known as canonical autophagy. There is another type of autophagy known as non-canonical autophagy, in which proteins are still sequestered and degraded and recycled back to the cell[9]. Non-canonical autophagy does not need all the proteins that are needed in canonical autophagy (Figure 1.2). Non-canonical autophagy can bypass ATG5, ATG7, and LC3 which are needed for the elongation and closure of the autophagosomes. Non-canonical autophagy can also bypass the proteins needed for the initiation and nucleation of the autophagosomes, such as the UKL1 complex, and BECN1 as well as other proteins in the PI3KC3 complex. The autophagosomes formed in non-canonical autophagy can be from elongated from lipids from multiple membranes[10].

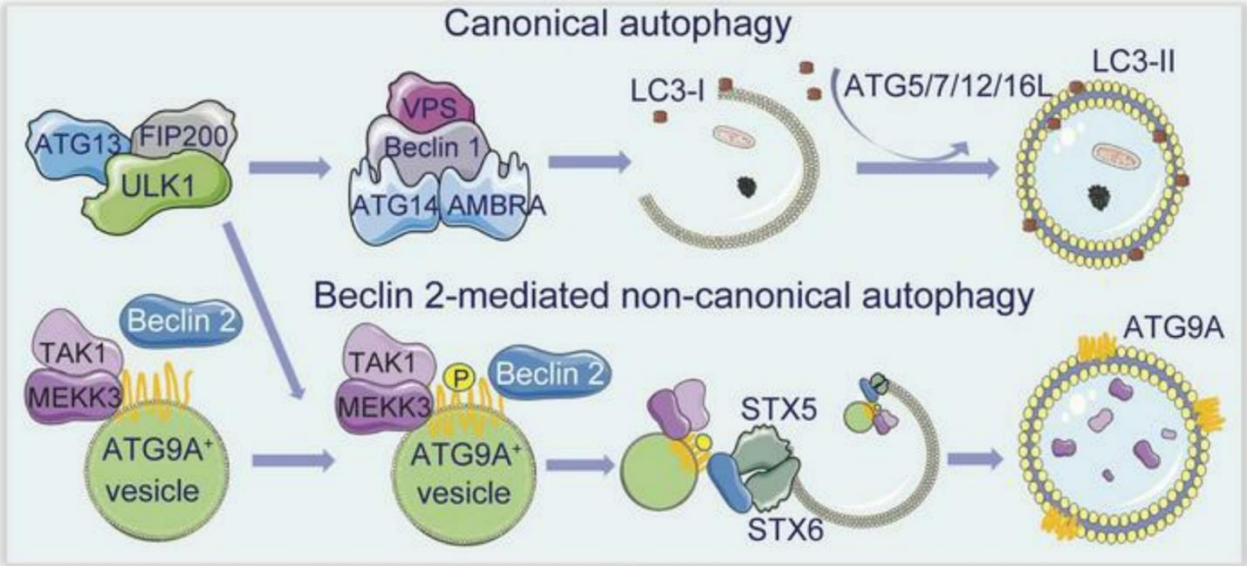

Figure 1.2: Comparison of canonical autophagy and non-canonical autophagy. Top showing canonical autophagy and proteins needed. The bottom showing BECN2 mediated non-canonical autophagy and showing that known proteins for canonical autophagy are not needed. Figure was adapted from Zhu, M. et al[11].

1.3. BECN1

BECN1, which is expressed in all cells, was first discovered as a Bcl-2 interacting protein 1[12]. BECN1 is a part of the PI3KC3 complex and was the first mammalian protein shown to function in autophagy[13]. BECN1 homologs are conserved in all eukaryotes, called BECN1 in mammals, VPS30/ATG6 in yeast, and ATG6 in plants[14]. Mutations or changes in expression levels of BECN1 are associated with various diseases. BECN1 has been shown to be a tumor suppressor in cancers[13, 14]. 40-75 % of breast, ovary, and prostate cancer have a monoallelic deletion of BECN1. A deficiency or malfunction of BECN1 is also implicated in neurodegenerative disorders like Alzheimer's and Parkinson's. Some viruses target BECN1 to evade autophagic degradation, like the human immunodeficiency virus, and the γ-herpesvirus. As mentioned before BECN1 is a part of the PI3KC3 complex that functions in the autophagosome nucleation stage of the autophagy pathway[14].

Human BECN1 is a 450-residue protein that contains an intrinsically disordered region (IDR, residues 1-140), a flexible helical domain (FHD, residues 141-171), a coiled-coil domain (CCD, residues 175-265), and a β-α-repeated autophagy-specific domain (BARAD, residues 266-450). Within the IDR is a BCL2 homology 3 domain (BH3D, residues 105-130) that becomes helical upon binding to a BCL2 homolog. The BH3D has been shown to interact with many anti-apoptotic BCL2 homologs, including viral BCL2 homologs such as M11 from the γ-herpesviruses 68[15]. The BECN1 CCD has been shown to form an anti-parallel left-handed coiled-coil homodimer[14]. The BECN1 CCD has also been shown to form a parallel heterodimer with ATG14 and UVRAG, which are a part of the PI3KC3 complex 1 and 2 respectively[14, 16]. These interactions have been shown to interact via the BECN1 CCD and the CCD of ATG14 and UVRAG. The BECN1 CCD homodimerizes at a lower affinity than the binding of BECN1 CCD to ATG14 CCD or to the UVRAG CCD[16]. The BECN1 CCD has also been shown to interact with Transforming growth factor β-activated kinase 1 (TAK1) binding protein 2 and 3 (TAB2 and TAB3) via their CCDs. TAB2 and TAB3 inhibit autophagy when bound to BECN1[17]. The BARAD comprising of residues 266-450, has a novel protein fold that contains three sets of an anti-parallel, three-stranded, β-sheet followed by an α-helix[18]. Residues 248-264, comprising the last 18 residues of the CCD, have been named the overlap helix, as it has been crystallized in two different alternate packing states: as part of the anti-parallel CCD homodimer or packed against the BARAD[19]. Thus, these interactions with BECN1 help to show how BECN1 functions in the regulation of autophagy.

1.4. BECN2

Unlike other eukaryotes, mammals have two BECN homologs, BECN1 and BECN2. BECN2 is expressed in select tissues including the brain, skeletal muscle, placenta, thymus, and

uterus. Human BECN1 and BECN2 share 57% sequence identity (Figure 1.3), while mouse BECN1 and BECN2 share 44% sequence identity. Human BECN2 and mouse BECN2 shares a 52.6% sequence identity, while human BECN2 and pig BECN2 shares a 59.4% sequence identity and mouse BECN2 and pig BECN2 shares a 50.1% sequence identity (Figure 1.4).

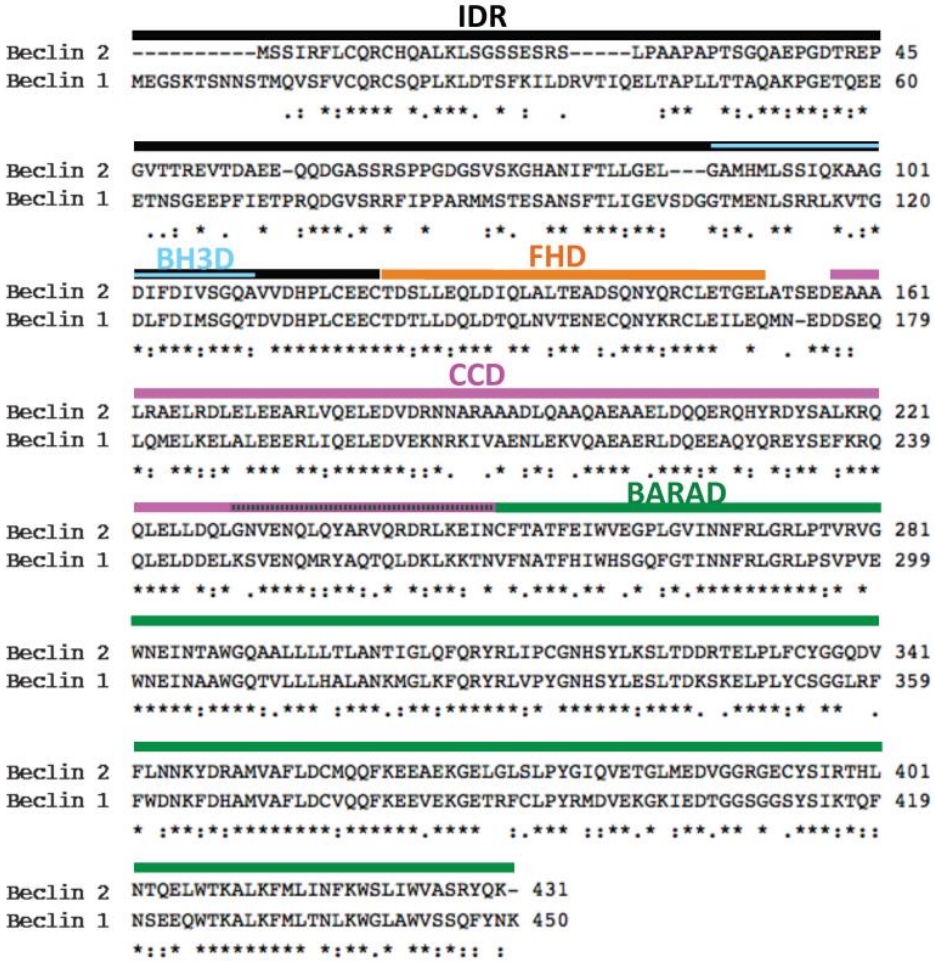

Figure 1.3: Sequence alignment of BECN2 and BECN1. Domains are indicated above the sequence. This figure was adapted from[20].

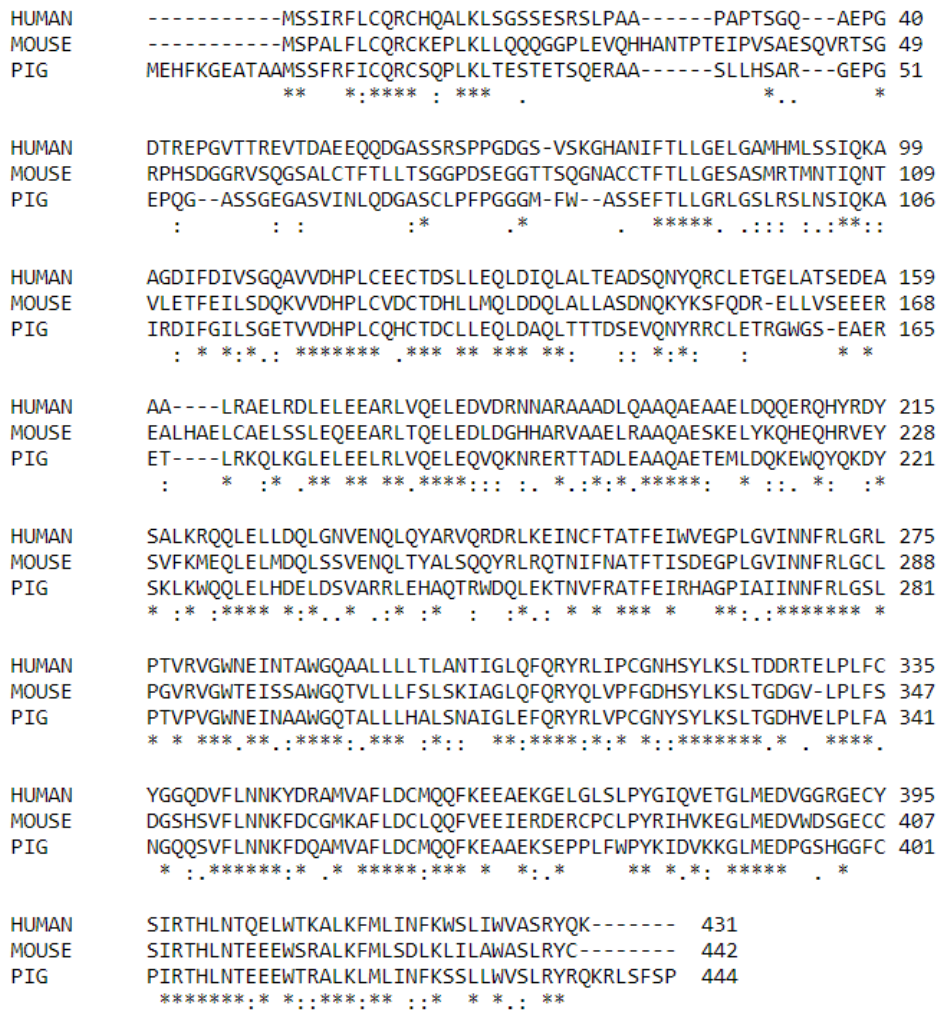

Figure 1.4: Sequence alignment between BECN2 found in Human, Mouse, and Pig. Asterisks represent identical residues, while double and single dots represent decreasing sequence conservation.

Human BECN2 is a 431 amino acid protein[21]. BECN1 and BECN2 have similar domain architecture including the IDR (residues 1-121), the FHD (residues 122-152), the CCD (residues 158-250), and the BARAD (residues 251-431) (Figure 1.3). Residues 88-111 of the IDR of BECN2 are equivalent to the BH3D of BECN1. Similar to BECN1, the BECN2 CCD forms an anti-parallel coiled-coil homodimer (Figure 1.5.A and 1.5.B). Unlike the BECN1 CCD homodimer, the BECN2 CCD forms a curved coiled-coil with a curvature of 15 nm radius

(Figure 1.5.C). The BECN2 CCD homodimer has a self-dissociation constant of 138 µM compared to the BECN1 CCD homodimer self-dissociation constant of 48 µM[20].

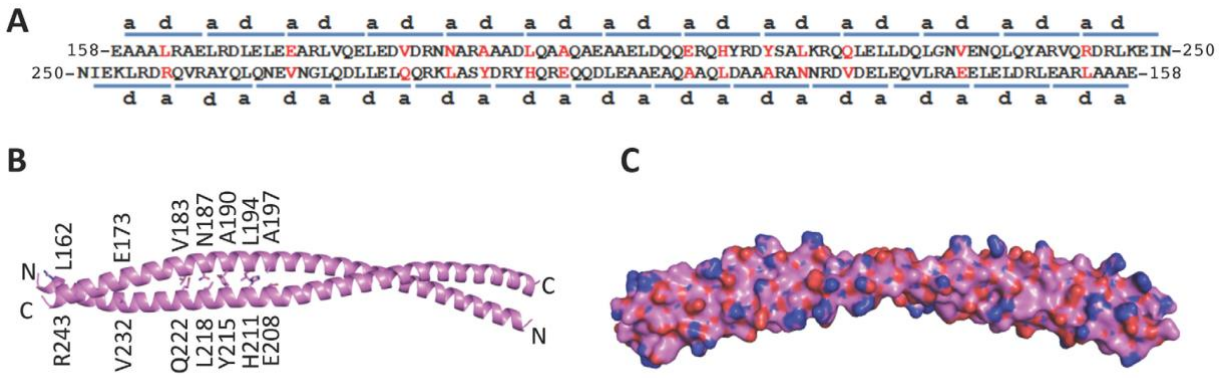

Figure 1.5: The BECN2 CCD homodimer. A) The paired residues of the anti-parallel BECN2 CCD homodimer. B) The X-ray crystal structure of the BECN2 CCD homodimer is shown as a ribbon, with the non-ideal packing interface residues shown. C) The surface representation showing the curvature of the homodimer with the atoms colored by type – oxygen red, nitrogen blue, and carbon violet. This figure was adapted from[20].

1.4.1. Functions of BECN2

Like BECN1, BECN2, also functions in autophagy in both basal conditions and starvation conditions[21]. Unlike BECN1, BECN2 also functions in pathways that are not related to autophagy. For example, BECN2 functions in agonist-induced lysosomal degradation of G protein-coupled receptors, and this does not involve BECN1 or other BECN1 interacting proteins[21]. BECN2-dependent endolysosomal trafficking and degradation of Kaposi's sarcoma-associated herpesvirus's G protein-coupled receptors shows that BECN2 plays a role in endolysosomal trafficking and tumor suppression[22]. BECN2 has also been shown to function in cocaine-induced behaviors, cocaine-amplified dopamine release, and kinase signaling, and in dopamine neurons, BECN2 plays a critical role in regulating cocaine responses[23]. BECN2 functions as a negative regulator of innate immune signaling by controlling the expression of some proinflammatory cytokines[24]. BECN2 plays a role in the negative regulation of

inflammasome activation, the deletion of BECN2 increases the activities of inflammasomes, and the overexpression of BECN2 suppress the inflammasome activitation[25]. Therefore, it has been shown that BECN2 functions in autophagy similar to BECN1, but BECN2 also functions in other pathways that are not related to autophagy and are not dependent on BECN1.

1.4.2. Interactions of BECN2

BECN2 has been shown to interact with many of the same proteins that interact with BECN1 and function in autophagy, but it also has some unique interactions. Like BECN1, BECN2 interacts with UVRAG[21], and ATG14[20, 21]. However, BECN2 interacts with STX5 and STX6[24, 25], whereas BECN1 does not appear to interact with these proteins.

The BECN2 and ATG14 CCDs form a parallel heterodimer with a binding affinity of 0.22 μM, which is approximately 600-fold tighter than the BECN2 CCD homodimer[20], and is also tighter than the binding of the BECN1 CCD to the ATG14 CCD interaction[14, 20]. UVRAG has been shown to interact with BECN2 through Coimmunoprecipitation experiments, but this interaction has not been further characterized[21]. Coimmunoprecipitation experiments have shown that BECN2 interacts with both STX5 and STX6, but this interaction appears to not be required for canonical autophagy. The domains and the interaction between BECN2 and these other proteins shown to interact have yet to be investigated. Further studies need to be done to determine how these proteins interact with BECN2 and how these interactions function in autophagy or other pathways not related to autophagy.

1.5. Overview of Methods Used for This Research

1.5.1. Isothermal Titration Calorimetry (ITC)

ITC is a useful technique for measuring the thermodynamics of a binding reaction, by monitoring heats of binding. ITC is a convenient technique as it does not require protein

immobilization or labeled protein and it uses a small amount of protein[26]. All ITC experiments described in this dissertation were performed on a Low Volume Nano ITC from TA instruments, which can determine dissociation constants from 10^{-9}-10^{-4} M and detect heats from 0.05-5000 µJ[26]. There are two identical cells in the calorimeter, a sample cell and a reference cell, which are kept at a constant temperature (Figure 1.6). As the molecule titrated into the sample cell, dissociated or binds to the molecules in the sample cell, heat may be released or absorbed. The calorimeter provides power to heat or cool the sample cell to maintain a constant temperature relative to the reference cell, resulting in the titration curve of the heater power vs time (Figure 1.6)[27].

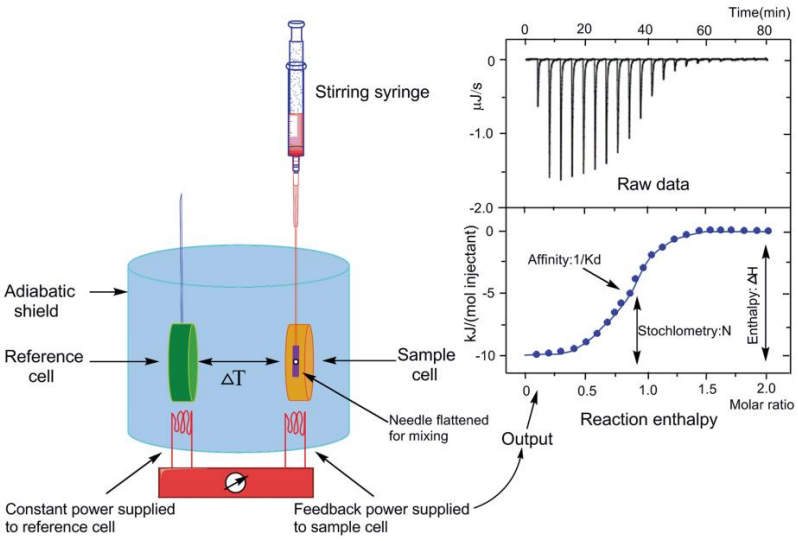

Figure 1.6: Basic principle of ITC. Left: the schematic of the ITC instrument. Right: the raw data (top) an example of the titration experiment (bottom) the fit to an independent interaction model. This figure was adapted from[28].

Proper sample preparation is important to obtaining reliable ITC results. Proteins should be very pure as impurities can affect the heats of binding detected. Further, reliable protein concentrations should be determined as these are needed to calculate the thermodynamic parameters after fitting the data with the appropriate binding models. Both samples should be co-dialyzed against a selected ITC buffer to make sure proteins are fully buffer matched, to

guarantee that all heats being detected are from the binding or dissociation and not due to mixing of mismatched buffers. For binding interactions experiments, one protein is loaded into the syringe and titrated into the other protein in the cell. For dissociation experiments, the protein dimer is loaded into the syringe and titrated into a buffer in the cell. The area of the peak is then integrated and plotted versus the molar ratio of proteins in syringe to cell. The binding curve is then fitted to a binding model using NanoAnalyze software (TA Instruments, New Castle, US) to determine thermodynamic constants such as the enthalpy of interaction (ΔH), association constant (K_a), and stoichiometry (n) (Figure 1.6).

1.5.2. Microscale Thermophoresis (MST)

MST measures the movement of molecules in a microscopic temperature gradient. The change in molecular movement in the presence of increasing concentrations of ligand allows for the quantification of binding affinity of biomolecule interactions. MST requires smaller amounts of sample compared to ITC[29]. MST can be performed in almost any buffer, plasma, or cell lysate[30].

A binding constant is calculated by measuring the MST signal from multiple capillaries containing a constant concentration of fluorescent molecules mixed with an increasing concentration of ligand (by adding serial dilutions of the ligand). The MST experimental setup starts with an infrared (IR) laser being focused through the sample to cause a 2-6 °C change[29, 30] (Figure 1.7.B). This temperature gradient excites the fluorophores in the capillaries, with 10 to 16 capillaries used per binding constant experiment. The typical MST signal (Figure 1.7.C) shows the constant initial fluorescence before the IR-laser is turned on. After the IR laser is turned on there is a T-jump that shows the rapid change in movement of fluorophore, which is measured for 30 seconds which leads to the molecules reaching a near steady-state. After the IR

laser is turned off there is an inverse T-jump followed by back diffusion of the molecules[29, 30]. The change in the concentration of unbound and bound fluorescent molecule causes a change in the MST traces (Figure 1.7.D). The analysis of the MST traces is shown by plotting ΔF_{norm} vs concentration of Ligand. ΔF_{norm} is F_{hot}/F_{cold}. The plot of the ΔF_{norm} vs concentration of Ligand gives the binding curve from which the binding constant can be determined (Figure 1.7.D)[29, 30].

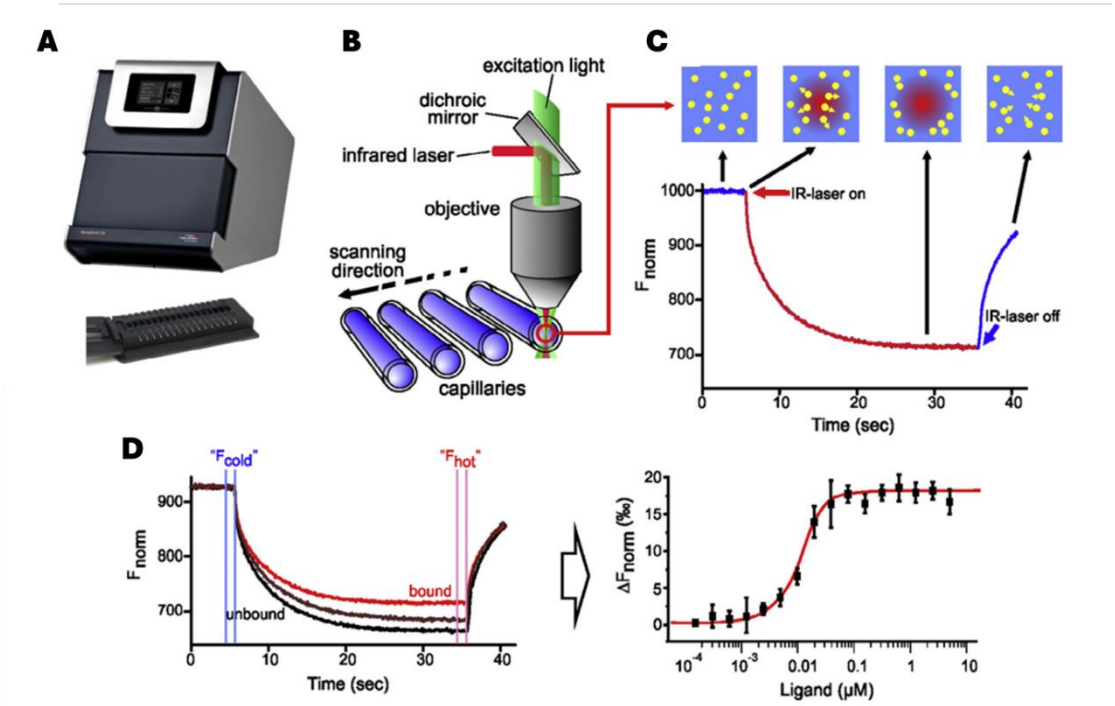

Figure 1.7: MST setup and experiment. A) Example of an MST machine. B) The IR laser passes through the capillaries. C) An example of the signal of an MST experiment. First the protein at a constant homogeneously distributed. Next the “T-jump" when the IR laser is turned on. Next, the fluorescent change was measured over 30 seconds. Finally, the IR laser is turned off, the inverse T-jump happens with the back diffusion. D) An example of a binding experiment. This figure was adapted from[30].

1.5.3. Circular Dichroism (CD) Spectroscopy

Amino acids, except glycine, are chiral and therefore are optically active, i.e they rotate polarized light due to the unequal absorption of left-handed and right-handed polarized light[31]. CD spectroscopy is normally used to estimate the secondary structure content, and folding of optically active molecules[31]. In the far-UV spectra (wavelengths below 250nm) there is an

optical transition due to the different geometric arrangement of the amides of the protein backbone in the different secondary structures. This leads to the characteristic CD spectra for the different types of secondary structures (Figure 1.8). Protein helices result in negative peaks at 222 nm and 208 nm and a positive peak at 193 nm; β-strands in a negative peak at 218 nm and a positive peak at 195 nm; and disordered peptides have low ellipticity above 210 nm and a negative peak near 195 nm[31]. For proteins that contain a mixture of secondary structures, the CD spectra will reflect a combination of the spectra that arises for each individual secondary structure[31]. Therefore CD spectra can be analyzed with programs like CDPro software package to determine the secondary structure content of proteins[32]. CD data is normally reported as a plot with the X-axis being wavelength (nm) and the Y-axis being the mean residue ellipticity with units of $^\circ M^{-1} m^{-1}$/residue[31].

CD Spectroscopy can also be used to study the thermal stability of folded proteins. As proteins are heated, they lose the characteristic CD spectra that arises from their α-helical or β-strand content, changing toward spectra characteristic of disordered proteins[33]. Since the CD spectra have a significant negative peak at 222 nm and 218 nm for α-helical and β-strand proteins respectively (Figure 1.8), these wavelengths can be monitored to track thermal unfolding as disordered proteins lack ellipticity at these wavelengths. The melting temperature (T_m) of a protein can be determined by fitting the melting curve with a Boltzmann model to calculate the midpoint of the sigmoid. The unfolding can be reversible or irreversible but in both cases, the thermal stability can still be determined[33].

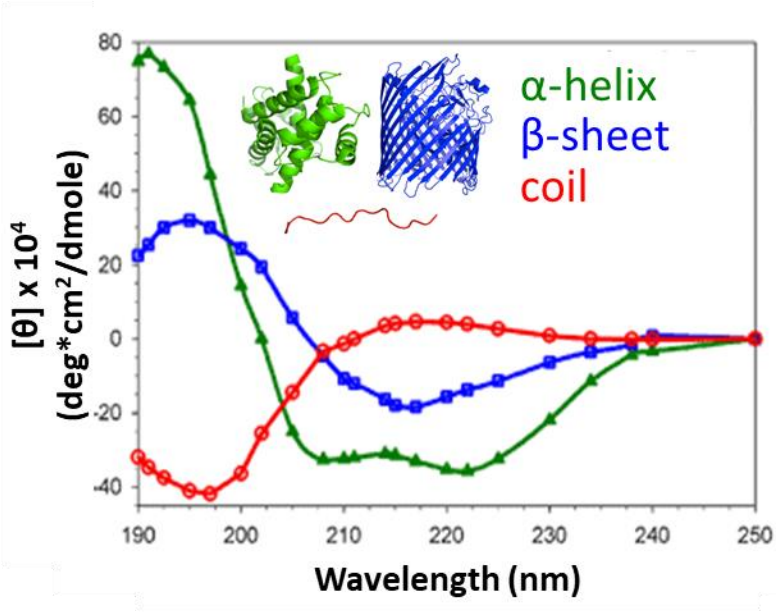

Figure 1.8: The CD Spectra of proteins composed of different secondary structures. Green shows a spectrum of a protein containing primarily α-helical content. Blue shows a spectrum of a protein containing primarily β-sheet content. Red shows a spectrum of a protein containing all random coil. This figure was adapted from "Experimental methods to study protein structure and folding" published by Louise McBride at SlidePlayer.

1.5.4. Small Angle X-ray Scattering (SAXS)

SAXS is a powerful method used to obtain low-resolution three-dimensional structures of macromolecules in solution, which is useful for determining folding state, shape, conformation, and oligomerization[34]. Therefore, SAXS is an important method for obtaining solution structure information for proteins that do not crystallize.

In SAXS, the protein sample in solution is exposed to the X-ray source and the scattering signal comes from the difference in average electron density of the protein sample and the bulk solvent. The scattering curve I(q) is a function of momentum transfer q. $q= (4\pi\sin\theta)/\lambda$, where 2θ is the angle between the incident and scattered bean, and λ is the wavelength of the X-ray beam[34]. The scattering curve resulting from this subtraction of scattering from the buffer alone from that containing the sample, is an isotropic scattering curve due to the random orientation of the protein in the solution. The scattering intensity can be written as:

$$I(q) = \langle I(q) \rangle_{\Omega} = \langle A(s) A^{*}(s) \rangle_{\Omega} \quad (1.1)$$

In equation 1.1, the intensity is averaged over all orientations (Ω). A(s) is the scattering amplitude, which is a Fourier transformation of the excess scattering length density.

Analyses of the scattering curve can be used to determine protein homogeneity, average radius of gyration (R_g), pairwise-distance distribution function (P(r)), maximum particle dimension (D_{max}), and the folding state.

A Guinier analysis is performed to extract the information of the intensity at 0 θ, I(0), and the R_g. the Guinier equation can be written as:

$$I(q) = I(0) exp\left(-\frac{1}{3} R_g^2 s^2\right) \quad (1.2)$$

The Guinier plot of ln(I) versus q^2 is used to determine the protein homogeneity and R_g[34]. A linear Guinier plot in the lower q range shows that the sample is homogenous and monodispersed, while curvature in the Guinier plot indicates that the sample is aggregated (Figure 1.9)[35]. R_g is the average root-mean-square distance to the center of density. Therefore, for proteins of the same mass, the R_g is smaller for a compact protein, than for an elongated protein[36].

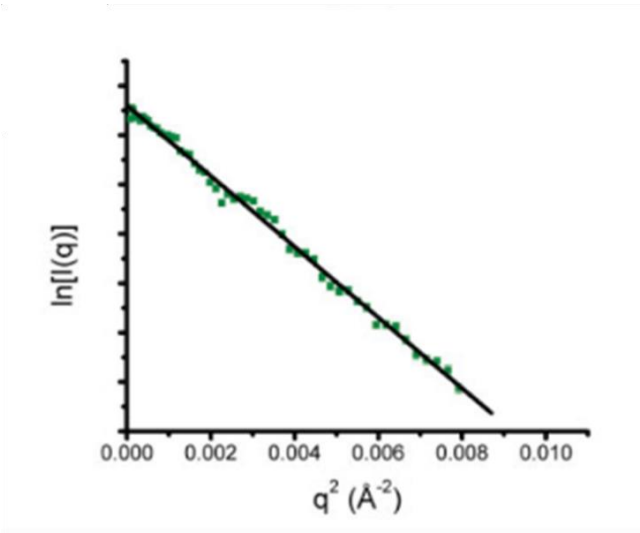

Figure 1.9: An example of a Guinier plot of a homogenous, and monodispersed sample. This figure was adapted from the website: https://bioxtas-raw.readthedocs.io/en/latest/saxs/saxs_guinier.html.

The distance distribution function, P(r) can be derived from the Fourier transformation of the scattering data:

$$P(r) = \frac{r^2}{2\pi^2}\int_0^\infty s^2 I(s)\frac{\sin sr}{sr}\,ds \qquad (1.3)$$

The P(r) is calculated by the Fourier transform of the scattering curve and provides information about the distance between electrons in the scattering particles. The P(r) plot can be used to estimate the molecule's D_{max}, i.e. the maximum dimension of the molecule which is determined from the point where the P(r) approaches zero[34]. The P(r) plot also provides information about the shape of the protein, with globular proteins displaying a bell curve with the maximum at $D_{max}/2$, and an elongated protein showing an asymmetric curve with the maximum being at the smallest distances of the protein (Figure 1.10)[35].

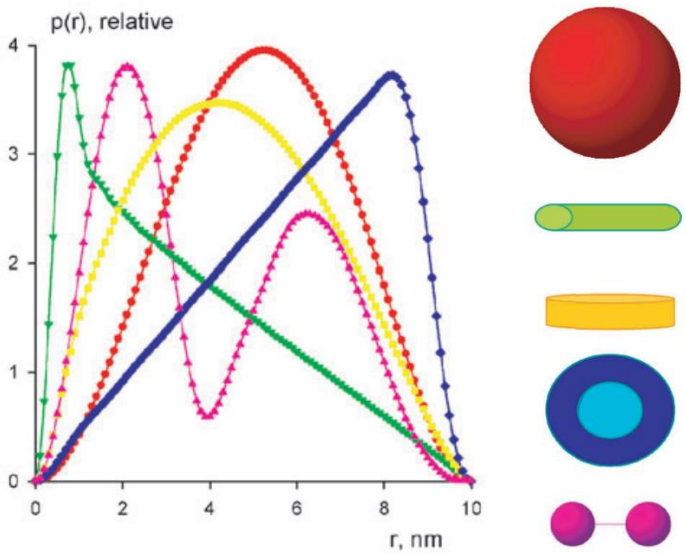

Figure 1.10: P(r) curves and the protein shapes that correspond. Curves for globular protein (Red), elongated protein (green), disk-shaped protein (yellow), hollow sphere (blue), and dumbbell-shaped protein (magenta). This figure was adapted from Dmitri, I et al.[35].

The Kratky plot (Figure 1.11), calculated directly from the scattering curve, provides information about the folding of the protein.

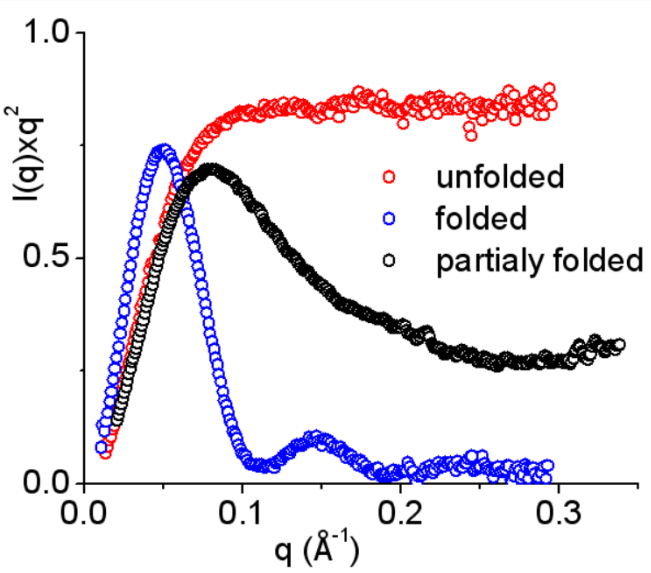

Figure 1.11: Sample Kratky plots showing the different folding states. The curve for disorder (red), partially folded (black), and refolded (blue). This figure is adapted from a 2012 Bruker lecture: An overview of biological SAXS: instrumentation, techniques, and applications.

The Kratky Plot for a well-folded protein, has a peak at low q with the curve returning to baseline. For a partially folded protein, has a peak at low q with the curve not returning to baseline and for a disordered protein, there is a plateau-shaped curve[34]. The Kratky plots displays a mixture of the plots for folded and unfolded proteins in the case of proteins containing multiple domains with disordered regions (Figure 1.11).

An *ab initio* molecular envelope of the protein can be generated from the scattering data. These structures are generated using programs such as DAMMIF[37] which model the protein as many densely packed beads inside a certain search volume. Next, the DAMAVER[38] program is used to calculate the average of multiple runs of the same model. SUPCOMB[39] is then used to fit protein with known atomic structure within this molecular envelope. A good fit can provide information about the oligomerization state or the domain arrangement of proteins[35].

1.5.5. Protein X-ray Crystallography

Protein X-ray crystallography enables determination of high-resolution three-dimensional structures of proteins and protein complexes. The atomic details of the structure provides information about protein function and details of protein-protein interactions. This is a powerful technique that helps in the understanding the structural function of proteins and protein complexes. However, X-ray crystallography only gives structural information about proteins that crystallize therefore the technique is not useful for proteins that are not well-ordered as flexibility typically prevents crystals from diffracting to atomic resolution.

A highly pure and homogeneous protein sample is needed to form protein crystals for protein X-ray crystallography. Crystallization takes place by bringing a protein solution to supersaturation, such that a slight change of solution conditions will cause the protein to come out of solution in the form of either a crystal nucleus that can grow into larger crystals or often

and undesirably precipitate. Many conditions can affect the crystallization including protein concentration, precipitant (i.e. Polyethylene glycol) type and concentration, buffer type and pH, temperature, and additives (i.e. amino acids)[40,41]. Therefore, to obtain diffraction quality crystals, crystallization conditions needs to be optimized. A commonly used crystallization technique is vapor diffusion where the protein solution is mixed with reservoir solution (mixture of buffer, salt, precipitant, crystallization additive, etc.) and placed over a reservoir of the reservoir solution until the drop reaches a vapor equilibrium with the reservoir. The drop containing the protein has a lower concentration of the reservoir solutes, leading to water vapor evaporation from the drop, causing an increase in the protein and solute concentration in the drop. This concentration increase can lead to the crystal formation and growth[41].

The crystal is exposed to a monochromatic X-ray beam to collect X-ray diffraction data. There are two ways of generating this X-ray beam - either by electrons striking a rotating copper anode or from electrons accelerating in a synchrotron storage ring, with the absorption of unwanted wavelengths. X-ray beams generated by a synchrotron are more intense, therefore needs shorter exposure times and have a higher signal-to-noise ratio, leading to higher resolution diffraction data. Diffraction data is normally collected at 100 K to reduce radiation damage, by mounting the crystal in a stream of cold liquid nitrogen. The X-rays are scattered by the electrons in the crystals and the diffracted X-ray are recorded by the detector as spots called reflections[41]. Between exposures of the protein crystal to the X-ray beam it is rotated, recording a set of numerous diffraction images, at different degrees of rotation.

The reflections are assigned to the Miller indices, which consists of three integers *h, k,* and *l* and the intensities of each reflection are recorded. These data allow us to determine the space group and the unit cell parameters of the crystal. As a full data set contains many images,

the reflections intensities of symmetry-related reflections are scaled, averaged and then merged into a unique set of reflections[41]. The quality of the data is assessed using the Pearson correlation coefficient between random half-data sets (CC1/2), this also determines the high-resolution cutoff for the data. A $CC_{1/2}$ at or above 0.5 is acceptable[42].

The intensity of the reflections is a function of the amplitude of the diffraction wave and the phase angle difference[41]. Both the amplitudes and the phases are needed to calculate the electron density map. Using the Fourier transform equation the electron density ρ(xyz).

$$\rho(xyz) = \frac{1}{V_c}\sum_h \sum_k \sum_l |F(hkl)|\, e^{i\alpha(hkl)} e^{-2\pi i(hx+ky+lz)} \qquad (1.4)$$

In equation 1.4, V_c is the volume of the unit cell, |F(hkl)| is the structure factor for the Bragg reflection with Miller indices *h, k,* and *l*; x, y, and z are the fractional coordinates of the unit cell, and α(hkl) is the phase of the reflection, which is unknown. As the phases of the reflections cannot be calculated in from the Fourier transform, leading to the phasing problem. Therefore, the phasing problem needs to be overcome to generate the electron density map[40].

There are several methods to solve this phasing problem, including multiple isomorphous replacement (MIR), multi-wavelength anomalous dispersion (MAD), single-wavelength anomalous dispersion, and molecular replacement (MR)[40, 41, 43]. Using MR, which depends on having the structure of a similar model to the molecule being studied, was used to solve all of the structures presented in this dissertation. During MR, structural phases are calculated at all possible permutation of different positions and rotations of a known homologous structure is placed within the experimental crystal unit cell. Theoretical diffraction patterns of each permutation are calculated and compared with the experimental diffraction patterns. The position and rotation that results in the best fit to the observed diffraction data are used as a starting estimate of the phases for the unknown structure[43]. To overcome the phasing problem using

MIR, diffraction patterns are measured for a native protein crystal and from a crystal soaked in a heavy atom (i.e. platinum or gold). Data sets from crystals soaked in at least two different heavy atoms need to be obtained. The position of the heavy atom in the unit cell is located using the Patterson synthesis, obtain the Patterson difference map, which the amplitude and the phase of the heavy-atoms can be determined. From there the protein phases are readily estimated from the heavy-atom positions[40]. Using MAD to overcome the phasing problem, data sets are collected from one crystal at three different wavelengths. As most protein atoms do not have significant anomalous scattering, selenium is incorporated into methionine. As the intensities of the diffraction patterns differ the positions of the anomalous scattering within the unit cell can be determined, and therefore determine the phases of the protein[40].

Once the amplitudes and phases are identified, the electron density map can be generated, in which the new protein structure can be built. Once the initial structure is determined from the electron density, it needs to be further refined to increase the agreement with the electron density map and the observed diffraction data. Multiple software suites can be used for MR, model building, and refinement of the structure solutions, including PHENIX[44] and the CCP4 software suite[45]. R-factors are used to evaluate the agreement between the experimental structure factors and those calculated from the model.

$$R - factor = \frac{\sum ||F_{obs}| - |F_{calc}||}{\sum |F_{obs}|} \quad (1.5)$$

In equation 1.5, $|F_{obs}|$ represents the experimentally measured structure factors, and $|F_{calc}|$ are the calculated structure factors from the latest model[40]. To fully validate the final structure, ~5 to 10% of the reflections are omitted during the modeling and refinement process. Using these omitted reflections, the free R-factor (R_{free}) is calculated in the same way as the R-factor. The reflections used in refinement are known as the working set, and the R-factor calculated from

them are called R_{work}. During refinement, both R_{free} and R_{work} should decrease, but R_{free} is usually slightly larger than R_{work}, although normally the difference is smaller than 5%[46]. Ideally, the R_{free} of a successful refinement should be about one-tenth of the structure resolution, as that shows that the refinement in correct.

1.5.6. Cryo-Electron Microscopy (EM)

Recently, it has become possible to use Cryo-EM to solve structures of proteins to atomic or near-atomic resolution[47]. Cryo-EM is useful for solving structures of macromolecules or complexes that are large or dynamic that have been difficult to solve from other methods, as there is no need to crystallize the protein[48]. The first step in cryo-EM is sample preparation. The purified protein needs to be adsorbed on the grid, and the grids need to be prepared using multiple methods, such as negative staining or vitrification[49]. In negative staining, the protein sample adsorbed on the grid is stained with a heavy metal salt such as uranyl acetate or uranyl formate. Negative staining can be done at room temperature[49]. The most common method of vitrification is plunge freezing during which the grid bearing the sample is plunged into liquid ethane or propane cooled by liquid nitrogen, leading to the sample being fixed in a thin layer of vitreous ice[49, 50].

Once the grids are prepared, they are imaged to obtain 2D electron micrographs. To avoid electron damage, small electron doses are used, resulting in a low signal-to-noise ratio, producing low resolution images. The RELION[51] program is used to process the data on these images and solve the structure of the macromolecule. As the proteins are in random orientations this is not an easy process[50]. Particles are picked from the 2D electron micrographs, these particles are then sorted into 2D classes corresponding to a specific orientation, and the particles

within each class are averaged to obtain high-resolution 2D projections. These 2D projections are then combined to obtain a high-resolution structure of the protein[52].

1.6. Specific Aims of This Research

As yet, it is unclear why mammals have two BECN homologs, while lower eukaryotes have only one. Understanding the interactions of BECN1 and BECN2 in atomic detail should help us understand that. Further, with the growing number of BECN2 interaction partners and pathways that BECN2 functions in, it is important to understand how these interactions and functions differ from those of BECN1. Therefore, the goal of this dissertation is to investigate specific BECN1 and BECN2 interactions, focusing on the interaction of the BECN2 CCD. The specific aims of this research are:

1. To use Cryo-EM to investigate conformational changes in BECN1 during the interaction with M11, to help determine why M11's interaction inhibits autophagy.
2. To investigate the interaction of the BECN2 CCD with the UVRAG CCD, in order to understand how the interaction differs from that with the BECN1 CCD, and determine if the interaction differs in autophagy.
3. To investigate the interaction of the BECN2 CCD with the TAB2 CCD or the TAB3 CCD, and understand how the interaction differs from the interaction of the BECN1 CCD with TAB2 CCD or TAB3 CCD, therefore show if there is a difference in the function of the interaction in autophagy.
4. To investigate the interaction of the BECN2 CCD with the STX6 SNARE domain and understand how this interaction may functions in non-canonical autophagy.

CHAPTER 2. INVESTIGATING THE INTERACTION AND CONFORMATIONAL CHANGE OF BECN1$^{\Delta 31\text{-}104,AFM}$ AND M11 USING CRYO-EM

2.1. Introduction

Anti-apoptotic BCL2 homologs have been shown to down-regulate autophagy by binding to the BECN1 BH3D[53, 54]. All anti-apoptotic BCL2 homologs have a similar three-dimensional structure[55]. The interaction between the BECN1 BH3 domain and the murine γ-Herpesvirus 68 Bcl-2 homolog, M11, has previously been structurally and thermodynamically characterized[15]. The BECN1 BH3D binds as an amphipathic helix within the hydrophobic groove of M11. M11 binds to BECN1 residues 1-135 with an affinity of 0.2 ± 0.1 μM, which is tighter than the affinity of binding to the isolated BECN1 BH3D[15]. However, the BECN1 BH3D domain is not conserved amongst BECN1 homologs and is dispensable for the induction of autophagy (Mukhopadhyay et. al., unpublished data). Therefore, the mechanism by which binding of BCL2 homologs to the BECN1 BH3D results in the down-regulation of autophagy is not well understood.

Dr. Yue Li had previously determined that BECN1 constructs that contain the BARAD domain precipitate, but this can be prevented by a triad aromatic finger mutation (AFM), F359D/F360D/W361D, in the BECN1 BARAD[19]. Dr. Li started to investigate whether M11 interacts with BECN1 residues outside the BARAD, and whether this interaction causes conformational changes. Since deletion of the IDR reduces sample flexibility, thereby facilitating structural studies, including by Cryo-EM, the MBP-tagged BECN1$^{\Delta 31\text{-}104,AFM}$ construct was selected for further investigation. Dr. Li also showed that binding of M11 stabilizes all BECN1 constructs.

Dr. Li also used SEC-SAXS to compare low resolution structural information of MBP-tagged BECN1$^{\Delta 31\text{-}104,AFM}$ and the MBP-BECN1$^{\Delta 31\text{-}104,AFM}$:M11 complex (unpublished data). The SEC-SAXS indicates that MBP-BECN1$^{\Delta 31\text{-}104,AFM}$ is a well-folded elongated, multi-domain protein with a D_{max} of 310 Å and an average R_g of 96 Å. The SEC-SAXS also indicates that MBP-BECN1$^{\Delta 31\text{-}104,AFM}$:M11 is an well-folded elongated, multi-domain protein with a slightly larger D_{max} of 351 Å and an average R_g of 92 Å. Based on the SAXS envelopes the MBP-BECN1$^{\Delta 31\text{-}104,AFM}$ (Figure 2.1 A) may be a little more compacted then MBP-BECN1$^{\Delta 31\text{-}104,AFM}$:M11 complex (Figure 2.1 B). This SEC-SAXS data provides an idea of the size and overall shape of the particles.

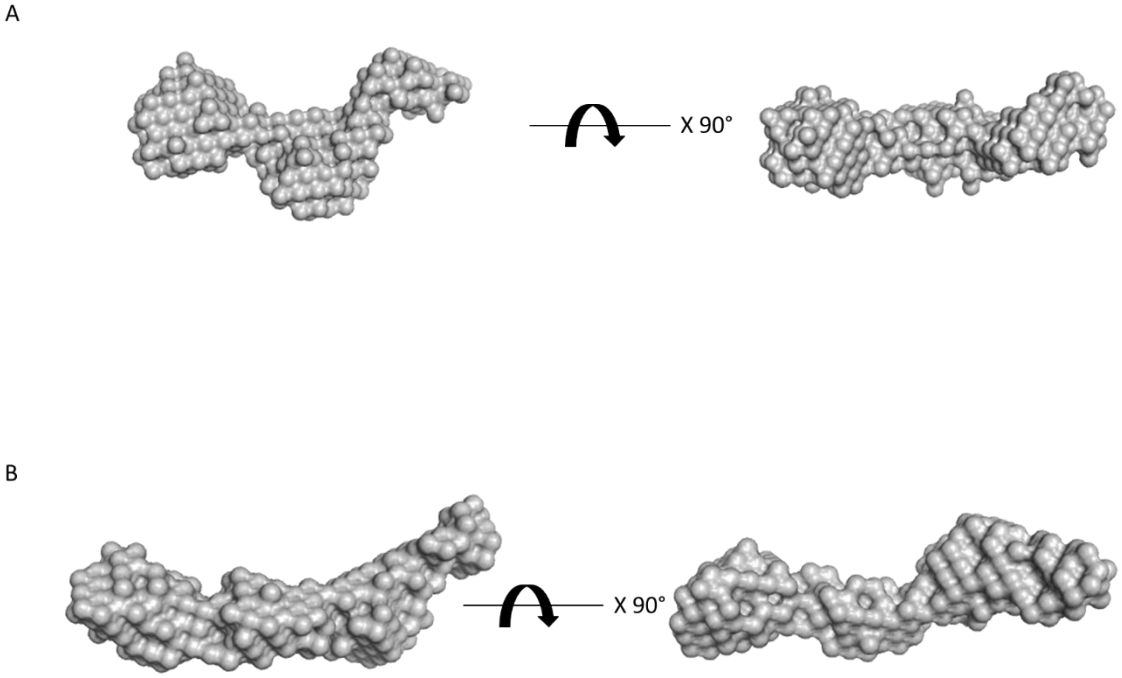

Figure 2.1: SEC-SAXS envelopes calculated by Dr. Yue Li. A) MBP- BECN1$^{\Delta 31\text{-}104,AFM}$, B) MBP- BECN1$^{\Delta 31\text{-}104,AFM}$:M11 complex calculated by Dr. Yue Li (unpublished data).

Next, Dr. Li attempted to obtain negative-stained EM images for the MBP-BECN1$^{\Delta 31\text{-}104,AFM}$ and the M11:MBP-BECN1$^{\Delta 31\text{-}104,AFM}$ complex. Both the MBP-BECN1$^{\Delta 31\text{-}104,AFM}$ and M11:MBP-BECN1$^{\Delta 31\text{-}104,AFM}$ were tested at initial concentrations of 0.43 μM and 0.29 μM respectively, but this resulted in aggregated particles. Sample dilution was attempted, but that appeared to cause dissociation of M11:MBP-BECN1$^{\Delta 31\text{-}104,AFM}$ complex. It is possible that negative-staining causes sample aggregation, therefore, the next step was to use cryo-EM to image these samples.

In this chapter, I report my attempts to use cryo-EM to obtain high resolution information regarding the impact of M11 on the conformation of BECN1, and to identify interactions with BECN1 residues outside the BH3D, in order to understand how that might prevent BECN1 from upregulating autophagy.

2.2. Materials and Methods

2.2.1. Expression and Purification

M11 was expressed with a C-terminal His_6-tag from a pET21(d+) vector as previously described[15]. Dr. Li constructed an expression vector by cloning the DNA sequence encoding BECN1$^{\Delta 31\text{-}104,AFM}$ into the pMBP-Parallel1 expression vector by to create the pMBP-Parallel1-BECN1$^{\Delta 31\text{-}104,AFM}$ expression vector.

E. coli Artic Express cells were transformed with pMBP-Parallel1- BECN1$^{\Delta 31\text{-}104,AFM}$ and grown at 37 °C in LB medium with 100 μg/mL ampicillin plates to select for colonies that contain the pMBP-Parallel1- BECN1$^{\Delta 31\text{-}104,AFM}$ vector. Single colonies were grown in LB medium with 100 μg/mL ampicillin at 37 °C to an OD_{600}=0.7 prior to equilibrating the temperature to 13 °C.

E. coli BL21(DE3) cells were transformed with the pET21(+)-M11-His_6 and grown at 37 °C in LB medium with 100 µg/mL ampicillin plates to select of colonies that contain the pET21(+)-M11-His_6 vector. Single colonies were grown in LB medium with 100 µg/mL ampicillin at 37 °C to an OD_{600}=0.7, prior to equilibrating the temperature to 20 °C.

In each case, after the temperature was equilibrated to the lower temperature, protein expression was induced by the addition of 0.5 mM isopropyl thio-β-D-galactoside (IPTG) and expressed overnight. Cells were harvested by centrifugation at 4000 x g for 15 minutes, cells were then resuspended in buffer, and pelleted into 50 mL conical tubes at 4 °C prior to storage at -80 °C.

Pellets from a 1.5 L cell culture were resuspended in 50 mL of wash buffer and a protease inhibitor cocktail tablet (Bimake) added. Resuspended cells were lysed using a NanoDeBEE emulsifier (BEE International) or by a Bronson 459 sonifier (Bronson). The lysate was centrifuged at 20,000 x g for 30 minutes to pellet cell debris and clarify the lysate. At each stage of purification, protein purity was evaluated by SDS-PAGE stained with Coomassie Blue.

The MBP- $BECN1^{\Delta 31\text{-}104,AFM}$ protein was purified from clarified lysate by amylose affinity chromatography using a 10 mL amylose resin column (NEB BioLab). The column was washed with 30 column volumes of wash buffer (50 mM Tris pH 8, 300 mM NaCl, 1 mM EDTA, 2 mM Dithiothreitol (DTT)). Protein was eluted from the amylose resin with wash buffer with the addition of 20 mM maltose. Pooled fractions were concentrated to 15 mg/mL before size exclusion chromatography (SEC). Final purification was achieved by injecting 0.5 mL over a Superdex 200 increase 10/300 SEC column (GE Healthcare) equilibrated with SEC buffer (50 mM Tris pH 8, 300 mM NaCl, 2 mM β-mercaptoethanol (βME)) and eluted using an isocratic gradient. Absorbance at 280 nm was monitored and 1 mL fractions collected during the course of

the elution. Purified protein was concentrated to 12.6 mg/mL using a 30 kD Amicon Ultra-4 centrifugal concentrator (MilliporeSigma), flash-frozen in 25 µL aliquots dropwise into liquid N_2 and stored at -80 °C.

The His_6-M11 protein was purified from the clarified lysate by Ni^{++}-NTA affinity chromatography using a 5 mL of Ni^{++}-NTA resin column (Thermo Fisher Scientific). The column was washed with 30 column volumes of wash buffer (50 mM HEPES pH 7.5, 250 mM NaCl, 2 mM βME, 25 mM Imidazole). Protein was eluted from the Ni^{++}-NTA resin with wash buffer with the addition of 250 mM Imidazole. Pooled fractions were concentrated to 15 mg/mL before SEC. Final purification was achieved by injection 0.5 mL over a Superdex 75 increase 10/300 SEC column (GE Healthcare) equilibrated with SEC buffer (50 mM HEPES pH 7.5, 250 mM NaCl, 2 mM βME) and eluted using an isocratic gradient. Absorbance at 280 nm was monitored and 1 mL fractions were collected during the course of the elution. Purified protein was concentrated to 15.3 mg/mL using a 10 kD Amicon Ultra-4 centrifugal concentrator (MilliporeSigma), flash-frozen in 25 µL aliquots dropwise into liquid N_2 and stored at -80 °C.

The His_6-M11:MBP- $BECN1^{\Delta 31\text{-}104,AFM}$ complex was obtained by mixing pure His_6-M11 with pure MBP- $BECN1^{\Delta 31\text{-}104,AFM}$ at a 3:2 molar ratio. Proteins were allowed to complex for 1 hour on ice prior to being passed over 2 mL of Ni^{++}-NTA resin (Thermo Fisher Scientific). The column was washed with 30 column volumes of Ni^{++}-NTA wash buffer. Protein was eluted from the Ni^{++}-NTA resin with wash buffer with the addition of 250 mM Imidazole. Pooled fractions were concentrated to 10 mg/mL before SEC. Final purification was achieved by injection 0.5 mL over a 200 increase 10/300 SEC column (GE Healthcare) equilibrated with SEC buffer (50 mM Tris pH 8, 300 mM NaCl, 2 mM βME) and eluted using an isocratic gradient. Purified protein complex was not concentrated after SEC, and the main peak fraction at a concentration of 3.2

μM, was flash-frozen in 25 μL aliquots dropwise into liquid N_2 and were stored at -80 °C for cryo-EM data collection.

2.2.2. Cryo-EM Sample Preparation and Data Collection

Grid preparation and imaging was done by Dr. David Belnap at the University of Utah. Cryo-EM grids were made by applying 4 μL of 3.2 μM of His_6-M11:MBP- BECN1$^{\Delta 31\text{-}104,AFM}$ complex onto a glow-discharged, holey carbon-coated, copper grids, incubated at 15 °C, in 100% relative humidity, prior to blotting to leave a thin uniform film, using a Vitrobot (Thermo Fisher). The grid was immediately plunge frozen in liquid ethane and the grids stored under liquid N_2 until screening. Grids were imaged on a Titan Krios 300 keV microscope (Thermo Fisher) equipped with a FRG and camera at the Electron Microscopy Core Laboratory at the University of Utah, Utah, USA. Concentration was optimized by imaging grids with different sample dilutions: undiluted, 10-fold dilution, and 100-dilution. Nine images were taken per stage move for a total of 3,938 images. Images were taken with a pixel size of 0.53 Å, a voltage of 300 kV, a spherical aberration of 2.7 mm, an amplitude contrast of 0.1, and a beam tilt (X & Y) of zero. An optimal concentration of 3.2 μM was determined and used for final data collection.

2.3. Results

2.3.1. Expression and Purification of MBP- BECN1$^{\Delta 31\text{-}104,AFM}$

MBP- BECN1$^{\Delta 31\text{-}104,AFM}$ fusion protein was purified by amylose affinity chromatography followed by SEC. The SEC elution profile contains a single peak with a leading-edge shoulder (Figure 2.2). The front shoulder is in the void volume and likely contains aggregated protein. SDS-PAGE indicates that the main 10.2 mL peak contains MBP- BECN1$^{\Delta 31\text{-}104,AFM}$. The molecular weight of the MBP- BECN1$^{\Delta 31\text{-}104,AFM}$ estimated from Kavg was 404.8 kD which is ~2.3 times larger than the theoretical molecular weight of 173.9 kD for an MBP- BECN1$^{\Delta 31\text{-}}$

^{104,AFM} dimer calculated from the amino acid sequence. This suggests that MBP- BECN1$^{\Delta 31-104,AFM}$ is an elongated homodimer. The final yield of the purified MBP- BECN1$^{\Delta 31-104,AFM}$ obtained from one liter of bacterial culture was 2.1 mg.

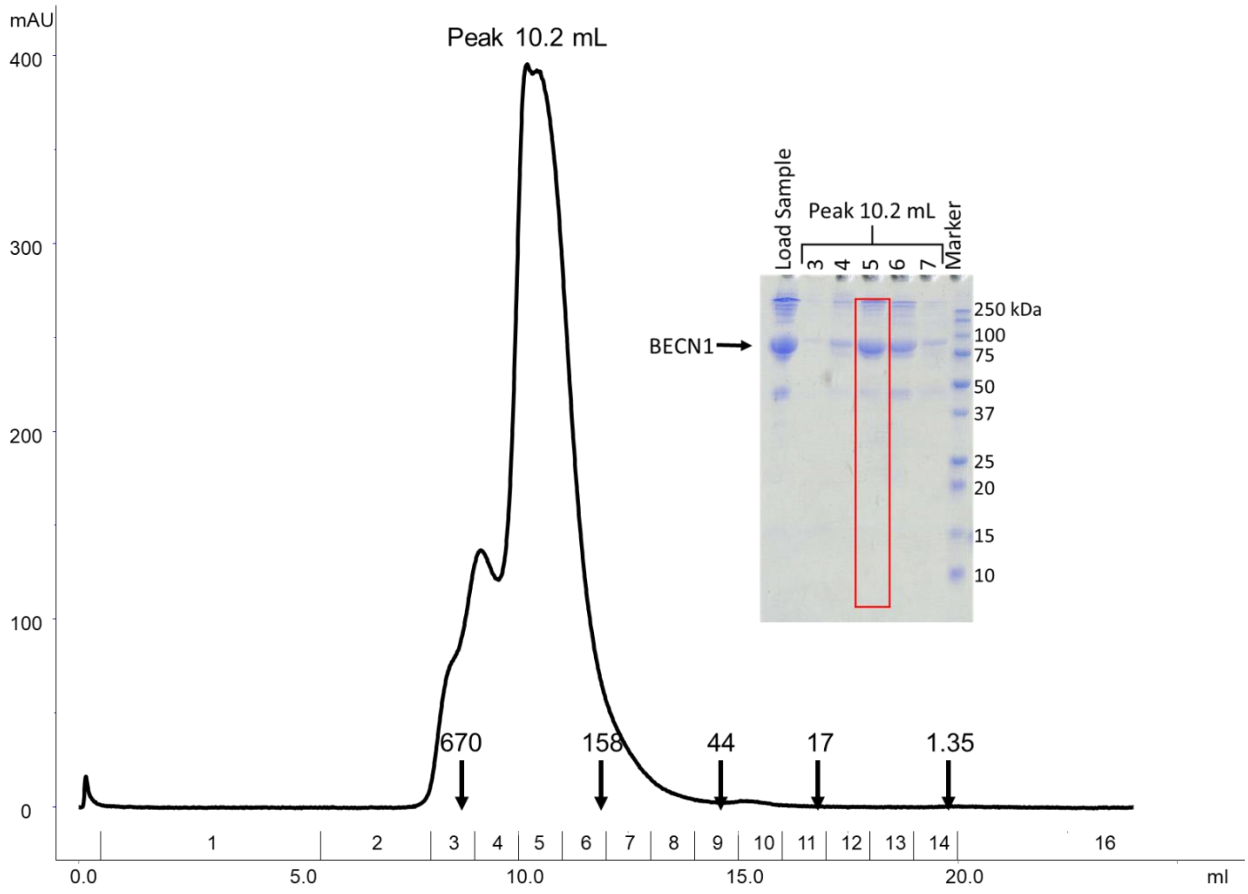

Figure 2.2: Size exclusion chromatogram and the Coomassie-stained SDS-PAGE gel of MBP-BECN1$^{\Delta 31-104,AFM}$. The elution positions of SEC Superdex 200 increase 10/300 standards are indicated by arrows. The fraction boxed in red was used to form the complex and corresponding molecular weight.

2.3.2. Expression and Purification of His$_6$-M11

The His$_6$-M11 fusion protein was purified by Ni^{++}-NTA affinity chromatography followed by SEC. The SEC elution profile contains 2 distinct peaks (Figure 2.3). SDS-PAGE indicates that the first peak eluting at 12 mL includes higher molecular weight contaminants, while the second peak eluting at 14.3 mL comprises only His$_6$-M11. The molecular weight of the

His_6-M11 estimated from Kavg was 15.3 kD which is within error to the theoretical molecular weight of 16.6 kD for the His_6-M11 monomer calculated from the amino acid sequence. This indicates that His_6-M11 is a globular protein. The final yield of the purified His_6-M11 obtained from one liter of bacterial culture was 2.5 mg.

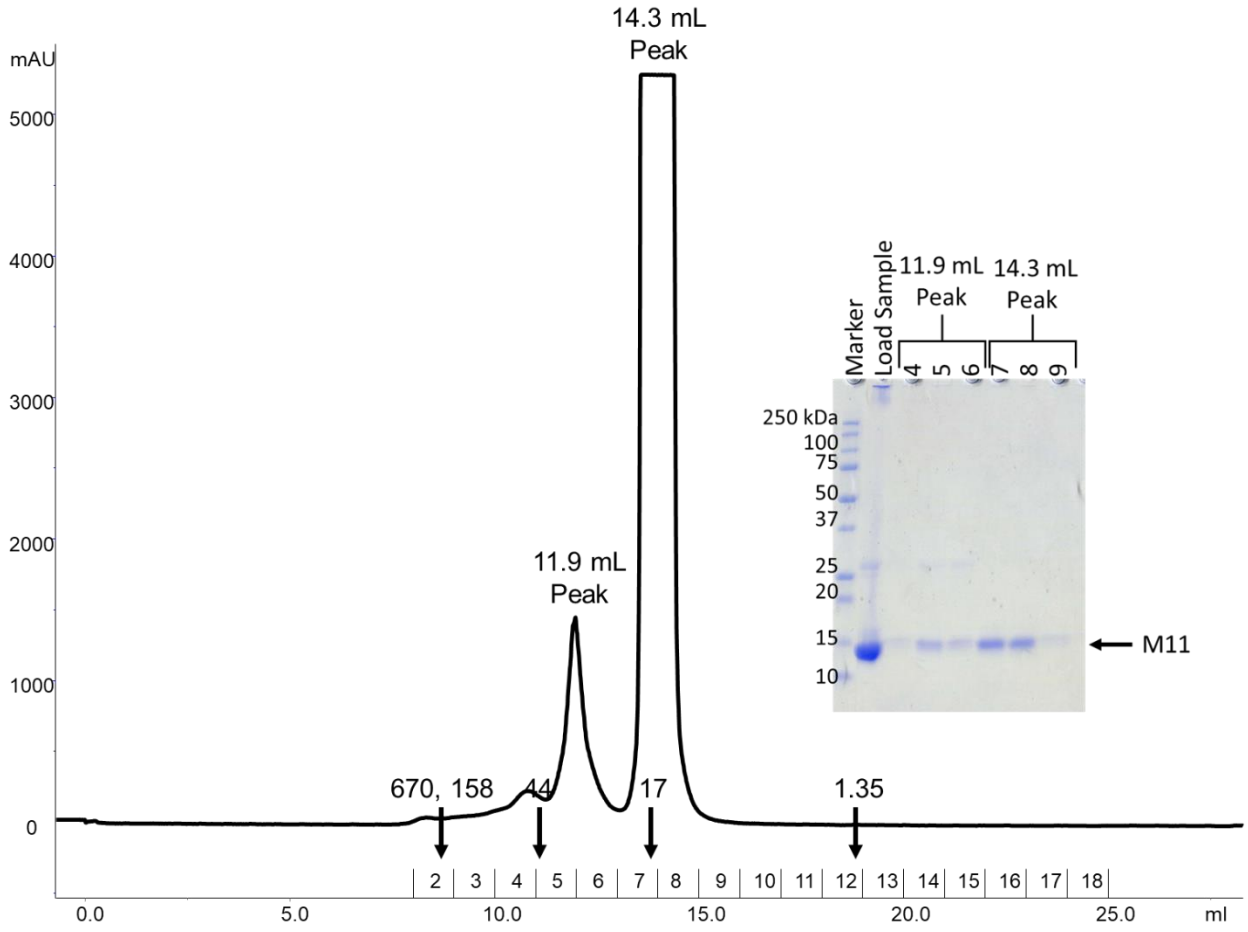

Figure 2.3: Size exclusion chromatogram and Coomassie-stained SDS-PAGE gel of Sumo-His_6-M11. The elution positions of SEC Superdex 75 increase 10/300 standards are indicated by arrows and corresponding molecular weight.

2.3.3. Purification of His_6-M11:MBP- $BECN1^{\Delta 31\text{-}104,AFM}$

The His_6-M11:MBP- $BECN1^{\Delta 31\text{-}104,AFM}$ complex was purified by Ni^{++}-NTA affinity chromatography followed by SEC. The SEC elution profile contains 2 major peaks (Figure 2.4).

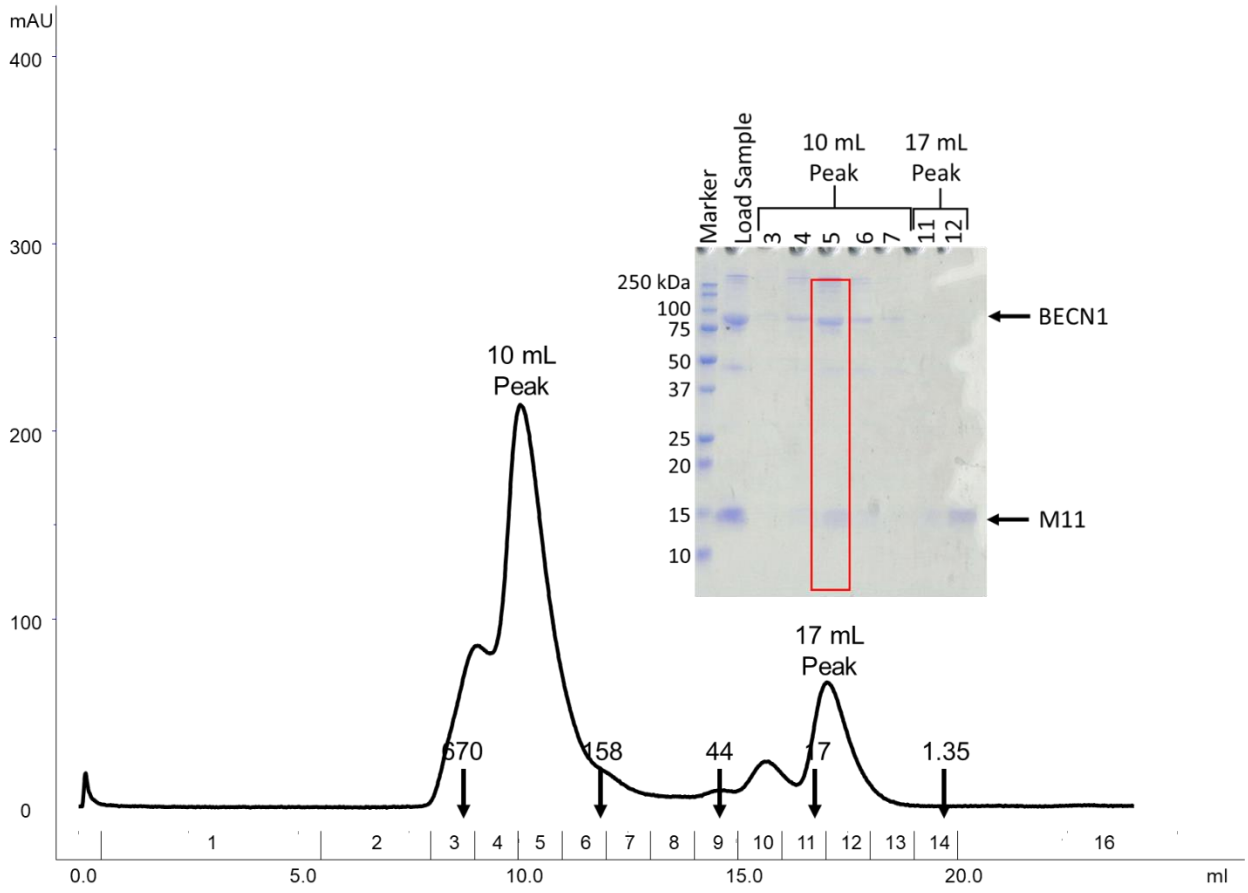

Figure 2.4: Size exclusion chromatogram and Coomassie-stained SDS-PAGE gel of His_6-M11:MBP- $BECN1^{\Delta 31\text{-}104,AFM}$ complex. The elution positions of SEC Superdex 200 increase 10/300 standards are indicated by arrows and corresponding molecular weight. The fraction boxed in red is the complex sent for cryo-EM.

The first peak which elutes at 10.4 mL, is the likely complex as SDS-PAGE indicates the presence of both proteins. This peak has a leading-edge shoulder, which overlaps the void volume and likely contains aggregated protein. The second peak, which elutes at 17 mL, contains unbound, excess His_6-M11 as expected. The molecular weight of the presumed His_6-M11:MBP-$BECN1^{\Delta 31\text{-}104,AFM}$ complex estimated from Kavg was 445 kD which is ~2.1 times larger than the molecular weight of 207.1 kD for the His_6-M11:MBP- $BECN1^{\Delta 31\text{-}104,AFM}$ dimer calculated from the amino acid sequence. It is likely that this significantly higher MW estimate is the result of the complex being an extended molecule in agreement with previous SEC-SAXS experiments.

Fraction five from SEC, which had the largest Abs_{280} from peak 1 of the His_6-M11:MBP-$BECN1^{\Delta 31\text{-}104,AFM}$ complex, had a concentration of 3.2 µM and was sent for Cryo-EM imaging without additional concentration.

2.3.4. Cryo-EM Data Analysis using RELION

Dr. Belnap tested different sample dilutions and determined that the undiluted sample at 3.2 µM gave sufficient His_6-M11:MBP- $BECN1^{\Delta 31\text{-}104,AFM}$ complex particle dispersion, and was selected for data collection. He recorded 3,921 micrographs, of which only 2,505 contained particles, most of which only contained a few particles. An example of a micrograph and the particles picked are shown in Figure 2.5. 25,045 particles were manually picked from these 2,505 micrographs using RELION 3.1[56]. These particles were assigned into classes and initially used to calculate 25 2D class averages, and subsequently 50 2D class averages (Figure 2.6 and Figure 2.7). Unfortunately, these initial classes did not show any resemblance to the SAXS envelopes previously calculated by Dr. Yue Li. Some of the particles that were picked had a length of 350 Å, which is similar in size to the D_{max} found by Dr. Yue Li's SAXS data, other particles were smaller in size, which may include dissociated complexes. Therefore, in order to improve the 2D classes, we selected the 2D classes that best matched the sizes and different orientations of the SAXS envelope (Figure 2.7). The particles in these selected classes (Figure 2.8) were reassigned into new 2D classifications. However, even after redoing the 2D classifications in this manner, the class averages still did not look as expected (Figure 2.9).

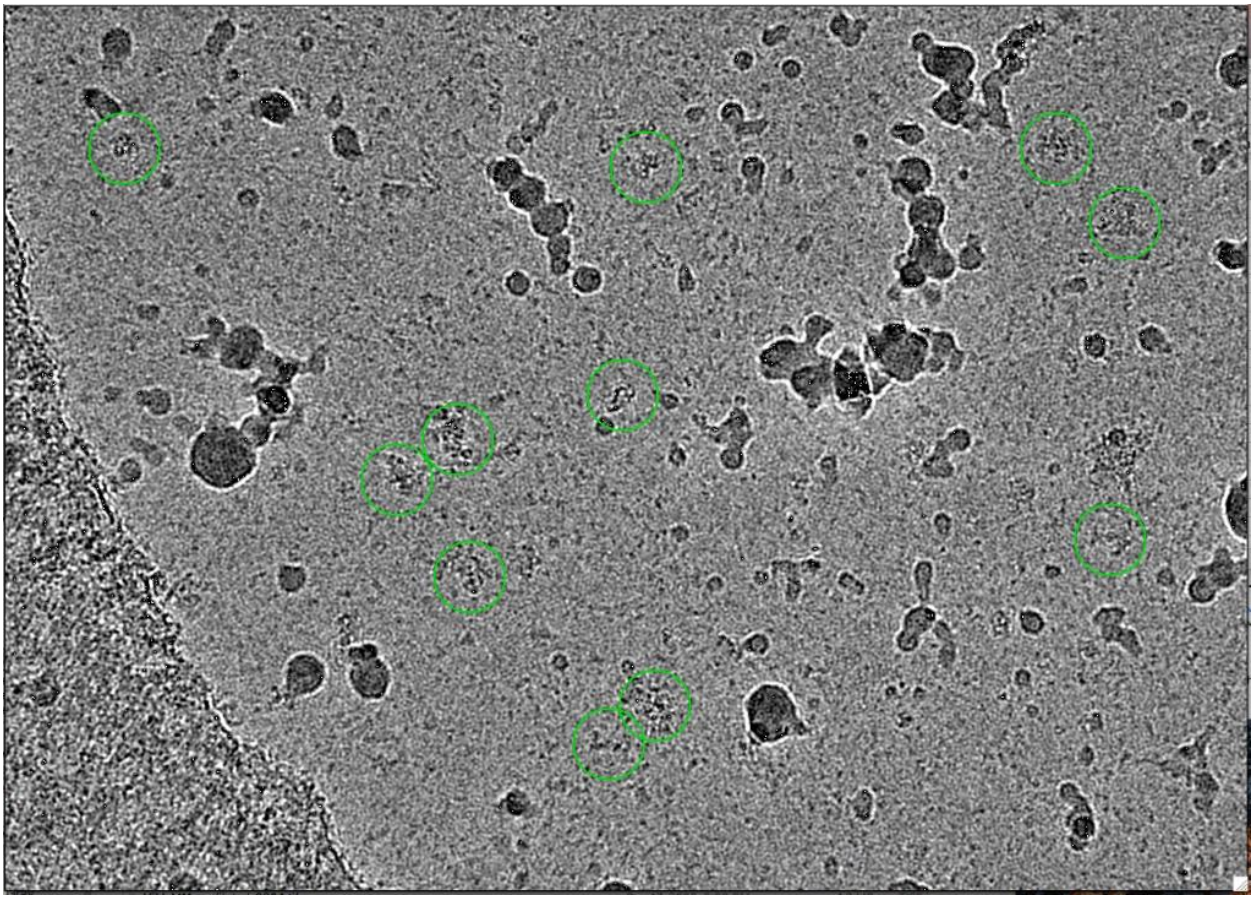

Figure 2.5: An example of the micrographs used for manual picking of particles circled in green.

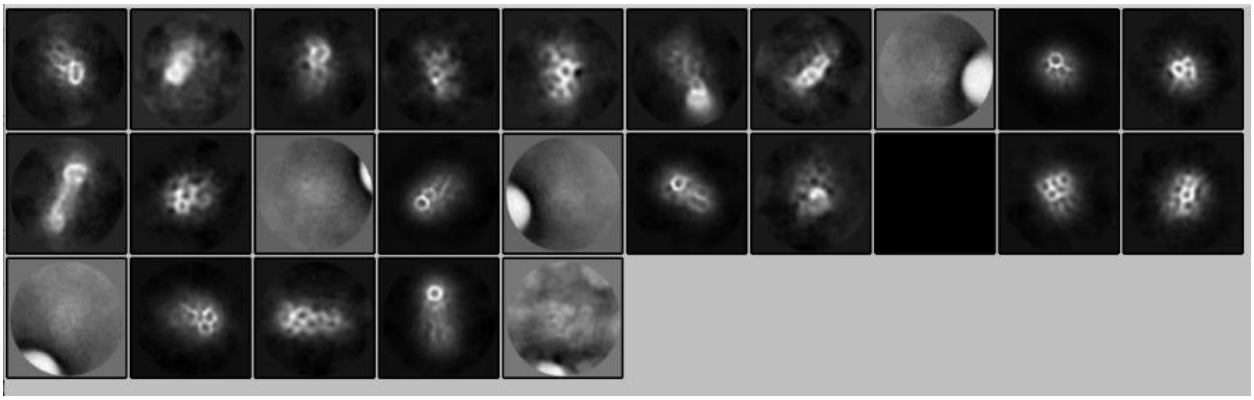

Figure 2.6: The 2D classes of the 25,045 manually picked particles. 25 total classes.

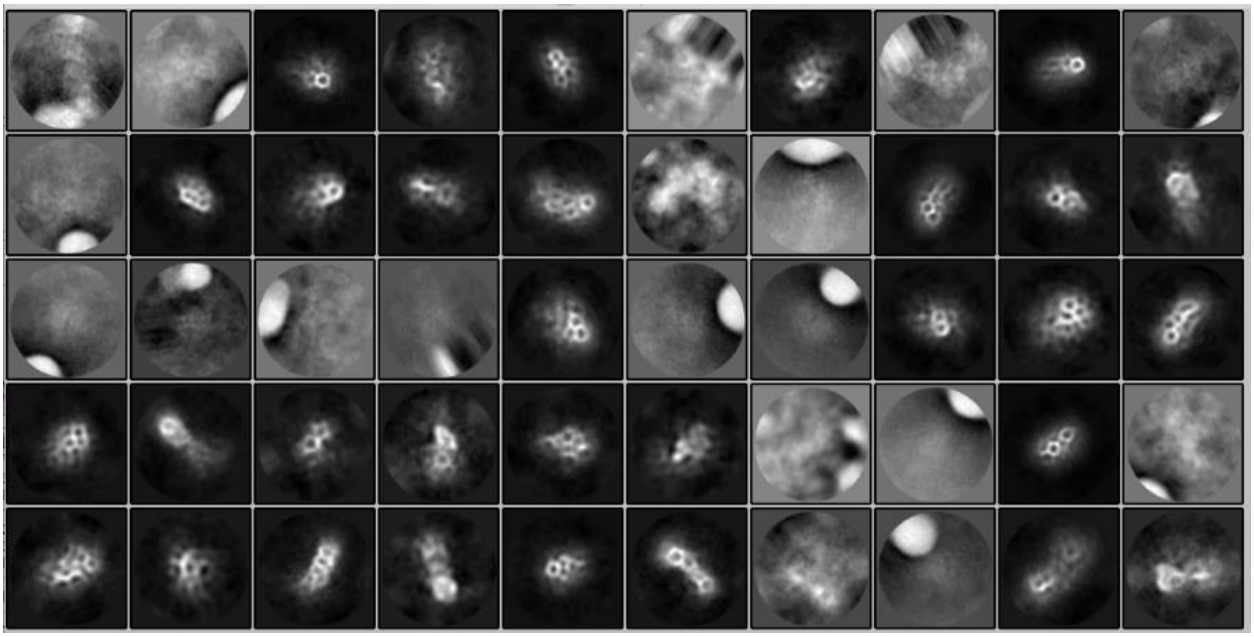

Figure 2.7: The 2D classes of the 25,045 manually picked particles. 50 total classes.

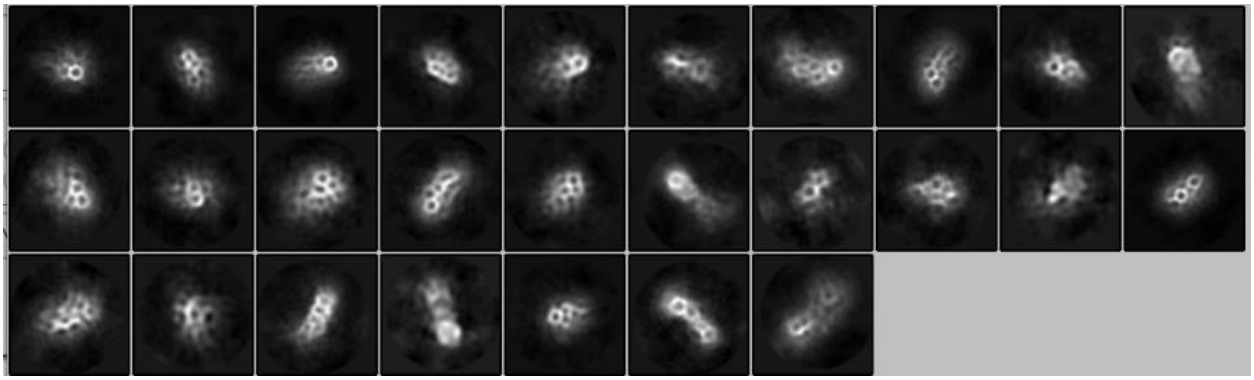

Figure 2.8: Selected 2D classes that looked closest to SAXS envelope from Figure 2.7. The practices within these classes were used to redo the 2D classifications.

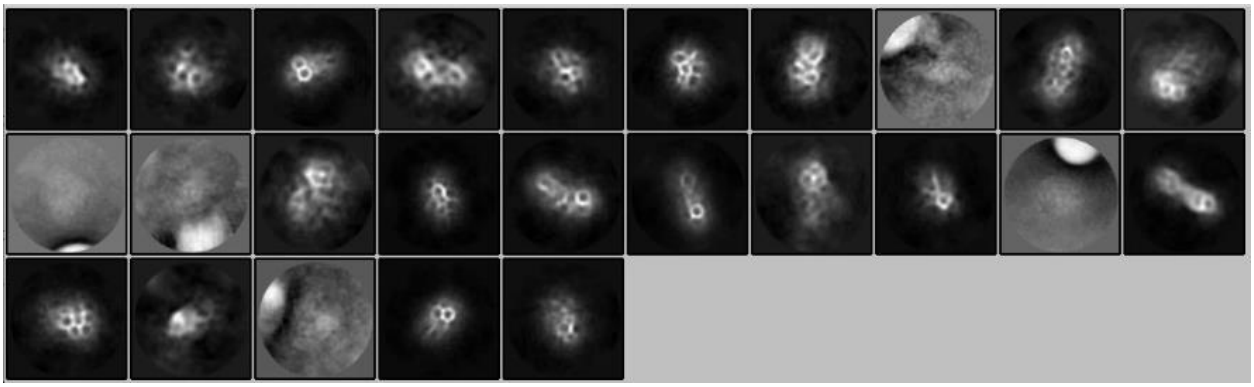

Figure 2.9: Recalculated 2D classes from particles in previously selected 2D classes shown in Figure 2.8.

2.4. Conclusions and Discussion

We were able to purify the complex of His_6-M11:MBP- $BECN1^{\Delta 31\text{-}104,AFM}$, based on the protocol developed by Dr. Yue Li. Dr. Belnap was able to record Cryo-EM micrographs of these samples. We were able to pick ~25,000 particles from these micrographs, and assign them to classes and calculate 2D class averages. However, these 2D class averages did not correspond well with the low-resolution SAXS envelope of the complex calculated by Dr. Yue Li, which agrees with our SEC data and prior results from SEC-SAXS experiments that the BECN1 protein has an extended conformation. Therefore, we did not pursue a 3D structure using single particles analysis with this sample.

However, there are still multiple avenues that could be pursued to obtain a molecular structure of the His_6-M11:MBP- $BECN1^{\Delta 31\text{-}104,AFM}$ complex. One possible way to facilitate the determination of the structure of the His_6-M11:MBP- $BECN1^{\Delta 31\text{-}104,AFM}$ complex using Cryo-EM, would be to increase particle size by binding an antibody to the complex. Inclusion of an antibody in the complex would not only make it larger, but also it would also provide a recognized marker for the particles, making it easier to pick the particles. This is because the antibody has a well-defined, globular, 3D structure, that would enable us to recognize and assign

true 2D classes more easily, leading to better 2D class averages. Subsequent, single particle analysis yielding a high-resolution structure of His_6-M11:MBP- $BECN1^{\Delta 31\text{-}104,AFM}$ would allow us to understand M11 interactions with BECN1 residues outside the BH3D, M11-binding induced conformational changes in BECN1, and the mechanism by which these additional interactions and conformational changes enable M11 and other BCL2 homologs to down-regulate autophagy.

CHAPTER 3. INVESTIGATION OF THE INTERACTION BETWEEN THE BECN2 CCD AND UVRAG CCD

3.1. Introduction

UVRAG is the human homolog of yeast Vps38[1]. UVRAG functions in autophagy by promoting autophagosome formation by associating with BECN1 as part of the PI3KC3 complex 2, and up-regulating PI3KC3 activity[57-59]. UVRAG contains an N-terminal polyproline disordered region, a C2 domain, a CCD, and a large intrinsically disordered region (Figure 3.1)[1]. The UVRAG CCD has been shown to interact with BECN1 CCD[58]. BECN1 and UVRAG are interdependent when it comes to inducing autophagosome formation, when BECN1 or UVRAG are knock-down autophagosome formation is decreased[58]. The interaction of BECN1 CCD:UVRAG CCD increases autophagy levels in cells and disrupting this interaction inhibits autophagy in cells[1, 58].

Figure 3.1: UVRAG domain architecture. Light green: PR: polyproline disordered region, Light blue C2 domain, yellow: CCD, and gray: disordered regions.

Immunoprecipitation assays showed that key autophagy proteins that interact with BECN1 also interact with human BECN2 and mouse BECN2[21]. One of these interacting partners is UVRAG, although the coimmunoprecipitation assays indicate that there may be a difference in the binding affinities of the interaction of UVRAG with BECN1 and BECN2[21].

The aim of this study was to determine if the BECN2 and UVRAG CCDs interact, quantify the affinity of interaction, and elucidate the atomic details of the interaction. We used affinity pull-downs to determine if BECN2 CCD interacts with UVRAG CCD and ITC to quantify the interaction affinity.

3.2. Materials and Methods

3.2.1. Creation of Protein Expression Constructs

The BECN2 CCD was expressed as a fusion protein, including a small ubiquitin-like modifier (SUMO), TEV-protease site, and His_6-tag preceding the protein, from the pET28-Sumo-TEVsite-His_6-BECN2 CCD previously used to purify the BECN2 CCD[20]. An expression vector was constructed by cloning the cDNA sequence encoding the UVRAG CCD (residues 230-320) into the pMBP parallel 1 expression vector between NdeI and XhoI restriction enzyme sites by Mr. Samuel Wyatt.

3.2.2. Purification of MBP-UVRAG CCD and Sumo-His_6-BECN2 CCD

E. coli BL21(DE3)pLysS cells were transformed with pMBP parallel1- MBP-UVRAG CCD expression plasmids and grown at 37 °C in LB medium with 100 µg/mL ampicillin plates to select for colonies that contain the pMBP parallel1- MBP-UVRAG CCD vector. A single colony was grown in LB medium with 100 µg/mL ampicillin at 37 °C to an OD_{600}=0.7, prior to equilibrating the temperature to 20 °C.

E. coli Artic Express cells were transformed with pET-28-Sumo-His_6-BECN2 CCD expression plasmids and grown at 37 °C in LB medium with 15 µg/mL kanamycin plates to select of colonies that contain the pET-28-Sumo-His_6-BECN2 CCD vector. A single colony was grown in LB medium with 100 µg/mL ampicillin at 37 °C to an OD_{600}= 0.7, prior to equilibrating the temperature to 13 °C.

In each case, after the temperature was equilibrated to the lower temperature, protein expression was induced by the addition of 0.5 mM IPTG was added after equilibration to induce expression overnight. Cells were harvested by centrifugation at 4000 x g for 15 minutes, cells

were then resuspended in buffer, and pelleted into 50 mL conical tubes at 4 ℃ prior to storage at -80 °C.

For each protein, cell pellets from 1.5 L of cell culture were resuspended in 50 mL of lysis buffer (50 mM Tris pH 8, 300 mM NaCl, 1 mM EDTA, 2 mM DTT) for MBP-UVRAG and 25 mM Tris pH 8, 150 mM NaCl, 2 mM βME, 25 mM Imidazole for SUMO-His_6-BECN2 CCD, and a protease inhibitor cocktail tablet (Bimake) was added. Resuspended cells were lysed using a NanoDeBEE emulsifier (BEE International) or a Bronson 459 sonifier (Bronson). The lysate was centrifuged at 20,000 x g for 30 minutes to pellet cell debris and clarify the lysate. At each stage of purification, protein purity was evaluated by SDS-PAGE stained with Coomassie Blue.

The MBP-UVRAG CCD fusion protein was purified from the clarified cell lysate by amylose affinity chromatography using a 10 mL of amylose resin column (NEB BioLabs). The column was washed with 30 column volumes of wash buffer (50 mM Tris pH 8, 300 mM NaCl, 1 mM EDTA, 2 mM DTT). Protein was eluted from the amylose resin with elution buffer (50 mM Tris pH 8, 300 mM NaCl, 2 mM βME, 20 mM maltose). Pooled fractions were concentrated to 10.2 mg/mL before SEC. Final purification was achieved by injecting 0.5 mL over a Superose 6 10/300 SEC column (GE Healthcare) equilibrated with SEC buffer (50 mM Tris pH 8, 300 mM NaCl, 2 mM βME) and eluted using an isocratic gradient. Absorbance at 280nm was monitored and 0.5 mL fractions were collected during the course of the elution. Purified protein was concentrated to 11.5 mg/mL using a 30 kD Amicon Ultra-4 centrifugal concentrator (MilliporeSigma, flash-frozen in 25 µL aliquots dropwise into liquid N_2 and stored at -80 °C.

The Sumo-His_6-BECN2 CCD was purified from the clarified lysate by Ni^{++}-NTA affinity chromatography using a 5 mL of Ni^{++}-NTA resin column (Thermo Fisher Scientific). The

column was washed with 30 column volumes of wash buffer (25 mM Tris pH 8, 150 mM NaCl, 2 mM βME, 25 mM Imidazole). Protein was eluted from the Ni^{++}-NTA resin with wash buffer with the addition of 250 mM Imidazole. Pooled fractions were concentrated to 13.16 mg/mL before SEC. Final purification was achieved by injecting 0.5 mL over a Superdex 200 increase 10/300 SEC column (GE Healthcare) equilibrated with SEC buffer (25 mM Tris pH 8, 150 mM NaCl, 2 mM βME) and eluted using an isocratic gradient. Absorbance at 280 nm was monitored and 0.5 mL fractions collected during the course of the elution. Purified protein was concentrated to 13.57 mg/mL using a 10 kD Amicon Ultra-4 centrifugal concentrator (MilliporeSigma), flash-frozen in 25 µL aliquots dropwise into liquid N_2 and stored at -80 °C.

3.2.3. Pulldown Assays

Pulldowns of MBP-UVRAG CCD and Sumo-His_6-BECN2 CCD were performed by using either completely purified proteins as described above, or proteins partly purified up to binding to and washing on affinity resin. At each stage of purification, protein purity was evaluated by SDS-PAGE stained with Coomassie Blue.

Completely purified or partly purified (i.e. via only affinity chromatography) Sumo-His_6-BECN2 CCD was added to partly-purified MBP-UVRAG CCD bound to amylose affinity resin. Proteins were allowed to complex at 4 °C for either 1 hour or overnight, after the resin was stirred. The column was washed with 30 column volumes of wash buffer (20-25 mM Tris pH 8, 150-300 mM NaCl, 2 mM βME). Protein was eluted from the amylose resin with wash buffer with the addition of 20 mM maltose. Protein that eluted as the complex was added to Ni^{++}-NTA affinity resin and washed with 30 column volume wash buffer (20-25 mM Tris pH 8, 150-300 mM NaCl, 2 mM βME, 20 mM Imidazole). The protein was eluted from the Ni^{++}-NTA resin with wash buffer with the addition of 250 mM imidazole. Elution fractions that appeared to

contain Sumo-His_6-BECN2 CCD and MBP-UVRAG in a one-to-one ratio, as indicated by SDS-PAGE, were pooled, concentrated and further purified by SEC using Superdex 200 increase 10/300 or Superdex 16/60 SEC column (GE Healthcare) in SEC buffer (20-25 mM Tris pH 8, 150-300 mM NaCl, 2 mM βME).

Partly purified MBP-UVRAG CCD was added to Sumo-His_6-BECN2 CCD bound to Ni^{++}-NTA affinity chromatography resin and allowed to complex for either 1 hour or overnight at 4 °C, after the column was stirred. The column was washed with 30 column volume wash buffer (20-25 mM Tris pH 8, 150-300 mM NaCl, 2 mM βME). The protein was eluted from the Ni^{++}-NTA resin with wash buffer with the addition of 250 mM imidazole. Protein that was close to a one-to-one ratio was further purified by SEC using a Superdex 200 increase 10/300 or Superdex 16/60 column (GE Healthcare) with SEC buffer (20-25 mM Tris pH 8, 150-300 mM NaCl, 2 mM βME).

E. coli Artic Express cells were co-transformed with the modified pET-28-Sumo-His_6-BECN2 CCD and pMBP parallel1- MBP-UVRAG CCD expression plasmids and grown at 37 °C in LB medium with 15 µg/mL kanamycin and 100 µg/mL ampicillin plate to select for colonies that contain the pET-28-Sumo-His_6-BECN2 CCD and pMBP parallel1- MBP-UVRAG CCD vector. A single colony was grown in LB medium with 15 µg/mL kanamycin and 100 µg/mL ampicillin at 37 °C to an OD_{600}= 0.7, prior to equilibrating the temperature to 13 °C. After the temperature was equilibrated to the lower temperature, protein expression was induced by the addition of 0.5 mM IPTG and expression overnight. Cells were harvested by centrifugation at 4000 x g for 15 minutes at 4 °C, cells were then resuspended in buffer, and pelleted into 50 mL conical tubes at 4 °C prior to storage at -80 °C. Frozen cell pellets were thawed and resuspended in 50 mL of lysis buffer (20 mM Tris pH 8, 150 mM NaCl, 25 mM

Imidazole, 2 mM βME, or 50 mM HEPES pH 7.5, 150 mM NaCl, 25 mM Imidazole). Buffers were optimized to find the best buffer for complex stability. A protease inhibitor cocktail tablet (Bimake) was added to the resuspended cells. Resuspended cells were lysed using NanoDeBEE emulsifier (BEE International) or by a Bronson 459 sonifier (Bronson). The lysate was centrifuged at 20,000 x g for 30 minutes to pellet cell debris and clarify the lysate. At each stage of purification, protein purity was evaluated by SDS-PAGE stained with Coomassie Blue.

The clarified lysate was purified by Ni^{++}-NTA affinity chromatography using a 5 mL of Ni^{++}-NTA resin column (Thermo Fisher Scientific). The column was washed with 30 column volumes of wash buffer (20 mM Tris pH 8, 150 mM NaCl, 2 mM βME, 25 mM Imidazole or 50 mM HEPES pH 7.5, 150 mM NaCl, 25 mM Imidazole). Protein was eluted from the Ni^{++}-NTA resin with wash buffer with the addition of 250 mM Imidazole. The complex was further purified by binding to amylose affinity resin, and washing the column with 30 column volume wash buffer (20 mM Tris pH 8, 150 mM NaCl, 2 mM βME). The complex was eluted from the amylose column with wash buffer with the addition of 20 mM maltose. Elution fractions that appeared to contain Sumo-His_6-BECN2 CCD and MBP-UVRAG in a one-to-one ratio, as indicated by SDS-PAGE were pooled and purified further by SEC using Superdex 200 increase 10/300 or Superdex 16/60 column (GE Healthcare) in SEC buffer (20 mM Tris pH 8, 150 mM NaCl, 2 mM βME).

Reverse pull-down assays were performed by co-expressing Sumo-His_6-BECN2 CCD and MBP-UVRAG, harvesting cells, and preparing clarified cell lysate, as described above. The clarified lysate was purified by amylose affinity chromatography using a 10 mL of amylose resin column (NEB BioLab). The column was washed with 30 column volumes of wash buffer (20 mM Tris pH 8, 150 mM NaCl, 2 mM βME). Protein was eluted from the amylose resin with

wash buffer with the addition of 20 mM maltose. The complex was added to a Ni^{++}-NTA affinity chromatography column and washed with 30 column volumes of wash buffer (20 mM Tris pH 8, 150 mM NaCl, 2 mM βME, 20 mM Imidazole). The protein was eluted from the Ni^{++}-NTA resin with wash buffer with the addition of 250 mM Imidazole. Elution fractions that appeared to contain Sumo-His_6-BECN2 CCD and MBP-UVRAG in a one-to-one ratio, as indicated by SDS-PAGE were pooled and further purified by SEC using Superdex 200 10/300 column (GE Healthcare) in SEC buffer (20 mM Tris pH 8, 150 mM NaCl, 2 mM βME).

3.2.4. ITC

ITC experiments were performed using a Low Volume Nano ITC (TA Instruments). All ITC experiments were performed at 20 °C with 20 injections of 2.5 µL each, with a stirring rate of 200 RPMs. The Sumo-His_6-BECN2 CCD and MBP-UVRAG CCD samples were loaded into separate dialysis cassettes, then co-dialyzed against the ITC buffer consisting of 50 mM Tris pH 8, 150 mM NaCl, and 2 mM βME. 200 µM MBP-UVRAG CCD was loaded into the syringe and titrated into the cell containing the 60 µM Sumo-His_6-BECN2 CCD. Blank profiles obtained by titrating buffer into buffer were subtracted from the experimental profiles. Data were analyzed using the NanoAnalyze Software (TA Instruments) using a blank constant model, a model that takes into consideration the heat of dilution, and an independent binding model.

3.3. Results

3.3.1. Expression and Purification of MBP-UVRAG CCD

MBP-UVRAG CCD fusion protein was purified by amylose affinity chromatography followed by SEC. The SEC elution profile contains two distinct peaks at 8.7 mL and 17 mL, each with a trailing edge shoulder (Figure 3.2). The 8.7 mL peak is in the void volume and likely contains aggregated protein.

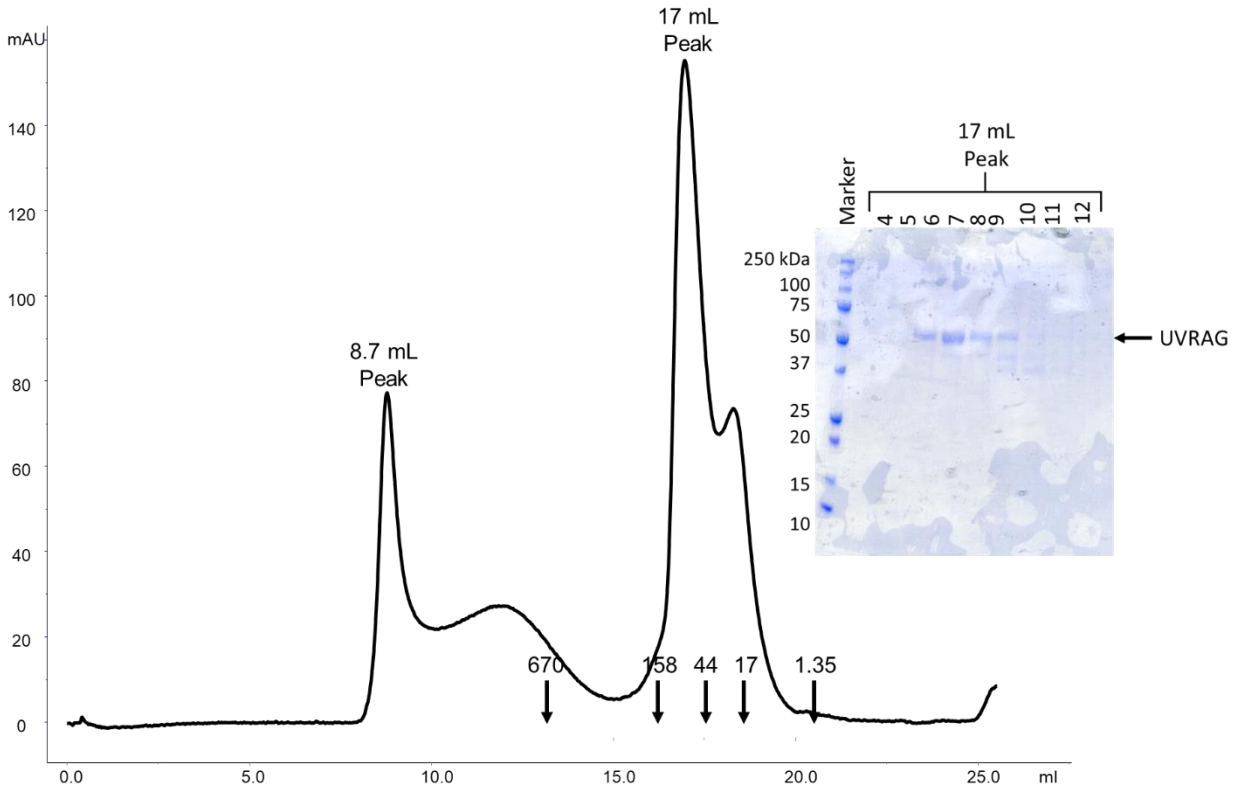

Figure 3.2: Size exclusion chromatogram and Coomassie-stained SDS-PAGE gel of MBP-UVRAG CCD. The elution positions of SEC Superose 6 increase 10/300 standards are indicated by arrows and corresponding molecular weight.

SDS-PAGE indicates that the 17 mL peak contains MBP-UVRAG CCD with the shoulder containing additional lower molecular weight contaminants. The molecular weight of the MBP-UVRAG CCD estimated from Kavg SEC is 51.5 kD, which is within error to the theoretical molecular weight of 51.7 kD for the MBP-UVRAG CCD calculated from the amino acid sequence. This suggests that MBP-UVRAG CCD is a monomer, and that it may not be stabilized as an elongated, helical CCD. The final yield of purified MBP-UVRAG CCD obtained from one liter of bacterial culture was 1.5 mg.

3.3.2. Expression and Purification of Sumo-His$_6$-BECN2 CCD

Sumo-His$_6$-BECN2 CCD fusion protein was purified by Ni^{++}-NTA affinity chromatography followed by SEC. The SEC elution profile contains a single peak eluting at 12.7 mL which contains Sumo-His$_6$-BECN2 CCD (Figure 3.3).

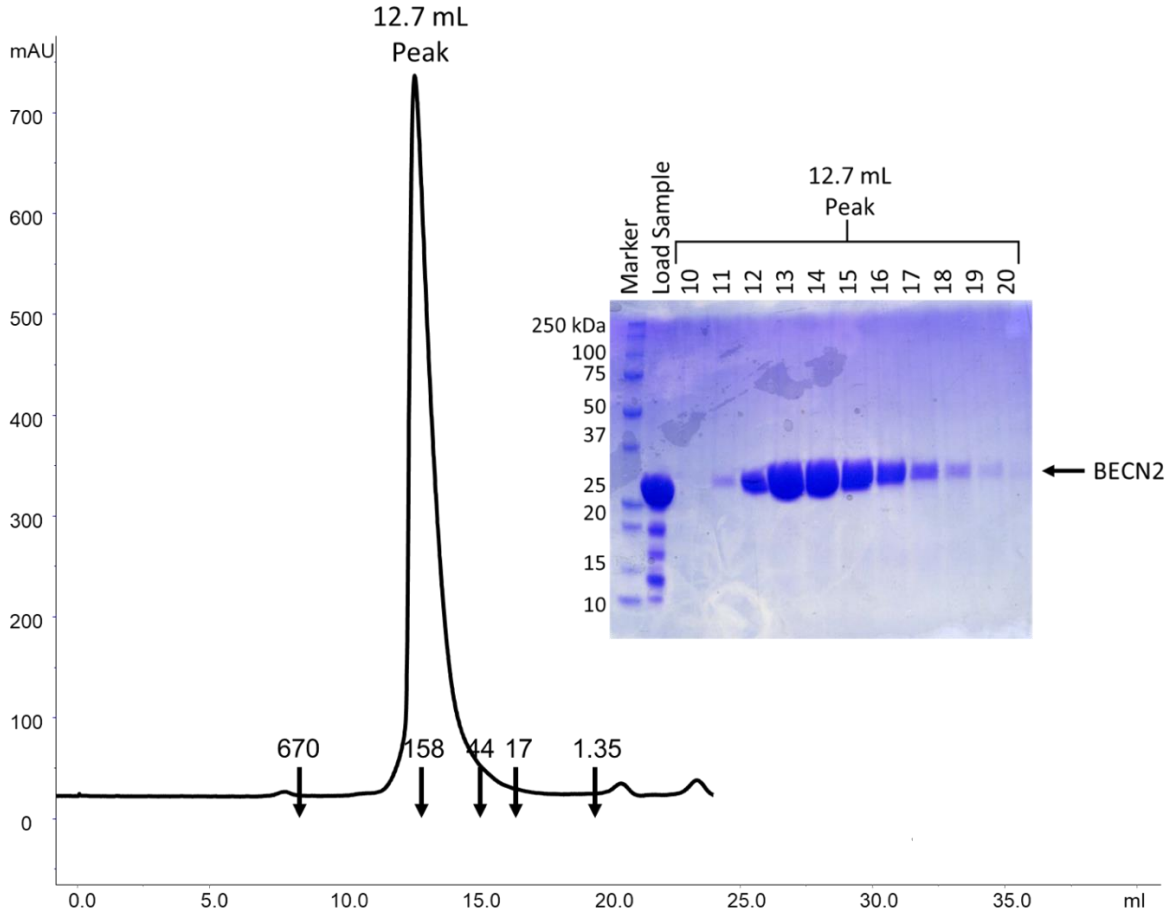

Figure 3.3: Size exclusion chromatogram and Coomassie-stained SDS-PAGE gel of Sumo-His$_6$-BECN2 CCD. The elution positions of SEC Superdex 200 increase 10/300 standards are indicated by arrows and corresponding molecular weight.

The molecular weight of the Sumo-His$_6$-BECN2 CCD estimated from Kavg is 99.6 kD, which is ~2.2 times larger than the theoretical molecular weight of 45 kD for the Sumo-His$_6$-BECN2 CCD homodimer calculated from the amino acid sequence. This suggests that Sumo-His$_6$-BECN2 CCD is an elongated homodimer. The final yield of the purified Sumo-His$_6$-BECN2 CCD obtained from one liter of bacterial culture was 1.1 mg.

3.3.3. Pulldown Assays

Affinity pulldowns were performed using Ni^{++}-NTA and amylose affinity resin to determine if the BECN2 CCD interacts with UVRAG CCD (Figure 3.4).

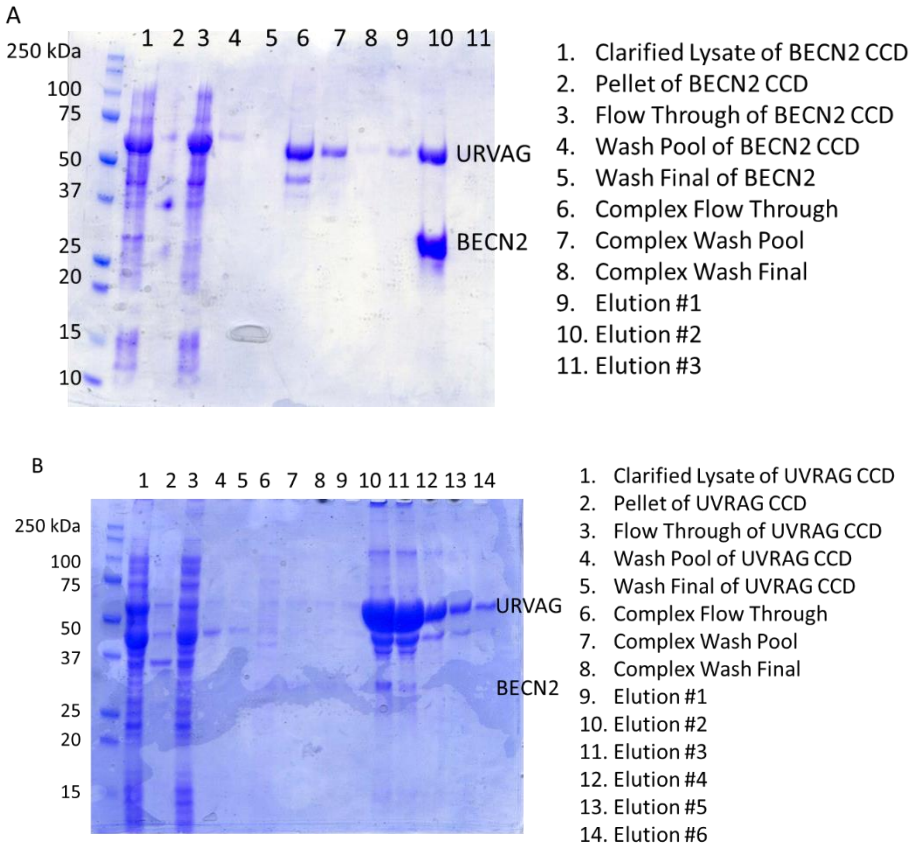

Figure 3.4: SDS-PAGE of the pulldown of MBP-UVRAG CCD and Sumo-His_6-BECN2 CCD. Samples loaded in each lane are indicated on the right. A) Pulldown on Ni^{++}-NTA affinity. B) Pulldown on Amylose affinity.

The BECN2 and UVRAG CCD were found to interact on both Ni^{++}-NTA (Figure 3.4A) and amylose resin (Figure 3.4B). However, the two proteins do not stay in complex over SEC, as indicated by the multiple peaks in the SEC elution profile (Figure 3.5). SDS-PAGE indicates that Peak 1 contains MBP-UVRAG CCD and some MBP, peak 2 contains Sumo-His_6-BECN2 CCD, while peak 3 contains Sumo-His_6-BECN2 CCD and some MBP. This suggests that the BECN2 CCD and UVRAG CCD interact, but with a low affinity.

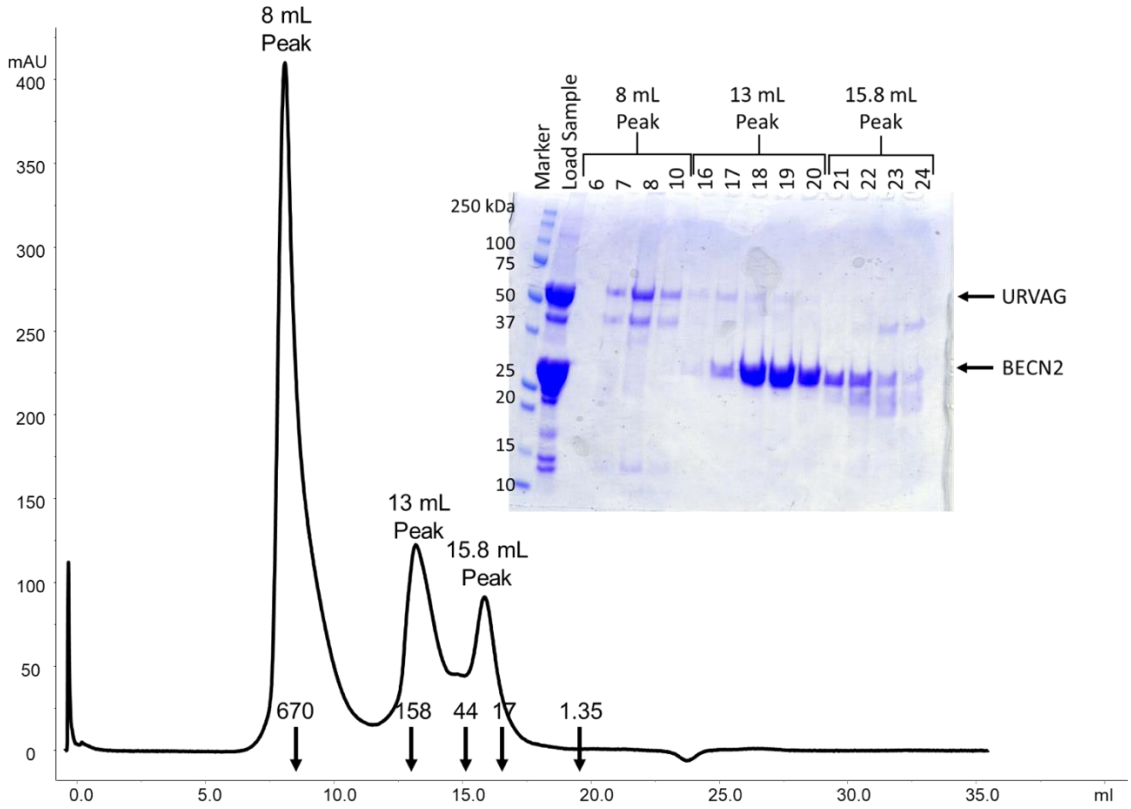

Figure 3.5: Size exclusion chromatogram and Coomassie-stained SDS-PAGE gel of MBP-UVRAG CCD and Sumo-His$_6$-BECN2 CCD complex. The elution positions of SEC Superdex 200 10/300 standards are indicated by arrows and corresponding molecular weight.

3.3.4. ITC

We used ITC to quantify affinity of interaction between BECN2 CCD and UVRAG CCD. The two proteins bind with a Kd of 1.44 µM, a stoichiometry of 0.772, ΔH of -7.225 kJ/mol and a ΔS of 87.16 J/mol *K (Figure 3.6). These are preliminary results, as the concentrations of the proteins still need to be optimized, and triplicate measurements recorded to verify the thermodynamics of the interaction.

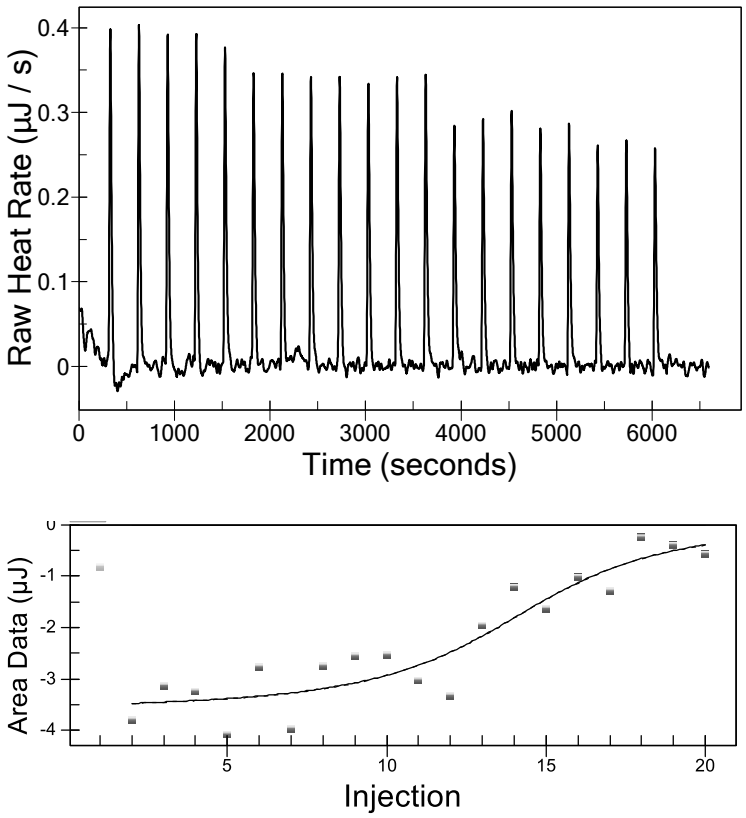

Figure 3.6: ITC profile of MBP-URAG CCD titrate into Sumo-His_6-BECN2 CCD.

3.4. Conclusion and Discussion

The *in vitro* analyses using purified proteins reported here shows that BECN2 and UVRAG CCDs interact. Unfortunately, as the complex dissociated upon SEC, the interaction was not strong enough to purify homogeneous complex for further biophysical and structural studies. This is somewhat unexpected as our initial ITC measurement indicates that the interaction affinity is ~1 µM, which should be sufficient to allow co-purification by SEC. Previous coimmunoprecipitation experiments using full-length proteins showed that BECN2 pulls down UVRAG[5]. It is likely that additional BECN2 and UVRAG domains further stabilize the interaction, and it is also possible that other proteins also facilitate the interaction.

As this research was being performed, a paper was published by Sheuai Wu et al 2018[60], that investigated the BECN1 and UVRAG interaction and reported the 1.8 Å crystal structure of

BECN1 and UVRAG. As we had found, they also report that mixing the BECN1 CCD and UVRAG CCD was insufficient for crystallizing the complex. However, they were able to stabilize the complex by cross-linking using a $(Glycine\text{-}Serine)_5$ linker to tether the BECN1 CCD to the UVRAG CCD. They also report that BECN1 residues 178-227, corresponding to the N-terminal half of BECN1 CCD, bind to the UVRAG CCD comprising residues 228-275, with a binding affinity of 7.6 μM[60].

This paper was published as our work was in the preliminary stages, therefore this project was not pursued any further.

CHAPTER 4. DETERMINING THE INTERACTIONS OF THE TAB2 AND TAB3 CCDS WITH BECN2 CCD

4.1. Introduction

TAB2 and TAB3 play an essential role in the activation of TAK1 response to inflammatory cytokines such as interleukin-1 (IL-1) and tumor necrosis factor-α (TNF)[61, 62]. TAB2 and TAB3 contain a C-terminal CCD and a Zn^{2+} Finger domain (Figure 4.1)[61, 62]. The TAB2 CCD interacts with the C-terminus of TAK1, which also contains a CCD (Figure 4.1)[63, 64]. TAK1 is a member of the MAP3K family and has been shown to function in many different signaling pathways. This function often requires interaction with TAB2/3[62].

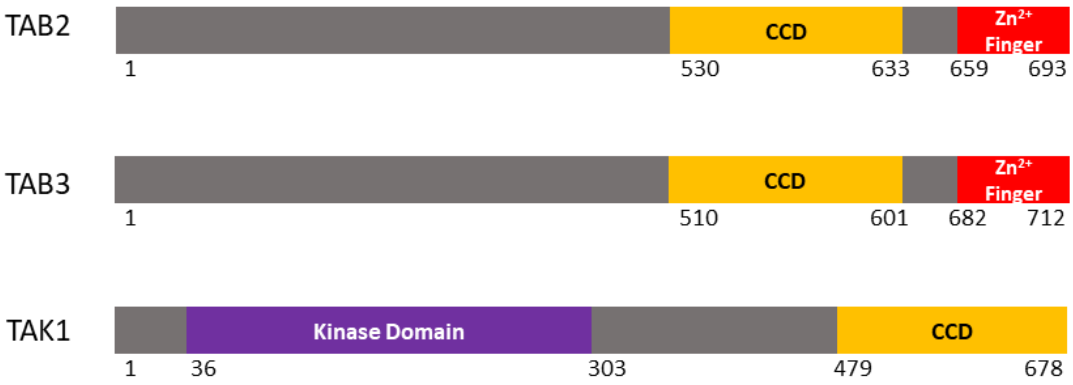

Figure 4.1: Domain architecture of TAB2, TAB3 and TAK1. Gray: disorder regions, Yellow: CCD, Red: Zn^{2+} Finger domain, and purple: Kinase domain.

Coimmunoprecipitation experiments show that TAB2 interacts with TAK1 residues 479-579[62]. GST pull-down assays show that TAB2 residues 574 to 653 interact with TAK1. ITC showed that TAK1 residues 479 - 579 and TAB2 residues 574 - 693 interact in a 1:1 ratio with a binding constant of 65 μM as determined by ITC[62]. Coimmunoprecipitation experiments show that the same TAK1 residues also interact with TAB3[62]. Lastly, the interaction between TAK1 and either TAB2 or TAB3 is required for the TAK1-dependent activation of the NF-κB

pathway[62, 63, 65]. The TAB2:TAK1 complex also plays an essential role in both IL-1 and TNF signaling[62].

Yeast-two hybrid assays show that TAB2 residues 526-657 and TAB2 residues 518-608 are sufficient for interaction with BECN1, and TAB2 and TAB3 interact with BECN1 residues 150-278[17], which includes the BECN1 CCD. TAB2 and TAB3 appear to be endogenous inhibitors of autophagy, as the number of GFP-LC3^{+} puncta, representing autophagosomes, increase upon knockdown of TAB2 or TAB3[17]. Thus, TAB2 and TAB3 bind BECN1 to inhibit autophagy, but upon autophagy induction by starvation or mTOR activation, TAB2 and TAB3 dissociate from BECN1 to interact with TAK1, which further stimulates autophagy through TAK1-IKK signaling via the NF-κB pathway[17, 66]. Thus, TAB2 and TAB3 play a dual role in controlling the autophagy switch[66], and also facilitate crosstalk between autophagy and TAK1-IKK signaling[17].

The interaction of BECN2 with TAB2 and/or TAB3 has not been investigated. However, as many BECN1-interacting proteins have been found to also interact with BECN2, we investigated whether TAB2 and/or TAB3 also interact with BECN2. Since BECN1 interacts via its CCD with the CCDs of TAB2 and TAB3, we tested the BECN2 CCD for interaction. Understanding similarities and differences in interactions of BECN1 and BECN2 with different interaction partners such as TAB2 and/or TAB3 will provide information regarding the divergent role of these homologs and help explain why mammals have two BECN paralogs. Therefore, we purified the BECN2 and TAB2 CCDs, and used affinity pull down assays to determine if they interact. We used ITC to determine the thermodynamics of this interaction and SEC-SAXS to investigate and compare the solution structure of the complex with that of the individual proteins. In order to understand the atomic details of the interaction, we also attempted to

determine the high-resolution structure of the complex but were unable to grow diffraction-quality crystals.

4.2. Materials and Methods

4.2.1. Creation of Protein Expression Constructs

The BECN2 CCD was expressed as a fusion protein, including a small ubiquitin-like modifier (SUMO), TEV-protease site, and His_6-tag preceding the protein, from the pET28-Sumo-TEVsite-His_6-BECN2 CCD expression vector as described previously[20].

The TAB2 CCD (residues 526-620) and the TAB3 CCD (residues 514-601) were cloned into the pMBP parallel 1 expression vector between EcoRI & XhoI restriction endonuclease sites by Mr. Samuel Wyatt, to enable expression and purification as MBP-fusion proteins.

4.2.2. Expression and Purification of BECN2, TAB2 and TAB3

The BECN2 CCD constructs were expressed and purified as described in Chapter 3.

E. coli BL21(DE3)pLysS cells were transformed with the pMBP parallel 1 MBP-TAB2 CCD expression vector, and grown at 37 °C in LB medium with 100 µg/mL ampicillin plates to select colonies that contain the pMBP parallel1- MBP-UVRAG CCD vector. A single colony was grown in LB medium with 100 µg/mL ampicillin at 37 °C to an OD_{600}=0.7, prior to equilibrating the temperature to 20 °C.

E. coli Artic Express cells were transformed with pMBP parallel 1 MBP-TAB3 CCD expression vector and grown at 37 °C in LB medium with 100 µg/mL ampicillin plates to select colonies that contain the pMBP parallel 1 MBP-TAB3 CCD vector. A single colony was grown in LB medium with 100 µg/mL ampicillin at 37 °C to an OD_{600}=0.7, prior to equilibrating the temperature to 13 °C.

In each case, after the temperature was equilibrated to the lower temperature, protein expression was induced by the addition of 0.5 mM isopropyl thio-β-D-galactoside (IPTG) and expressed overnight. Cells were harvested by centrifugation at 4000 x g for 15 minutes, cells were then resuspended in buffer, and pelleted into 50 mL conical tubes at 4 °C prior to storage at -80 °C. Pellets from a 1.5 L cell culture were resuspended in 50 mL of 25 mM Tris pH 8, 150 mM NaCl, 2 mM βME buffer with the addition of a protease inhibitor cocktail tablet (Bimake). Resuspended cells were lysed using a NanoDeBEE emulsifier (BEE International) or a sonicator. The lysate was centrifuged at 20,000 x g for 30 minutes to pellet down cell debris and clarify the lysate. At each subsequent stage of purification, protein purity was evaluated by SDS-PAGE stained with Coomassie Blue.

The MBP-TAB2 CCD fusion protein was purified from the clarified lysate by amylose affinity chromatography using a 10 mL of amylose resin column (NEB BioLab). The column was washed with 30 column volumes of wash buffer (25 mM Tris pH 8, 150 mM NaCl, 2 mM βME). Protein was eluted from the amylose resin with wash buffer with the addition of 20 mM maltose. Pooled fractions were concentrated to 18.9 mg/mL before SEC. Final purification was achieved by injecting 0.5 mL over a Superdex 200 increase 10/300 SEC column (GE Healthcare) equilibrated with wash buffer and eluted using an isocratic gradient. Absorbance at 280 nm was monitored and 1 mL fractions were collected during the course of the elution. Purified protein was concentrated to 21 mg/mL using a 30 kD Amicon Ultra-4 centrifugal concentrator (MilliporeSigma), flash-frozen in 25 µL aliquots dropwise into liquid N_2 and stored at -80 °C.

The MBP-TAB3 CCD was expressed and purified in a similar manner to MBP-TAB2 CCD. However, the last stage of purification, SEC, was performed using a Superose 6 increase column (GE Healthcare) equilibrated with SEC buffer (25 mM Tris pH 8, 150 mM NaCl, 2 mM

βME) eluted using an isocratic gradient. The Superose 6 increase column was used because MBP-TAB3 CCD had increased aggregation compared to MBP-TAB2 CCD. Absorbance at 280 nm was monitored and 1 mL fractions were collected during the course of the elution. Purified protein was concentrated to 10 mg/mL using a 30 kD Amicon Ultra-4 centrifugal concentrator (MilliporeSigma), flash-frozen in 25 µL aliquots dropwise into liquid N_2 and stored at -80 °C.

4.2.3. Expression and Purification of the TAB2:BECN2 CCD Complex

The MBP-TAB2 CCD:Sumo-His_6-BECN2 CCD complex was obtained by mixing separately purified proteins. Sumo-His_6-BECN2 CCD was expressed and purified as described above. The MBP-TAB2 CCD was expressed and then purified on the amylose column until the wash step, as described above, but was not eluted from the column. Instead, after the wash, Sumo-His_6-BECN2 CCD was added to the amylose resin-bound MBP-TAB2 CCD, in as close to a 1:1 molar ratio as could be estimated, and allowed to complex overnight at 4 °C, after the resin was stirred. MBP-TAB2 CCD:Sumo-His_6-BECN2 CCD complex bound to the amylose resin was washed with 10 column volume wash buffer (25 mM Tris pH 8, 150 mM NaCl, 2 mM βME) to remove unbound protein. The complex was eluted from the amylose column with wash buffer with the addition of 20 mM maltose, as well as 25 mM Imidazole. The complex was further purified using Ni^{++}-NTA affinity chromatography using a 5 mL Ni^{++}-NTA resin column (Thermo Fisher Scientific) and washed with 10 column volumes of wash buffer (25 mM Tris pH 8, 150 mM NaCl, 2 mM βME, 25 mM Imidazole). The complex was eluted from the Ni^{++}-NTA column with wash buffer with the addition of 250 mM Imidazole. Pooled fractions were concentrated to 13.9 mg/mL before SEC. Final purification was achieved by injecting 0.5 mL over a Superdex 200 increase 10/300 SEC column (GE Healthcare) equilibrated with wash buffer and eluted using an isocratic gradient. Absorbance at 280 nm was monitored and 1 mL

fractions were collected during the course of the elution. Purified protein was concentrated to 10.2 mg/mL using a 30 kD Amicon Ultra-4 centrifugal concentrator (MilliporeSigma), flash-frozen in 25 µL aliquots dropwise into liquid N_2 and stored at -80 °C.

The cleaved TAB2 CCD:His_6-BECN2 CCD complex was purified as described for the MBP-TAB2 CCD:Sumo-His_6-BECN2 CCD complex, but instead of complexing overnight, after the resin was stirred, it was complexed at 4 °C for 1 hour, in order to perform overnight cleavage in same day. The complex was washed with 10 column volumes of wash buffer (25 mM Tris pH 8, 150 mM NaCl, 2 mM βME), then subjected to overnight, on-column cleavage by adding glutathione S-transferase (GST)-TEV protease at 4 °C, to remove the MBP and Sumo tags. The complex was washed from the amylose column with wash buffer (25 mM Tris pH 8, 150 mM NaCl, 2 mM βME, 25 mM Imidazole), then passed over Glutathione Sepharose resin (Thermo Fisher Scientific) to remove excess GST-TEV protease, then further purified using Ni^{++}-NTA affinity chromatography. The column was washed with 10 column volumes of wash buffer, and the complex eluted using wash buffer with the addition of 250 mM Imidazole. Pooled fractions were concentrated to 14.5 mg/mL before SEC. Final purification was achieved by injecting 0.5 mL over a Superdex 200 increase 10/300 SEC column (GE Healthcare) equilibrated with SEC buffer (25 mM Tris pH 8, 150 mM NaCl, 2 mM βME) and eluted using an isocratic gradient. Absorbance at 280 nm was monitored and 1 mL fractions were collected during the course of the elution. Purified protein was concentrated to 9.3 mg/mL using a 10 kD Amicon Ultra-4 centrifugal concentrator (MilliporeSigma), flash-frozen in 25 µL aliquots dropwise into liquid N_2 and stored at -80 °C.

4.2.4. Expression and Purification of TAB3 CCD:BECN2 CCD Complex

We first attempted to obtain the MBP-TAB3 CCD:Sumo-His_6-BECN2 CCD complex using a protocol similar to that used for purification of the MBP-TAB2 CCD:Sumo-His_6-BECN2 CCD complex. However, as a very little amount of complex was obtained, we were unable to perform SEC, therefore, we attempted to purify the complex by co-expressing the two proteins.

E. coli Artic Express cells were transformed with pMBP parallel 1 MBP-TAB3 CCD and pET28-Sumo-TEVsite-His_6-BECN2 CCD expression vector and grown at 37 °C in LB medium with 25 µg/mL kanamycin and 100 µg/mL ampicillin plates to select of colonies that contain the pMBP parallel 1 MBP-TAB3 CCD and pET28-Sumo-TEVsite-His_6-BECN2 CCD vector. A single colony was grown in LB medium with 100 µg/mL ampicillin at 37 °C to an OD_{600}=0.7, prior to equilibrating the temperature to 13 °C. After the temperature was equilibrated to the lower temperature, protein expression was induced by the addition of 0.5 mM isopropyl thio-β-D-galactoside (IPTG) and expressed overnight. Cells were harvested by centrifugation at 4000 x g for 15 minutes, cells were then resuspended in buffer, and pelleted into 50 mL conical tubes at 4 °C prior to storage at -80 °C. Frozen cell pellets were thawed and resuspended in 50 mL lysis/wash buffer consisting of 20 mM Tris pH 8, 150 mM NaCl, 2 mM βME, 25 mM Imidazole, and a protease inhibitor cocktail tablet (Bimake) added. Resuspended cells were lysed using a NanoDeBEE emulsifier (BEE International) or by a Bronson 459 sonifier (Bronson). The lysate was centrifuged at 20,000 x g for 30 minutes to pellet cell debris and clarify the lysate. At each stage of purification, protein purity was evaluated by SDS-PAGE stained with Coomassie Blue. The clarified lysate was purified by Ni^{++}-NTA affinity chromatography on 5 mL Ni^{++}-NTA resin (Thermo Fisher Scientific). The column was washed with 30 column volumes of wash buffer. Protein was eluted from the Ni^{++}-NTA resin with wash buffer with the addition of 250 mM

Imidazole. The complex was then bound to a 10 mL amylose affinity column, and the column was washed with 30 column volume wash buffer (20 mM Tris pH 8, 150 mM NaCl, 2 mM βME). The complex was eluted from the amylose column with wash buffer with the addition of 20 mM maltose.

4.2.5. Mass Spectrometry

All analyses were performed using a Waters SYNAPT G2-Si High Resolution MS system controlled by MassLynx 4.2 Software. An ACQUITY I-class liquid chromatograph with BEH Amide column 2.1 x 50 mm, 1.7 µm. Samples were run with initial 99% phase A, 7 min 30 % Phase A, with an injection volume 5 µL. Mobile phase A was 0.1% FA in acetonitrile, B was 0.1% FA in water. The flow rate was 0.4 mL/min, and the column temperature was 25 °C.

The instrument was operated in the positive and negative ion V-mode. The capillary voltage was 1.5 kV, source temperature 120 °C, sample cone voltage 30 V, desolvation gas temperature 500 °C, desolvation gas flow 800 L/h, cone gas flow 50 L/h, and lock spray Leukine enkephalin. Scan time was 0.5 sec (1 sec total duty cycle) for a scan mass range 50 to 1000 m/z. The average mass of the intact protein was determined by MaxEnt, a function of MassLynx software.

4.2.6. ITC

The thermodynamics of the binding of Sumo-His_6-BECN2 CCD to MBP-TAB2 CCD proteins was assessed using ITC, performed using a Low Volume Nano ITC (TA Instruments). All ITC experiments were performed at 20 °C with 20 injections of 2.5 µL each, with a stirring rate of 200 RPMs, with at least three repeats per measurement. Prior to ITC, the Sumo-His_6-BECN2 CCD and MBP-TAB2 CCD samples were loaded into separate dialysis cassettes, then

co-dialyzed against ITC buffer consisting of 25 mM HEPES pH 7.5, 150 mM NaCl, and 2 mM βME.

232 µM of MBP-TAB2 CCD was loaded into the syringe and titrated into the cell containing 30 µM Sumo-His_6-BECN2 CCD. The reverse experiment was also performed, wherein 80 µM Sumo-His_6-BECN2 CCD was loaded into the syringe and titrated into the cell containing 24 µM MBP-TAB2 CCD.

ITC experiments to quantify binding of Sumo-His_6-BECN2 CCD and MBP-TAB3 CCD were performed in a similar manner, except that these samples were co-dialyzed against ITC buffer consisting of 50 mM HEPES pH 7.5, 150 mM NaCl, and 2 mM βME. 244 µM Sumo-His_6-BECN2 CCD was loaded into the syringe and titrated into the cell containing the 50 µM MBP-TAB3 CCD.

For experiments wherein Sumo-His_6-BECN2 CCD was titrated into the cell, a blank profile was obtained by titrating equal concentrations of Sumo-His_6-BECN2 CCD into ITC buffer in the cell. For experiments wherein MBP-TAB2 CCD was titrated into the cell, a blank profile was obtained by titrating buffer into buffer, as MBP-TAB2 CCD does not dissociate. Blank profiles were subtracted from the experimental profile prior to analyzing the data. All data were analyzed using the NanoAnalyze Software (TA Instruments), using a blank constant model and an independent binding model.

4.2.7. SAXS Data Collection and Analysis

SEC-SAXS data were recorded at beamline 18-ID Bio-CAT at APS, ANL, Argonne, IL with in-line SEC to separate sample from aggregates, thus ensuring optimal sample.

Purified proteins in 25 mM Tris pH 8.0, 150 mM NaCl, and 2 mM βME were loaded at a concentration of 8.8- 10.3 mg/mL column at a flow rate of 0.5 ml min^{-1} using an Infinity II 1260

HPLC (Agilent). The SEC eluate was passed through a UV monitor and then into the SAXS flow cell, a 1.0 mm ID quartz capillary with 50 μm walls using a co-flow sample geometry to prevent radiation damage[67].

Each sample was exposed to an X-ray beam of size 150 (h) x 25 (v) μm^2, wavelength 1.03 Å (12 keV energy) for 1 s/frame, with a periodicity of 1 s/frame, and the SAXS data were recorded on a Pilatus3 X 1M detector (Dectris) at a sample to detector distance of 3.6 m. The range of momentum transfer (q) accessed was $0.005\ Å^{-1} < q < 0.35\ Å^{-1}$. Commercially available glassy carbon plates were used as absolute intensity calibration standards for SAXS data collection (NIST SRM 3600). X-ray radiation damage was monitored by automated frame-by-frame comparison of relevant regions using CORMAP[68], which is implemented in BioXTAS RAW (version 1.6.4).

Scattering data were normalized to the transmitted X-ray beam intensity and scattering from buffer was subtracted using the BioXTAS RAW software (version 1.6.4)[69] prior to further analysis. Guinier fits were used to calculate the radius of gyration (R_g) and scattering at zero angle I(0), and dimensionless Kratky plots[70] were used to evaluate disorder within the samples. GNOM[71] was used to calculate the maximum particle size (D_{max}) and the indirect Fourier transform used to obtain the pairwise-distance distribution function, P(r)[72]. The P(r) function was also used to calculate the R_g and I(0). The molecular mass was calculated using the Volume of correlation (V_c) method[15] as implemented in RAW. Ab initio SAXS envelopes were calculated by applying ten cycles in DAMMIF[37], with subsequent analysis by DAMAVER and DAMFILT[38], to compare and identify the most probable model, align all models to the most probable model, average the aligned models, compute a probability map, and filter the averaged model.

4.2.8. Crystal Screening

The TAB2 CCD:His_6-BECN2 CCD complex was screened for crystallization at 20 °C using a Gryphon LCP crystal screen dispensing robot (Art Robbins Instruments). Two sparse matrix screens, the Microlytic screens MCSG 1-2 (Anatrace, Maumee, OH, USA), each of which includes 96 different reservoir solution compositions was tested, using a 3:1, 1:1, 1:3 v/v ratio of protein:reservoir solution (4.2 mg/mL to 9.3 mg/mL complex in 25 mM Tris pH 8, 150 mM NaCl, 2 mM βME). Thus, a total of 576 different conditions were screened for crystallization of this complex. Attempts were made to optimize potential hits using 24-well hanging-drop vapor diffusion experiments at 20 °C, using 4 µL drops of with protein:reservoir solution mixed in 3:1 or 1:1 v/v ratios. Optimization strategies include using varying concentrations of salts including magnesium sulfate from 1.2 M to 2.2 M, varying buffer pH, including 0.1 M Tris pH 7.5 to pH 9, and varying concentrations of protein complex. Only spherulites were obtained from these experiments, and these were used for microseeding experiments. Seed stocks were made by adding 2 µL of spherulite-containing drops to 18 µL of 0.1M Tris pH 8, 1.8M $MgSO_4$ buffer in an eppendorf, vortexing vigorously to break the spherulites into crystal "seeds". Seeding experiments tested magnesium sulfate concentration varying between 1.2 M to 1.7 M, and seed stock dilutions varying between 1:500 to 1:10000.

4.3. Results

4.3.1. Expression and Purification of TAB2 Constructs

MBP-TAB2 CCD fusion protein was purified by amylose affinity chromatography followed by SEC. The SEC elution profile consists of a single peak with a small trailing shoulder (Figure 4.2). SDS-PAGE shows that MBP-TAB2 CCD elutes within the peak, while the shoulder includes MBP-TAB2 CCD and lower molecular mass contaminants. The molecular mass of

MBP-TAB2 CCD estimated from Kavg was 198.2 kD, which is ~3.8 times larger than the theoretical molecular weight of 51.3 kD for the MBP-TAB2 CCD monomer calculated from the amino acid sequence. This suggests that MBP-TAB2 CCD is an elongated protein. The final yield of the purified MBP-TAB2 CCD obtained per liter of bacterial culture is 30 mg.

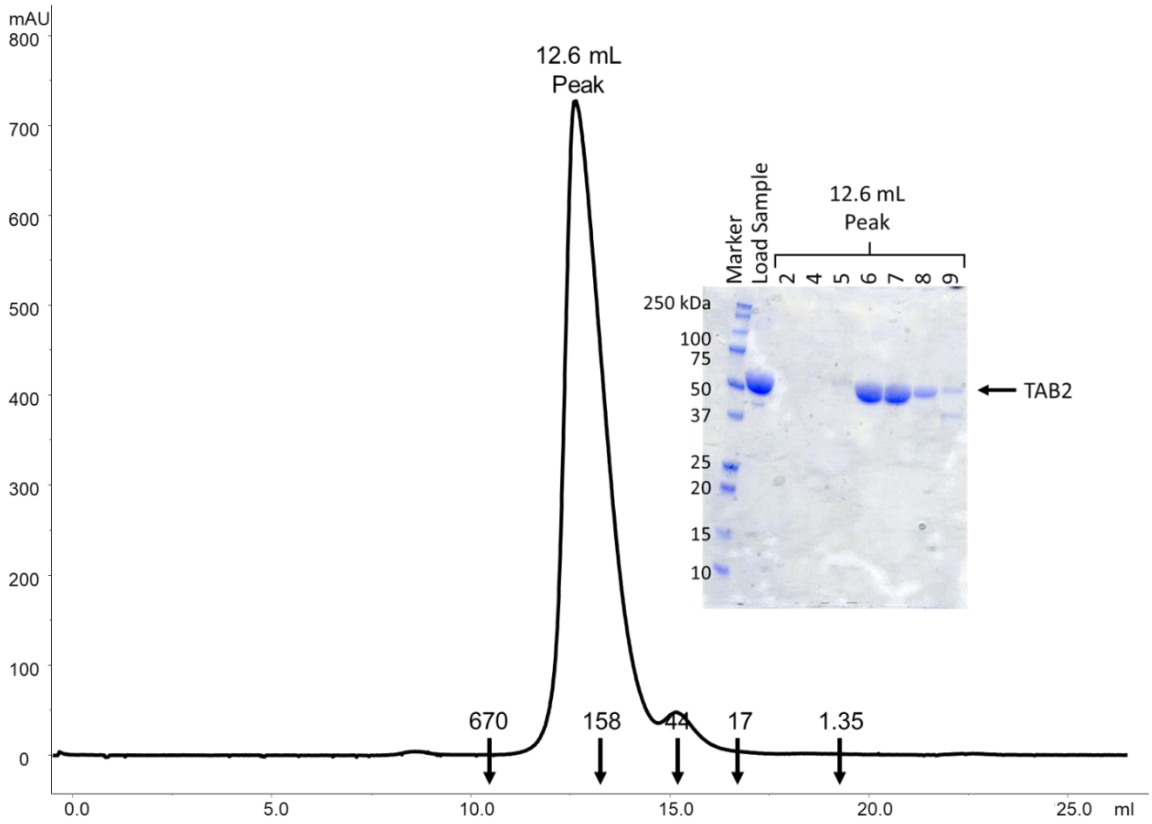

Figure 4.2: Size exclusion chromatogram and Coomassie-stained SDS-PAGE gel of MBP-TAB2 CCD. The elution positions of SEC Superdex 200 increase 10/300 standards are indicated by arrows and corresponding molecular weight.

4.3.2. Expression and Purification of TAB3 Constructs

MBP-TAB3 CCD fusion protein was purified by amylose affinity chromatography followed by SEC. The SEC elution profile contains 3 distinct peaks, and SDS-PAGE shows that MBP-TAB3 CCD is the major protein eluting within each of these peaks (Figure 4.3). As the first peak is in the void volume, while the second peak is at an elution volume that corresponds to a mass of 1039.9 kDa based on the SEC standard, it is likely that both peaks correspond to

aggregated protein. The molecular weight of the MBP-TAB3 CCD estimated from Kavg of the third peak is 89.1 kD, which is ~1.7 times larger than the theoretical molecular weight of 51.3 kD for the MBP-TAB3 CCD monomer calculated from the amino acid sequence. This suggests that MBP-TAB3 CCD is an elongated monomer. The final yield of the purified MBP-TAB3 CCD obtained from one liter of bacterial culture was 1.5 mg.

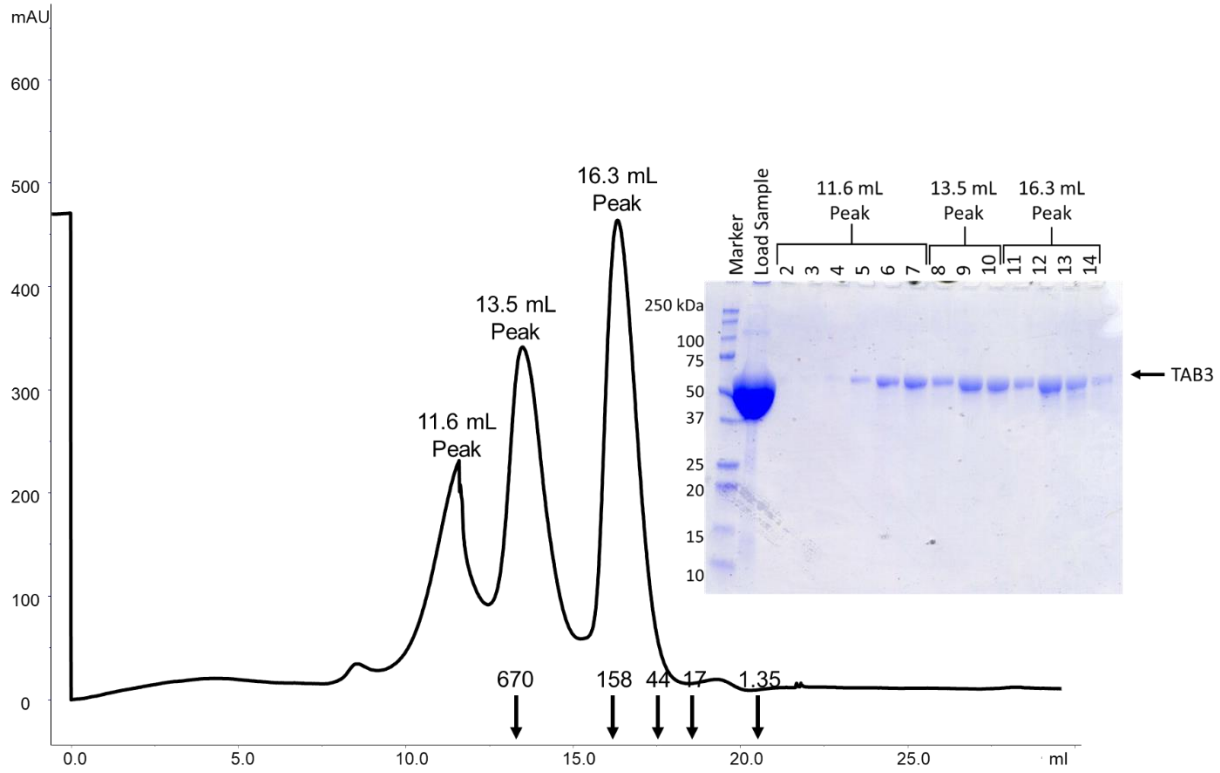

Figure 4.3: Size exclusion chromatogram and Coomassie-stained SDS-PAGE gel of MBP-TAB3 CCD. The elution positions of SEC Superdex 200 increase 10/300 standards are indicated by arrows and corresponding molecular weight.

4.3.3. Expression and Purification of BECN2:TAB2 Complex

The MBP-TAB2 CCD:Sumo-His_6-BECN2 CCD fusion complex was purified by Ni^{++}-NTA affinity chromatography and amylose affinity chromatography followed by SEC. The SEC elution profile contains a single peak, and SDS-PAGE shows that the eluted protein is the MBP-TAB2 CCD:Sumo-His_6-BECN2 CCD complex (Figure 4.4).

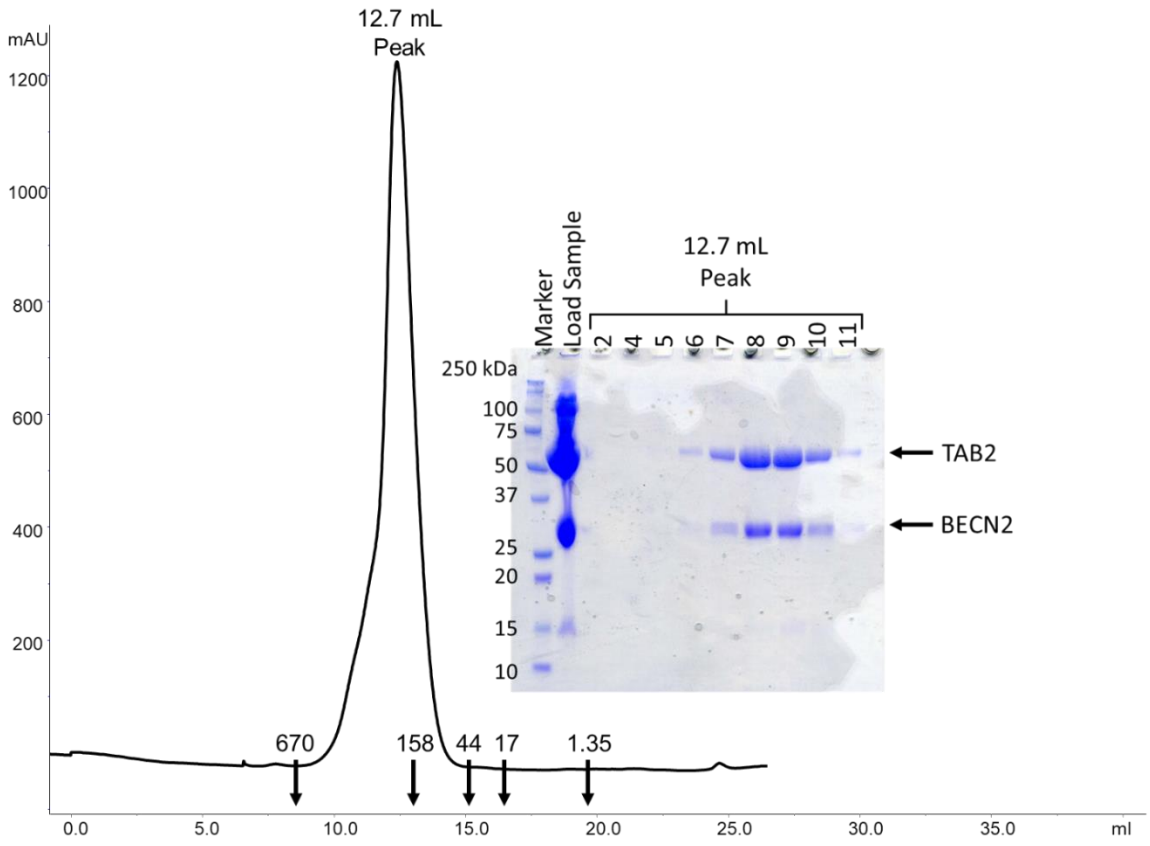

Figure 4.4: Size exclusion chromatogram and Coomassie-stained SDS-PAGE gel of MBP-TAB2 CCD:Sumo-His_6-BECN2 CCD complex. The elution positions of SEC Superdex 200 increase 10/300 standards are indicated by arrows and corresponding molecular weight

The molecular weight of the MBP-TAB2 CCD:Sumo-His_6-BECN2 CCD estimated from Kavg was 110.4 kD, which is ~1.5 times larger than the theoretical molecular weight of 74.3 kD for the MBP-TAB2 CCD:Sumo-His_6-BECN2 CCD heterodimer calculated from the amino acid sequence. This suggests that MBP-TAB2 CCD:Sumo-His_6-BECN2 CCD is an elongated heterodimer. 4.75 mg of purified MBP-TAB2 CCD:Sumo-His_6-BECN2 CCD complex was obtained from a 1.5 L culture expressing MBP-TAB2 CCD and 6L culture expressing Sumo-His_6-BECN2 CCD.

The TAB2 CCD:His_6-BECN2 CCD complex was purified by Ni^{++}-NTA affinity chromatography and amylose affinity chromatography followed by SEC. The SEC elution profile contains a single peak (Figure 4.5).

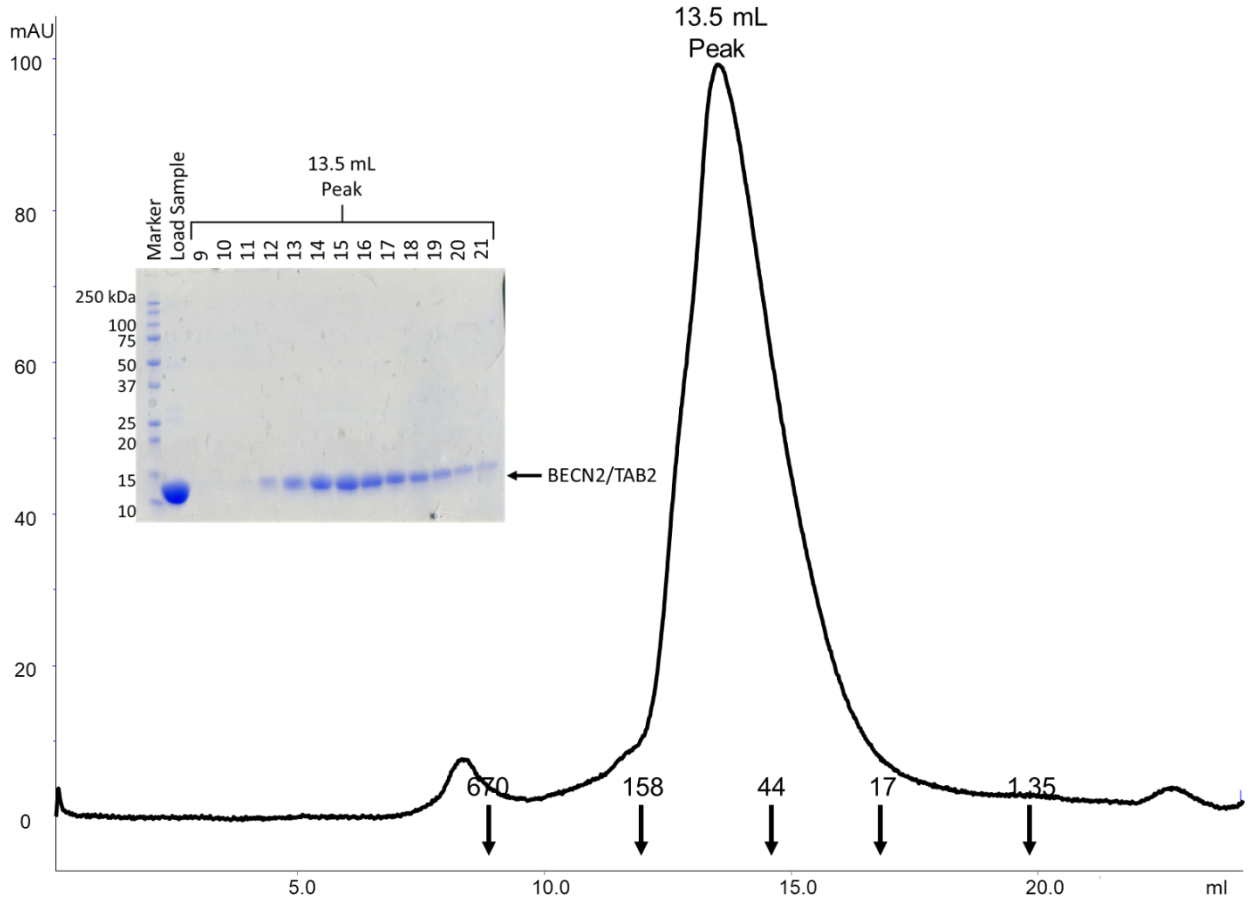

Figure 4.5: Size exclusion chromatogram and Coomassie-stained SDS-PAGE gel of TAB2 CCD:His_6-BECN2 CCD complex. The elution positions of SEC Superdex 200 increase 10/300 standards are indicated by arrows and corresponding molecular weight.

Since the TAB2 CCD and His_6-BECN2 CCD have similar mass the presence of both proteins could not be determined by SDS-PAGE (Figure 4.5). Therefore, mass spectrometry was used to determine if both proteins were present in the eluted sample. Regardless, based on the elution volume from SEC, the molecular mass of the eluted protein is 70.5 kD, which is ~3.3 times larger than the theoretical molecular weight of 21 kD for the TAB2 CCD:His_6-BECN2 CCD heterodimer calculated from the amino acid sequence. This suggests that TAB2 CCD:His_6-

BECN2 CCD is an elongated heterodimer. 6.8 mg of purified TAB2 CCD:His_6-BECN2 CCD complex was obtained from a 1.5 L culture expressing MBP-TAB2 CCD and a 6 L culture expressing Sumo-His_6-BECN2 CCD.

4.3.4. Mass Spectrometry of TAB2 CCD:His_6-BECN2 CCD Complex

His_6-BECN2 CCD and TAB2 CCD run at the same size on the SDS-PAGE, therefore we used electrospray ionization time-of-flight mass spectrometry (Figure 4.6) to verify that His_6-BECN2 CCD and TAB2 CCD were both present in the protein eluted from SEC. The first major peak seen in the mass spectrum corresponds to a mass of 11559.6 Da, which agrees very well with the theoretical molecular weight of 11559.2 Da for the TAB2 CCD (residues 526-620) along with the extra glycine at the N-terminus left after TEV-protease cleavage. The largest peak corresponds to a mass of 11852.4 Da, which agrees very well with the theoretical molecular weight of 11852.9 Da for the His_6-BECN2 CCD. Thus, both proteins were co-eluted in the SEC peak. The size of the peaks correlates to the relative amount of protein in the sample, indicating that the sample may contain more BECN2 CCD than TAB2 CCD. The mass spectrum also contains two other major peaks at 11635.6 Da and 11824.6 Da. The 11635.6 Da peak corresponds to the mass expected for TAB2 with an extra glycine residue, however the source of the glycine residue is unclear . The 11824.6 Da peak agrees with the addition of the combined mass of a glutamine and a phenylalanine to TAB2. Perhaps these residues are included in some of the TAB2 protein due to imperfect cleavage at the TEV protease site to remove the MBP tag, as the TEV cleavage site is Glu-Asn-Leu-Tyr-Phe-Gln-Gly. Alternately, the 11824.6 Da peak may correspond to the BECN2 CCD with a removal of one carbon and one oxygen.

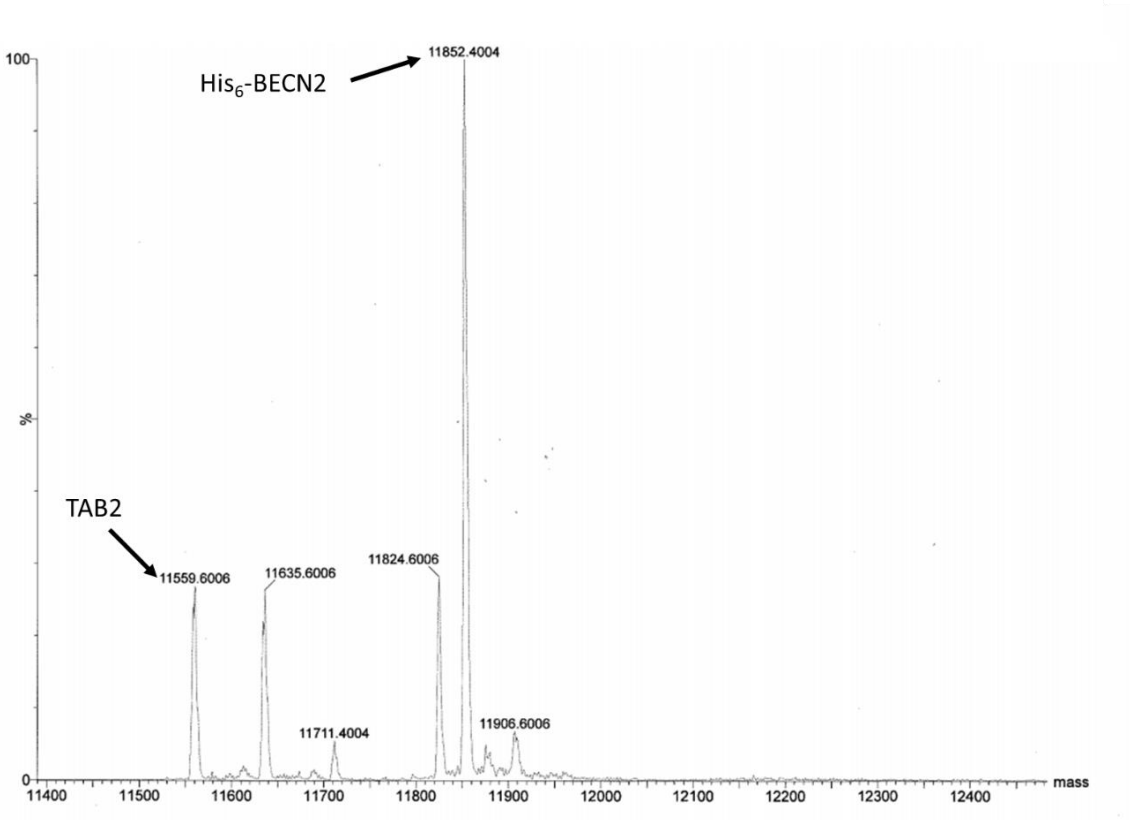

Figure 4.6: Mass Spectrum of the TAB2 CCD:His_6-BECN2 CCD SEC peak. Arrows indicate the peaks corresponding to each protein, indicating that both proteins are present in the sample.

4.3.5. Purification of Sumo-His_6-BECN2 CCD:MBP-TAB3 CCD

Attempts were made to purify the complex of BECN2 CCD with TAB3 CCD via Ni^{++}-NTA and Amylose affinity resin (Figure 4.7). Initially, partly purified BECN2 CCD and TAB3 CCD were used to perform Ni^{++}-NTA and Amylose affinity pull-down assays, similar to that used for affinity purification of the MBP-TAB2 CCD:Sumo-His_6-BECN2 CCD complex. While the complex co-eluted from both Amylose resin and Ni^{++}-NTA resin, the yield was too low for further purification using SEC (Figure 4.7 A and B). Subsequently the two proteins were co-expressed and co-purified via Ni^{++}-NTA and Amylose affinity pull-downs. While the BECN2 CCD and TAB3 CCD co-eluted from the Ni^{++}-NTA resin, the two proteins did not co-elute from the Amylose resin (Figure 4.7 C & D). We did not pursue this purification further.

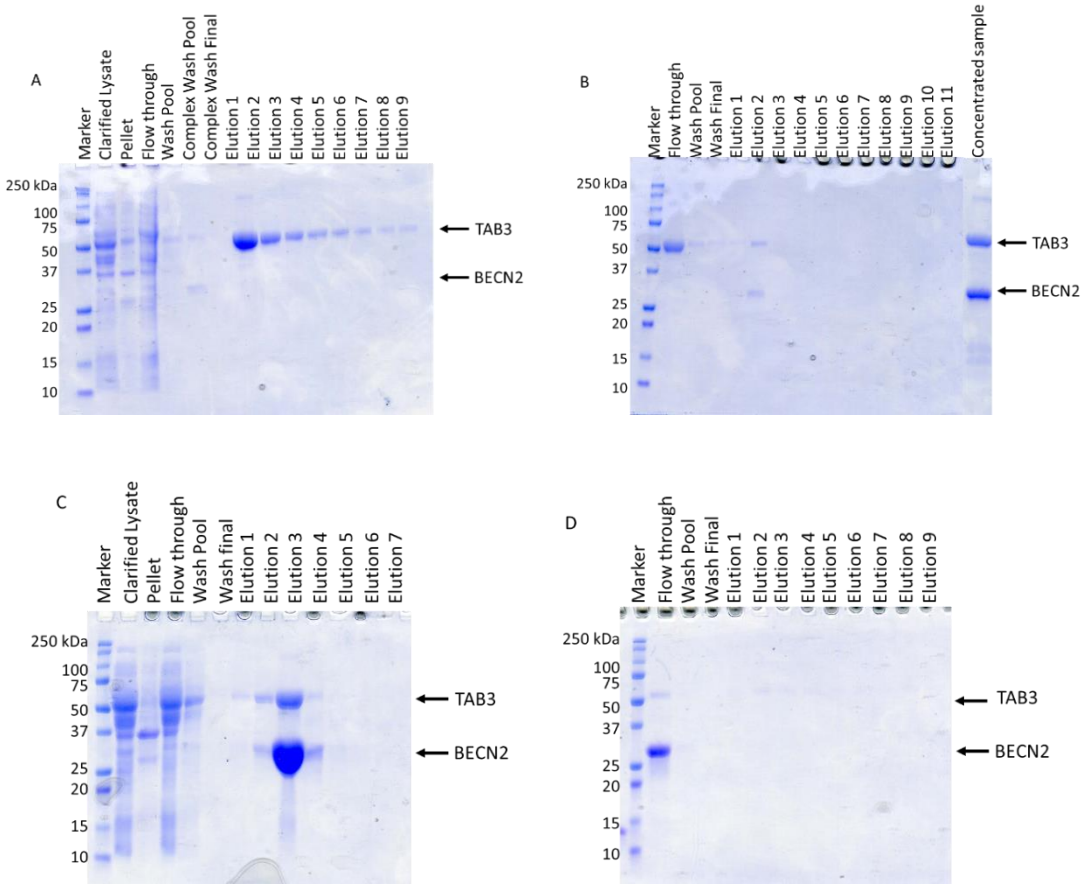

Figure 4.7: SDS-PAGE of MBP-TAB3 CCD and Sumo-His$_6$-BECN2 CCD Affinity Pulldowns. (A and B) Pulldowns using partly purified proteins. A) Amylose Affinity chromatography. B) Ni^{++}-NTA Affinity chromatography. (C and D) Pulldowns of co-expressed complex. C) Ni^{++}-NTA Affinity chromatography. D) Amylose Affinity chromatography.

4.3.6. ITC

We used ITC to quantify the thermodynamics of BECN2 CCD and TAB2 CCD binding. Titration of Sumo-His$_6$-BECN2 CCD into MBP-TAB2 CCD results in a K_d of 1.76 ±0.94 µM, with a stoichiometry of 0.413 ±0.019 (Figure 4.8 A, Table 4.1), while the reverse experiment wherein MBP-TAB2 CCD is titrated into Sumo-His$_6$-BECN2 CCD results in a binding constant of 6.53 ±0.78 µM, with a stoichiometry of 1.022 ±0.052 (Figure 4.8 B, Table 4.1). Perhaps this is because Sumo-His$_6$-BECN2 CCD is a homodimer at 80 µM in the syringe, but dissociates as it is titrated into the cell, as the K_d of Sumo-His$_6$-BECN2 CCD self-association is 134 µM (Figure 4.8

C, Table 4.1), similar to the published dissociation constant of BECN2 CCD of 138 ±6 μM[20] (Table 4.1).

Table 4.1: Thermodynamics of binding of Sumo-His_6-BECN2 CCD with MBP-TAB2 CCD, Sumo-His_6-BECN2 CCD with MBP-TAB3 CCD, and Sumo-His_6-BECN2 CCD.

	K_d (μM)	N	ΔH (kJ/mol)	ΔS (J/mol *K)
Sumo-His_6-BECN2 CCD into MBP-TAB2 CCD	1.76 ±0.94	0.413 ±0.019	-348.9 ±11.1	-1079.3 ±41.6
MBP-TAB2 CCD into Sumo-His_6-BECN2 CCD	6.53 ±0.78	1.022 ±0.052	-189.6 ±5.5	-537.0 ±19.4
Sumo-His_6-BECN2 CCD into MBP-TAB3 CCD	26.5	0.444	-98.82	-249.5
Sumo-His_6-BECN2 CCD dissociation	134		152.8	447.2
BECN2 CCD dissociation[20]	138± 6		120.7 ±7.4	492.7 ±25.4

Titration of Sumo-His_6-BECN2 CCD into MBP-TAB3 CCD results in a K_d of 26.5 μM (Figure 4.8 D, Table 4.1), with a stoichiometry of 0.444. This is likely due to the same reason as the Sumo-His_6-BECN2 CCD into MBP-TAB2 CCD, except that the Sumo-His_6-BECN2 CCD concentration is above the dissociation constant.

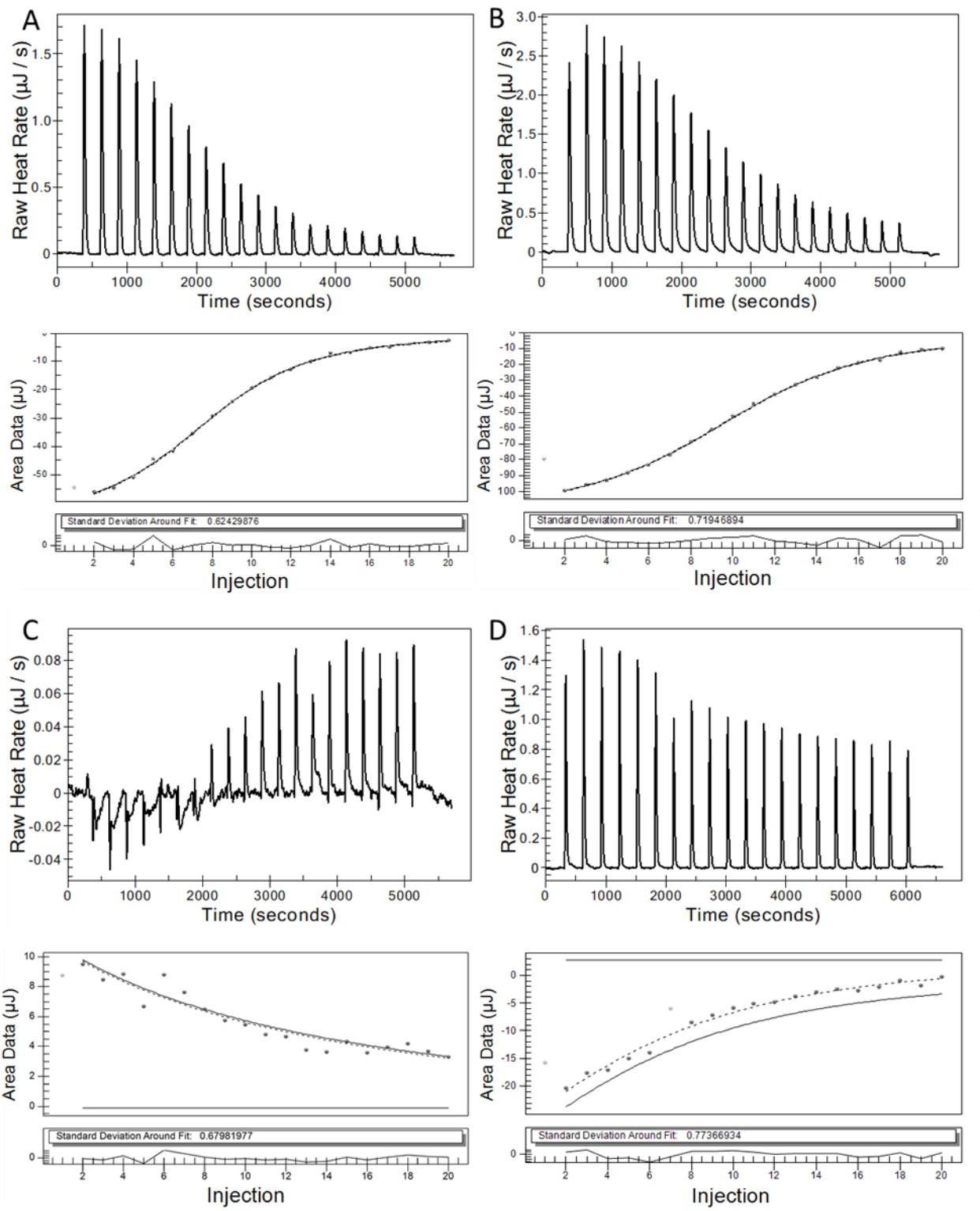

Figure 4.8: ITC binding profiles of A) Sumo-His_6-BECN2 CCD into MBP-TAB2 CCD. B) MBP-TAB2 into Sumo-His_6-BECN2 CCD. C) Dissociation of Sumo-His_6-BECN2 CCD. D) Sumo-His_6-BECN2 CCD into MBP-TAB3 CCD.

4.3.7. SAXS

We used SEC-SAXS to investigate the size, shape, and structure of the MBP-TAB2 CCD:Sumo-His_6-BECN2 CCD complex. The integrated scattering intensity across different scattering frames (Figure 4.9 A) trends similar to the SEC profile, including the presence of a trailing edge shoulder on the main peak. The uniform R_g distribution across the scattering frames corresponding to the peak, indicates elution of a homogenous species (Figure 4.9 B). These scattering frames were used for further analysis. The molecular weight calculated from the V_c is ~85.8 kD which is ~ 1.1 times larger than theoretical molecular weight. The R_g of the MBP-TAB2 CCD:Sumo-His_6-BECN2 CCD complex estimated from the Guinier plot and P(r) distribution is ~54 Å (Figure 4.9 C and D). Further, the shape of the P(r) distribution curve indicates that the MBP-TAB2 CCD:Sumo-His_6-BECN2 CCD complex has an elongated shape with a D_{max} of ~210 Å (Figure 4.9 D). The Kratky plot indicates that the MBP-TAB2 CCD:Sumo-His_6-BECN2 CCD complex is well-folded (Figure 4.9 E). The molecular envelope was not calculated as I felt it would provide limited information in the absence of atomic-resolution tagged structures.

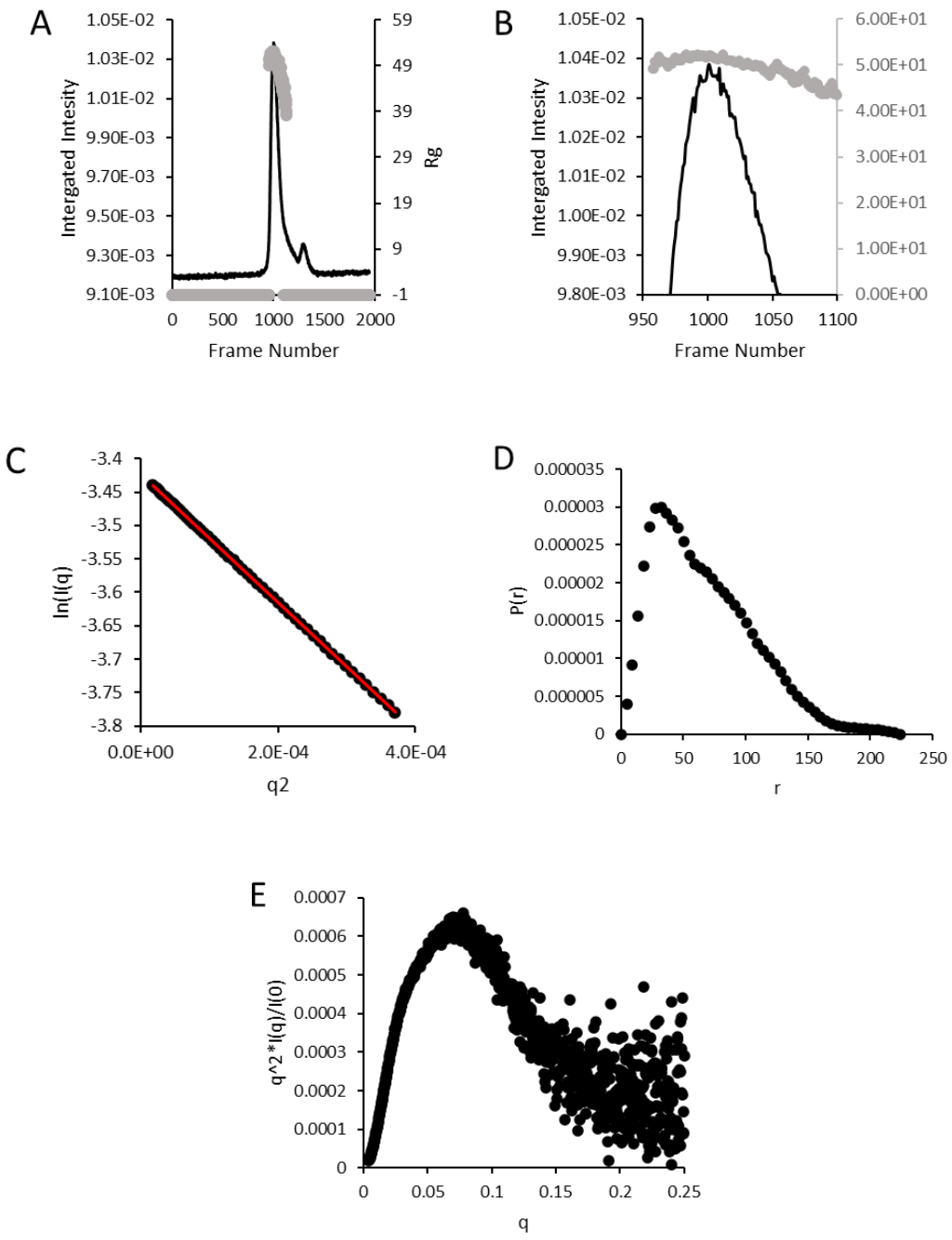

Figure 4.9: SAXS analysis of MBP-TAB 2 CCD:Sumo-His6-BECN2 CCD. A) Integrated intensity vs frame number in black and Rg vs frame number in grey. B) Zoomed in of (A) to see Rg values over top of peak. C) Guinier plot. D) P(r) pairwise distribution. E) Kratky plot.

We also used SEC-SAXS to investigate the size, shape, and the structure of the TAB2 CCD:His_6-BECN2 CCD. The integrated scattering intensity across different scattering frames (Figure 4.10 A) trends similar to the SEC profile, including the presence of a trailing edge

shoulder on the main peak. The uniform R_g distribution across the scattering frames corresponding to the peak, indicates elution of a homogenous species (Figure 4.10 B). These scattering frames were used for further analysis. The molecular weight calculated from the V_c is ~22.1 kD which is ~ 0.9 times the theoretical molecular weight (Figure 4.10 A and B). The R_g of the TAB2 CCD:His_6-BECN2 CCD complex estimated from the Guinier plot and P(r) distribution is ~38.3 Å (Figure 4.10 C and D). Further, the shape of the P(r) distribution curve indicates that the TAB2 CCD:His_6-BECN2 CCD complex has an elongated protein complex, with a D_{max} of ~125 Å (Figure 4.10 D). The Kratky plot indicates that the TAB2 CCD:His_6-BECN2 CCD is partially unfolded (Figure 4.10 E). An ab initio envelope was calculated from the SAXS data, which was fit with BECN2 CCD homodimer (PBD ID 5K7B) with χ^2 of 6.73 and 6.16, using FoXS and Crysol respectively (Figure 4.10 F). However, there is a bend in the envelope that is unoccupied by the BECN2 CCD homodimer, suggesting there may be a change in the curvature of the TAB2:BECN2 CCD heterodimer, or at least a kink within one helix in the heterodimer.

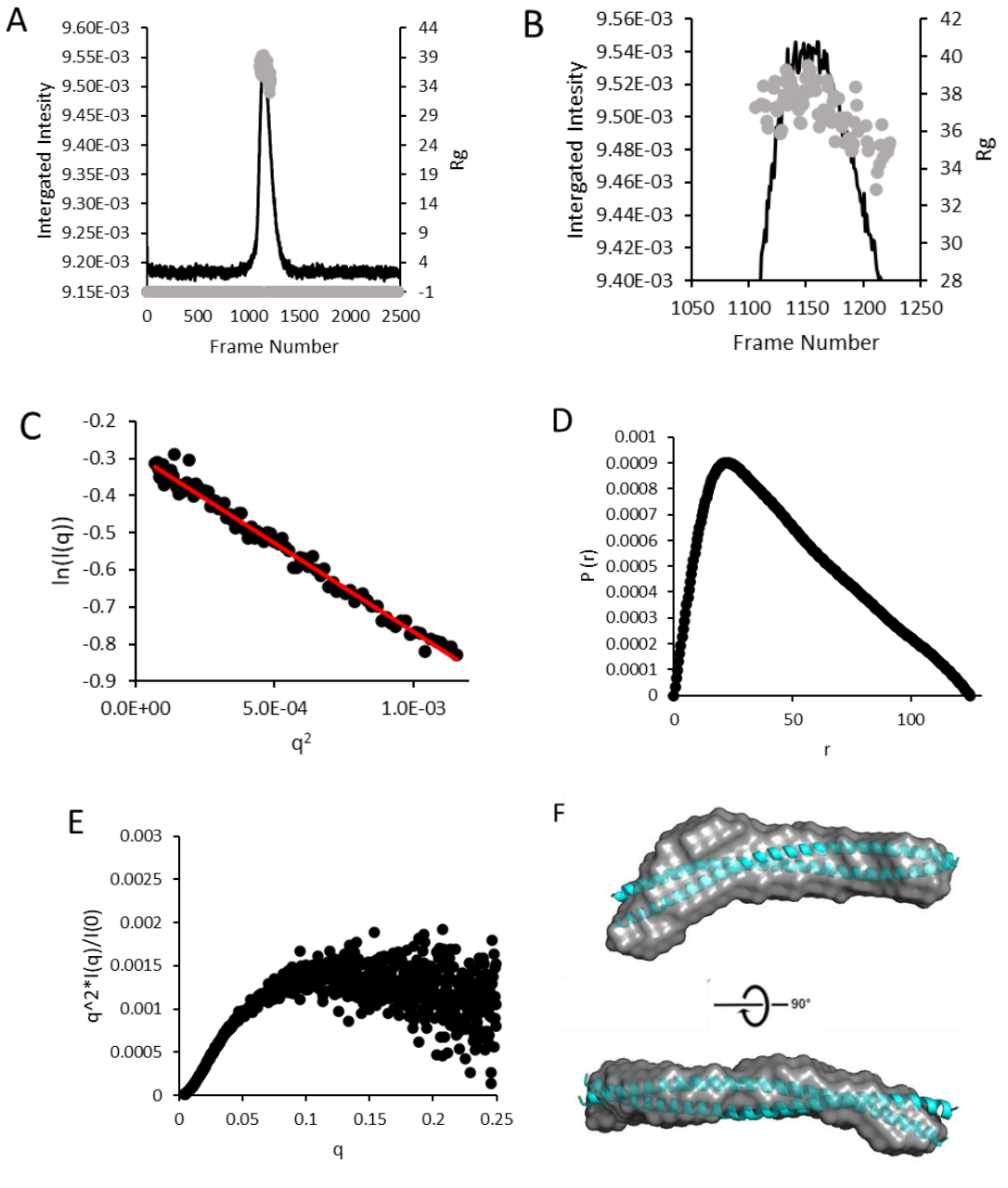

Figure 4.10: SAXS analysis of TAB 2 CCD:His_6-BECN2 CCD after SVD to eliminate unwanted proteins. A) Integrated intensity vs frame number in black and Rg vs frame number in grey. B) Zoomed in of (A) to see Rg values over top of peak. C) Guinier plot. D) Kratky plot. E) P(r) pairwise distribution. (F) SAXS envelopes in gray fitted with the BECN2 CCD homodimer (PBP ID 5K7B), with main chain shown in cyan ribbon.

4.3.8. Crystals From Crystallization Screening and Manual Trays

Robotic screening of the TAB2 CCD:His_6-BECN2 CCD complex with the MCSG1 and MCSG2 sparse matrix screens in 96-well plates incubated at 20 °C, produced potential crystallization hits that polarized light (Table 4.2 and Figure 4.11 A-F).

Table 4.2: Potential crystal hits of His_6-BECN2 CCD:TAB2 CCD complex from MCSG-1 and MCSG-2 crystal screens (Anatrace).

Screen condition	protein: well	Protein concentration	Reservoir solution	Figure #
MCSG1 B7	1:1	4.3 mg/mL	0.17 M Ammonium Acetate, 0.085 M Sodium Citrate, 25.5% (w/v) PEG, 15% (v/v) Glycerol	
MCSG1 H7	3:1	4.3 mg/mL	2.0 M Ammonium Sulfate, 0.1M Bis-Tris pH 5.5	4.11 A
MCSG1 H10	3:1	4.3 mg/mL	0.1 M HEPES pH 7.5, 25% (w/v) PEG 3350	4.11 B
MCSG1 E8	3:1, 1:1, 1:3	9.3 mg/mL, 4.6 mg/mL	0.1 M Tris pH 8.0, 1.8 M Magnesium Sulfate	4.11 C
MCSG1 E9	3:1, 1:1, 1:3	4.3 mg/mL	0.2 M Calcium Chloride, 20% (w/v) PEG 3350	4.11 D
MCSG2 C8	3:1, 1:1, 1:3	4.6 mg/mL	0.1 M Bis-Tris Propane pH 7.0, 1.8 M Magnesium Sulfate	4.11 E
MCSG2 D11	3:1	4.3 mg/mL	0.1 M Tris-HCl pH 8.5, 1.5 M Lithium Sulfate	4.11 F

Hanging-drop vapor diffusion optimization experiments performed using 24-well trays, assessed the impact of the different types and concentrations of salts and precipitants, different buffer pH, and incubation at 20 °C and 4 °C, on crystal quality. However, these optimization experiments produced only spherulites (Figure 4.11 G). These spherulites were used for micro-seeding experiments, with seed stocks added to drops at dilutions between 1:500 to 1:10000. Seeding trays were optimized by changing the concentrations of the magnesium sulfate from 1.2 M to 1.7 M. Only one of the seeded drops showed anything resembling crystals (Figure 4.11 H), and these were not of sufficient quality for X-ray diffraction experiments.

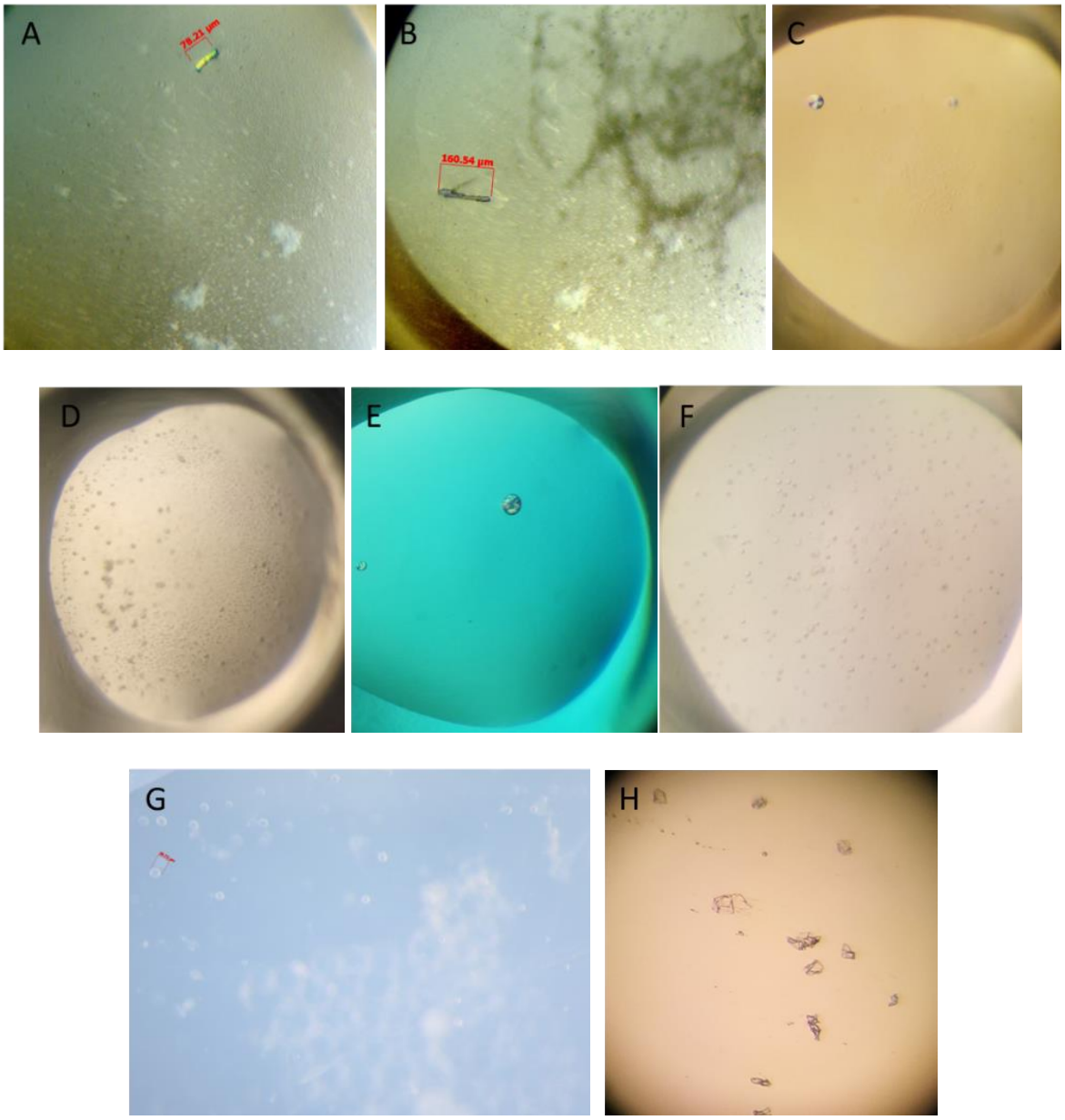

Figure 4.11: Images of potential crystals. A) Potential crystal hit from MCSG-1 H7 at 3:1 in well solution of 2.0 M Ammonium Sulfate, 0.1M Bis-Tris pH 5.5. B) Potential crystal hit from MCSG-1 well H10 at 3:1 in well solution of 0.1 M HEPES pH 7.5, 25% (w/v) PEG 3350. C) Potential crystal hit from MCSG-1 well E8 at 1:3 in well solution of 0.1 M Tris pH 8.0, 1.8 M Magnesium Sulfate. D) Potential crystal hit from MCSG-1 well E9 at 3:1 in well solution of 0.2 M Calcium Chloride, 20% (w/v) PEG 3350. E) Potential crystal hit from MCSG-2 well C8 at 1:1 in well solution of 0.1 M Bis-Tris Propane pH 7.0, 1.8 M Magnesium Sulfate. F) Potential crystal hit from MCSG-2 well D11 at 3:1 in well solution of 0.1 M Tris-HCl pH 8.5, 1.5 M Lithium Sulfate. G) Potential crystal hit from manual tray in well solution of 0.1 M Tris pH 8, 2.0 M $MgSO_4$. H) Potential crystals after micro-seeding with a 1:500 dilution of seed stock into a drop of 1:1 protein:well solution of 0.1 M Tris pH 8, 1.2 M $MgSO_4$.

4.4. Conclusions and Discussion

Our biophysical and structural analyses show, for the first time, that BECN2 interacts directly with TAB2, and the CCD of each protein is necessary and sufficient for interaction. The TAB2 and BECN2 CCD bind with an affinity of 6.53 μM, which is tighter than the Kd of BECN2 CCD homodimerization[20]. Our SEC, SDS-PAGE and Mass Spectrometry data indicate that we have successfully developed protocols to obtain pure and homogenous BECN2 CCD:TAB2 CCD complex. Unfortunately, our attempts to crystallize this complex were unsuccessful and we did not obtain diffraction-quality crystals, preventing us from obtaining atomic level information on this complex.

Our SEC-SAXS analyses indicates that the MBP-TAB2 CCD:Sumo-His_6-BECN2 CCD is a well-folded, elongated complex and the molecular weight calculated from the V_c is ~1.1 times the size of the theoretical molecular weight of the heterodimer complex. The TAB2 CCD:His_6-BECN2 CCD complex is partially folded, with an elongated shape. The molecular weight calculated from V_c is slightly smaller than the theoretical molecular weight expected for the heterodimer complex, indicating that the TAB2 CCD:BECN2 CCD complex most likely forms a heterodimer. Fit of the BECN2 CCD homodimer crystal structure to the experimental SAXS envelope for the TAB2 CCD:His_6-BECN2 CCD complex, indicates that a 2-helix coiled-coil of the correct length fits the envelope, although there might be a difference in the curvature of the TAB2 CCD:His_6-BECN2 CCD heterodimer.

We determined that the BECN2 CCD interacts with the TAB3 CCD, but not as well as with the TAB2 CCD. Our preliminary quantification of the thermodynamics of binding indicated a binding affinity of 26.5 μM, but this experiment was only done once and needs further

optimization. Further, we were unable to get purified complex, and therefore unable to further characterize the interaction as we did with the BECN2 CCD and TAB2 CCD complex.

Based on the preliminary studies presented in this chapter, in the future we could attempt to model the interaction of the BECN2 CCD with the TAB2 CCD and TAB3 CCD using a modeling program like Alphafold-2.0[73]. This would allow us to identify potential residues from each protein that contribute to the interaction interface and assess the importance of these residues by mutating them and assessing the impact on binding. Such a detailed understanding of BECN2 interactions would not only help us better understand the divergent role of the two BECN paralogs in mammals but also better elucidate the crosstalk between autophagy and TAK1-IKK signaling.

CHAPTER 5. BECLIN 2 INTERACTS WITH SYNTAXIN 6 TO FORM AN ANTI-PARALLEL THREE-HELIX BUNDLE, A POSSIBLE T-SNARE INTERMEDIATE COMPLEX

5.1. Introduction

Syntaxin 6 (STX6), a soluble N-ethylmaleimide-sensitive factor attachment protein receptor (SNARE) protein, contains an N-terminal domain followed by a SNARE domain and a single C-terminal helical membrane anchor[74]. SNARE domains associate to form a parallel four-helix bundle that typically contain one Arginine (R)-SNARE associated with the fusing vesicle (thereby also called a v-SNARE) and three Glutamine (Q)-SNAREs associated with the target membranes (thereby also called t-SNAREs), with at least one of the Q-SNAREs tethered to the target membrane[75-77]. Formation of the SNARE bundle brings the vesicle and target membranes together. The SNARE complex is stabilized by 15 or 16 layers of four interacting residues contributed by each of the four helices. The middle layer, termed 'layer 0', is an ionic layer that typically contains an arginine from the R-SNARE and three glutamines from the three Q-SNARES[75, 76]. STX6 is expressed at higher levels in the brain, lungs, and kidneys[78]. STX6 is found in the trans-Golgi network and early endosomes in most cells[79]. Based on sequence analysis of its SNARE domain, STX6 has been classified as a member of the SNAP-25 family and also as a Q-SNARE[80]. STX6 contributes a glutamine to the 'layer 0' of the SNARE complex it forms with syntaxin 13, Vti1a, and VAMP4, which functions in homotypic fusion of early endosomes[74].

Recently, STX6 was shown to interact with BECN2 in ATG9A-bearing vesicles[11, 24]. Degradation of TAK1 and mitogen-activated protein kinase kinase kinase 3 (MEKK3), and the BECN2-mediated degradation of inflammasome sensors is not stopped by knockout of the

canonical autophagy proteins ATG16L, LC3B, and BECN1, but is stopped by knockout of ATG9A and ULK1, indicating that BECN2-mediated degradation of TAK1 and MEKK3 is a result of non-canonical autophagy involving ATG9A-bearing vesicles[11, 24, 25]. Notably, STX6 knockout causes partial blockage of BECN2-mediated degradation of MEKK3. The BECN2 and STX6 domains required for interaction have not been delineated, and the BECN2:STX6 interaction has yet to be biophysically or structurally characterized.

In this study we first verify that the STX6 SNARE domain interacts directly with the BECN2 CCD. We use CD to investigate the structure and stability of each interacting protein individually and in complex. We use ITC and MST to try to determine the affinity with which STX6 SNARE binds to BECN2. We also used SEC-SAXS to try to obtain and compare low-resolution solution structure of the complex with that of the corresponding unbound proteins. We determine the X-ray crystal structure of complex of the two proteins and analyze the structure to determine the oligomeric state of the complex and the packing of interface residues stabilizing the complex. Further we assess the importance of hydrophobic interface residues by mutating these residues and use pull-down assays to determine their impact on the STX6:BECN2 interaction. Structural comparisons with other SNARE complexes help provide mechanistic insights into the assembly of SNARE complexes that are involved in non-canonical autophagy involving ATG9A-bearing vesicles.

5.2. Material and Methods

5.2.1. Creation of Protein Expression Constructs

The STX6 SNARE, comprising residues 170-232, was cloned between *NdeI* and *XhoI* restriction enzyme sites of the pET-28a bacterial expression vector such that the expressed protein includes an N-terminal hexa-histidine (His_6) tag for affinity purification. Site-directed

mutagenesis was used to generate the point mutations of His_6-STX6 SNARE (L173D, V176D, L183D, L208D, L215D, and V218D). STX6 residues 170-232, were cloned between *BamHI* and *XhoI* restriction enzyme sites of the pMBP parallel vector 1 bacterial expression vector such that the expression construct includes an N-terminal MBP tag. Site-directed mutagenesis was used to generate the point mutations of MBP-STX6 SNARE (L173D, V176D, L183D, L208D, L215D, and V218D).

The BECN2 CCD were cloned into the pMBP parallel 1 expression vector between the BamHI and NotI restriction sites and used to produce protein, as previously reported for the determination of the X-ray crystal structure of this domain[20]. Subsequently, based on our initial crystal structure, site-directed mutagenesis was used to generate a shorter BECN2 CCD construct encoding only residues 181-250. We henceforth call this construct BECN2(181-250). Lastly, site-directed mutagenesis was used to generate point mutations in BECN2(181-250): L194D, A197D, L204D, L229D, L236D, and A239D.

5.2.2. Protein Expression and Purification

All proteins were expressed by transforming *E. coli* BL21(DE3)pLysS cells with the appropriate expression plasmid(s). Transformed cells were selected by inclusion of appropriate antibiotics in LB media used for growth: 100 µg/ml ampicillin for *p*MBP parallel 1 derived expression vectors or 25 µg/mL kanamycin for pET-28a derived bacterial expression vectors. Cultures were grown at 37 °C to an OD_{600} ~ 0.7 prior to equilibrating the temperature to 20 °C, after which 0.5 mM IPTG was added to induce protein expression overnight. Bacterial cells were harvested by centrifugation at 4000 x g for 15 minutes at 4 °C, and cell pellets were resuspended in 50 mL of buffer consisting of 25 mM Tris pH 8, 150 mM NaCl, and 2 mM βME prior to cell lysis by sonication. Proteins were purified by various chromatography methods as described

below and protein concentrations quantified using UV/Vis spectroscopy. During each stage of the purification, protein purity was monitored by SDS-PAGE, by loading either 15 µg total protein or a maximum volume of 15 µL into each sample well in the gel. The final step of purification of each protein was SEC using SEC buffer consisting of 25 mM Tris pH 8, 150 mM NaCl, and 2 mM βME. Final protein purity was, estimated to be >95% pure by SDS-PAGE stained with Coomassie Blue.

The MBP-STX6 SNARE fusion protein was purified from the clarified lysate by amylose affinity chromatography on a gravity column hand-packed with10 mL amylose resin (NEB BioLab). After applying sample, the column was washed with 30 column volumes of wash buffer (25 mM Tris pH 8, 150 mM NaCl, 2 mM βME). Protein was eluted from the amylose resin with wash buffer plus 20 mM maltose. Pooled fractions were concentrated to 21 mg/mL before SEC. Final purification was achieved by injecting 0.5 mL over a Superdex 200 increase 10/300 SEC column (GE Healthcare) equilibrated with SEC buffer (25 mM Tris pH 8, 150 mM NaCl, 2 mM βME) and eluted using an isocratic gradient. Absorbance at 280 nm was monitored and 1 mL fractions were collected during the course of the elution. Purified protein was concentrated to 19.5 mg/mL using a 30 kD Amicon Ultra-4 centrifugal concentrator (MilliporeSigma), flash-frozen in 25 µL aliquots dropwise into liquid N_2 and stored at -80 °C. All MBP-STX6 SNARE point mutations were purified in a similar manner.

The His_6-STX6 SNARE was purified from the clarified lysate by Ni^{++}-NTA affinity chromatography using 5 mL Ni^{++}-NTA resin (Thermo Fisher Scientific) in a gravity column. The column was washed with 30 column volumes of wash buffer (25 mM Tris pH 8, 150 mM NaCl, 2 mM βME, 25 mM Imidazole). Protein was eluted from the Ni^{++}-NTA resin with wash buffer plus 250 mM Imidazole. Pooled fractions were concentrated to 8.9 mg/mL before SEC. Final

purification was achieved by injecting 0.5 mL over a SEC using Superdex 75 increase 10/300 column (GE Healthcare). Purified protein was concentrated to 9.1 mg/mL using a 4 kD Amicon Ultra-4 centrifugal concentrator (MilliporeSigma), flash-frozen in 25 µL aliquots dropwise into liquid N_2 and stored at -80 °C.

The MBP-BECN2 CCD fusion protein was purified from the clarified lysate by amylose affinity chromatography using 5 mL amylose resin (NEB BioLab) in a gravity column. The column was washed with 30 column volumes of wash buffer (25 mM Tris pH 8, 150 mM NaCl, 2 mM βME). Protein was eluted from the amylose resin with wash buffer with the addition of 20 mM maltose. Pooled fractions were concentrated to 10.3 mg/mL before SEC. Final purification was achieved by injecting 0.5 mL over a Superdex 200 increase 10/300 SEC column (GE Healthcare). Absorbance at 280 nm was monitored and 1 mL fractions were collected during the course of the elution. Purified protein was concentrated to 8.9 mg/mL using a 30 kD Amicon Ultra-4 centrifugal concentrator (MilliporeSigma), flash-frozen in 25 µL aliquots dropwise into liquid N_2 and stored at -80 °C.

The MBP-BECN2(181-250) and all MBP-BECN2(181-250) point mutations were purified using protocols identical to the MBP-BECN2 CCD.

The BECN2 CCD was purified in the same manner as the MBP-BECN2 CCD up to the amylose wash step. The protein was then subjected to on-column cleavage by the addition of GST-TEV protease and incubating at 4 °C overnight. The relased protein was washed off the column using wash buffer and further purified by ion exchange chromatography on a 5/50 GL MonoQ column (GE Healthcare) (MonoQ Buffer A: 25 mM Tris pH 8, 2 mM βME; MonoQ Buffer B: 25 mM Tris pH 8, 1 M NaCl, 2 mM βME). The protein was loaded and washed with 5% MonoQ Buffer B and eluted with a gradient of 5 – 50% MonoQ buffer B over 200 mL. the

BECN2 CCD eluted at approximately 15% MonoQ Buffer B. The protein was further purified by SEC using Superdex 200 increase 10/300 column (GE Healthcare) and eluted using an isocratic gradient. Absorbance at 280 nm was monitored and 1 mL fractions were collected during the course of the elution. Purified protein was concentrated to 6.1 mg/mL using a 3 kD Amicon Ultra-4 centrifugal concentrator (MilliporeSigma), flash-frozen in 25 µL aliquots dropwise into liquid N_2 and stored at -80 °C. BECN2(181-250) was purified in an identical manner to the BECN2 CCD.

5.2.3. Affinity Pulldown Assays and Purification of BECN2:STX6 SNARE Complexes

Both, the MBP-BECN2 CCD:His_6-STX6 SNARE complex and the MBP-BECN2(181-250):His_6-STX6 SNARE complex were each co-expressed as described for the individual proteins, except that BL21(DE3)pLysS cells were transformed with both expression plasmids. Plasmid containing transformants were selected by inclusion of 100 µg/ml ampicillin for and 25 µg/mL kanamycin in the LB media. Clarified cell lysate was prepared as described above. The MBP-BECN2(181-250):His_6-STX6 SNARE complex was purified from clarified crude cell lysate by Ni^{++}-NTA affinity chromatography with wash buffer consisting of 25 mM Tris pH 8, 150 mM NaCl, 2 mM βME, and 25 mM imidazole, and then eluted from the resin with wash buffer containing 250 mM imidazole. The complex was then passed over amylose affinity resin with wash buffer consisting of 25 mM Tris pH 8, 150 mM NaCl, and 2 mM βME, and then eluted with wash buffer containing 20 mM maltose. Protein interaction was qualitatively assessed by evaluating co-elution of proteins using Coomassie blue stained SDS-PAGE. Similar pull-down assays were performed to assess binding of each BECN2(181-250) mutant; L194D, A197D, L204D, L229D, L236D, and A239D; to wild-type (WT) His_6-STX6 SNARE, as well as

of each His_6-STX6 SNARE mutant; L173D, V176D, L183D, L208D, L215D, and V218D; to WT BECN2(181-250).

For structural and biophysical experiments, the BECN2 CCD:His_6-STX6 SNARE complex was co-purified in a manner similar to the pull-down assays, up to binding and washing on the amylose affinity resin. However, the complex was not eluted off the column, rather the MBP tag was cleaved by on-column TEV protease cleavage, as described for the purification of BECN2(181-250) alone. Subsequently, the BECN2 CCD:His_6-STX6 SNARE complex was further purified using Ni^{++}-NTA affinity chromatography, followed by glutathione Sepharose affinity chromatography to remove degraded protein and GST-TEV protease. Finally, the cleaved protein was purified by SEC using a Superdex 200 10/300 increase (GE Healthcare Life Sciences) The BECN2(181-250):His_6-STX6 SNARE complex was expressed and purified in a manner identical to the BECN2 CCD:His_6-STX6 SNARE complex.

5.2.4. CD and Thermal Denaturation

CD data were recorded from BECN2 CCD, BECN2(181-250), the BECN2 CCD:His_6-STX6 SNARE complex, and the BECN2(181-250):His_6-STX6 SNARE complex at a concentration of 10 µM and from His_6-STX6 SNARE at a concentration of 30 µM in a quartz cell with a 0.1 cm path length using a Jasco J-715 CD spectrometer. Each sample was dialyzed against CD buffer comprised of 10 mM potassium phosphate, pH 7.5, and 100 mM ammonium sulfate. Full-length scanning spectra were collected between 190 and 250 nm at 4 °C. Secondary structure content of each sample was estimated using CONTIN and CDSSTR analysis within the CDPro program package[81]. Thermal denaturation curves were recorded by measuring CD Signal at 222 nm at 1 °C intervals with a ramp of 1 °C/min from 4 °C to 90 °C for heating measurements (or 90 °C to 4 °C for cooling measurements). Data were analyzed using OriginPro

8 (OriginLab). The mean residue molar ellipticity was plotted against temperature and the T_m obtained by fitting data to the Boltzman algorithm included in OriginPro 8. The values reported in Table 2 are the T_m calculated separately from the heating and cooling curves.

5.2.5. CD with 2,2,2-Trifluoroethanol (TFE)

Experiments were performed as described above for both CD and thermal denaturation. The protein was dialyzed against a buffer comprising 10 mM potassium phosphate pH 7.5, and 100 mM ammonium sulfate, and different amounts of TFE (0%, 10%, 25%, and 40%). Data were analyzed as described above.

5.2.6. ITC

The thermodynamics of the binding of BECN2 to STX6 SNARE was assessed by ITC, using a Low Volume Nano ITC (TA Instruments). All ITC experiments were performed at 20 °C with 20 injections of 2.5 µL each, with a stirring rate of 200 RPMs.

Prior to ITC, the His_6-STX6 SNARE or MBP-STX6 SNARE and MBP-BECN2 CCD or MBP-BECN2(181-250) samples were loaded into separate dialysis cassettes and co-dialyzed against the ITC buffer consisting of 25 mM Tris pH 8, 150 mM NaCl, and 2 mM βME. MBP-BECN2 CCD at a concentration between150 to 437 µM was loaded into the syringe and titrated into the cell containing 30 to 62 µM of the His_6-STX6 SNARE. The reverse experiment was also performed, wherein 139 to 614 µM of MBP-STX6 SNARE was in the syringe and titrated into the cell containing 14 to 58 µM of MBP-BECN2 CCD or 50 to 76 µM of MBP-BECN2(181-250). Blank profiles were obtained by titrating buffer into buffer and subtracted from the experimental binding profiles.

For dissociation experiments 50 to 100 µM of His_6-STX6 SNARE, 286 µM of MBP-STX6 SNARE, 516 µM of MBP-BECN2(181-250), and 11 to 44 µM of MBP-BECN2

CCD:His_6-STX6 SNARE protein samples were dialyzed against 25 mM Tris pH 8, 150 mM NaCl, 2 mM βME. The proteins were loaded into the syringe and titrated into the cell containing buffer.

All data were analyzed using the NanoAnalyze Software (TA Instruments) using independent binding models and with a blank constant model to correct to baseline.

5.2.7. MST

Experiments were performed using a Monolith Pico MST (Nanotemper). All experiments were performed at 20 °C in standard capillaries. The MBP-BECN2(181-250) was labeled with Red NHS 2nd generation label following Nanotempers protocol, with a degree of labeling of 1.001. Initial experiments were performed using a buffer consisting of 25 mM HEPES pH 7.5, 150 mM NaCl, 0.05% (v/v) TWEEN 20. The concentration used for Red NHS labeled MBP-BECN2(181-250) was 20 nM and the concentration of MBP-STX6 SNARE used was 0.002869µM to 94µM . From these initial experiments, the concentration of MBP-STX6 SNARE was adjusted to test lower concentrations (0.00119µM to 39µM and 0.0005951µM to 19.5µM) and concentrations (0.002518µM to 82.5µM). To help with aggregation, the buffer was adjusted, to consist of 25 mM HEPES pH 7.5, 150 mM NaCl, 0.1% (v/v) TWEEN 20. The interaction was also tested in a buffer consisting of 25 mM HEPES pH 7.5, 150 mM NaCl, 0.1% (v/v) TWEEN 20, and 10% (v/v) TFE.

5.2.8. SEC-SAXS

SEC-SAXS data were recorded at beamline 18-ID Bio-CAT at APS, ANL, Argonne, IL with in-line SEC to separate the sample from aggregates, thus ensuring optimal sample.

Purified proteins in 25 mM Tris pH 8.0, 150 mM NaCl, and 2 mM βME were loaded at 5.2 to 17.7 mg/mL onto a column at a flow rate of 0.5 ml min^{-1} using an Infinity II 1260 HPLC

(Agilent). The SEC eluate was passed through a UV monitor and then into the SAXS flow cell, a 1.0 mm ID quartz capillary with 50 μm walls using a co-flow sample geometry to prevent radiation damage[67].

Each sample was exposed to an X-ray beam of size 150 (h) x 25 (v) μm^2, wavelength 1.03 Å (12 keV energy) for 1 s/frame, with a periodicity of 1 s/frame, and the SAXS data were recorded on a Pilatus3 X 1M detector (Dectris) at a sample to detector distance of 3.6 m. The range of momentum transfer (q) accessed was $0.005\ Å^{-1} < q < 0.35\ Å^{-1}$. Commercially available glassy carbon plates were used as absolute intensity calibration standards for SAXS data collection (NIST SRM 3600). X-ray radiation damage was monitored by automated frame-by-frame comparison of relevant regions using CORMAP [82], which is implemented in BioXTAS RAW (version 1.6.4). Scattering data were normalized to the transmitted X-ray beam intensity and scattering from buffer subtracted using the BioXTAS RAW software (version 1.6.4)[69] prior to further analysis. Guinier fits were used to calculate the radius of gyration (R_g) and scattering at zero angle I(0), and dimensionless Kratky plots[83] were used to evaluate disorder within the samples. GNOM [84] was used to calculate the indirect Fourier transform to obtain the pairwise-distance distribution function, P(r)[85], which was used to estimate the maximum particle size (D_{max}), R_g, and I(0). The molecular mass was calculated using the Volume of correlation (V_c) method[86] implemented in RAW.

5.2.9. Crystallization

The BECN2 CCD:His_6-STX6 SNARE and BECN2(181-250):His_6-STX6 SNARE complexes were screened for initial crystallization conditions at 20 °C using a Gryphon crystal screen dispensing robot (Art Robbins Instruments). Two sparse matrix screens, MCSG 1 and MCSG 2 (Anatrace, Maumee, OH, USA), each of which includes 96 different reservoir solution

compositions were tested, using a 3:1, 1:1, 1:3 v/v ratio of protein:reservoir solution (9.3 mg/mL complex in 25 mM Tris pH 8, 150 mM NaCl, 2 mM βME). Thus, a total of 576 different conditions were screened for crystallization of these complexes.

Crystals of both BECN2 CCD:His_6-STX6 SNARE and BECN2(181-250):His_6-STX6 SNARE complexes were optimized at 20 °C by hanging-drop vapor diffusion. The BECN2 CCD:His_6-STX6 SNARE was crystallized at a 3:1 mixture of protein stock (9.3 mg/mL protein complex in 25 mM Tris pH 8, 150 mM NaCl, and 2 mM βME) and reservoir solution comprising of 0.1 M Bis-Tris Propane pH 7, and 2.9 M NaCl. The BECN2(181-250):His_6-STX6 SNARE was crystallized from a 3:1 mixture of protein stock (9.3 mg/mL protein complex in 25 mM Tris pH 8, 150 mM NaCl, and 2 mM βME) and reservoir solution comprising of 0.1 M Tris pH 7.5 and 2.8 M NaCl. All crystals were harvested and cryo-protected in Mitegen's LV CryoOil and then immediately cryo-cooled in liquid N_2.

5.2.10. X-ray Data Collection, Structure Solution, and Refinement

X-ray diffraction data from crystals of the BECN2 CCD:His_6-STX6 SNARE complex were collected at beamline 24-ID NE-CAT at the Advanced Photon Source (APS), Argonne National Laboratory (ANL), Argonne, IL. Data were recorded at 100 K, in a 360° helical scan from a single BECN2 CCD:His_6-STX6 SNARE crystal, at 1-second exposure per 0.2° crystal rotation per image, at a crystal-to-detector distance of 351.682 mm. The BECN2 CCD:His_6-STX6 SNARE diffraction data were processed using the RAPD automated processing web server (https://rapd.nec.aps.anl.gov/rapd). The structure of the BECN2 CCD:His_6-STX6 SNARE complex was solved by molecular replacement using structures of the BECN2 CCD (PDB ID: 5K7B) and STX6 SNARE (PDB ID: 2NPS) as search models in Phaser-MR in PHENIX[87]. All refinement was performed using PHENIX[87] and the CCP4 software suite[45].

X-ray diffraction data from crystals of the BECN2(181-250):His_6-STX6 SNARE complex were collected at beamline 23ID-B GMCA at the APS, ANL, Argonne, IL. Data were recorded at 100 K in a 180° sweep from a single BECN2(181-250):His_6-STX6 SNARE crystal, at 0.2-second exposure per 0.2° crystal rotation per image at a crystal-to-detector distance of 300 mm. The BECN2(181-250):His_6-STX6 SNARE diffraction data were processed using the Autoproc processing suite (https://www.globalphasing.com/autoproc/). The structure of BECN2(181-250):His_6-STX6 SNARE structure was solved by molecular replacement using the BECN2 CCD:His_6-STX6 SNARE structure as the search model using Phaser-MR in PHENIX[87]. All refinement was performed using PHENIX[87] and CCP4 software suite[45].

Crystallographic data collection and refinement statistics are summarized in Table 3. All molecular figures were prepared using the PyMOL Molecular Graphics System[88]. The buried surface area was analyzed using PISA[89]. The final refined structures of the BECN2 CCD:His_6-STX6 SNARE and BECN2(181-250):His_6-STX6 SNARE are deposited in the PDB.

5.3. Results

5.3.1. Purification of STX6 SNARE Constructs

His_6-STX6 SNARE was purified by Ni^{++}-NTA affinity chromatography followed by SEC. The SEC elution profile contains three peaks (Figure 5.1). SDS-PAGE shows that the first two peaks contain contaminants while His_6-STX6 SNARE elutes in the third peak.

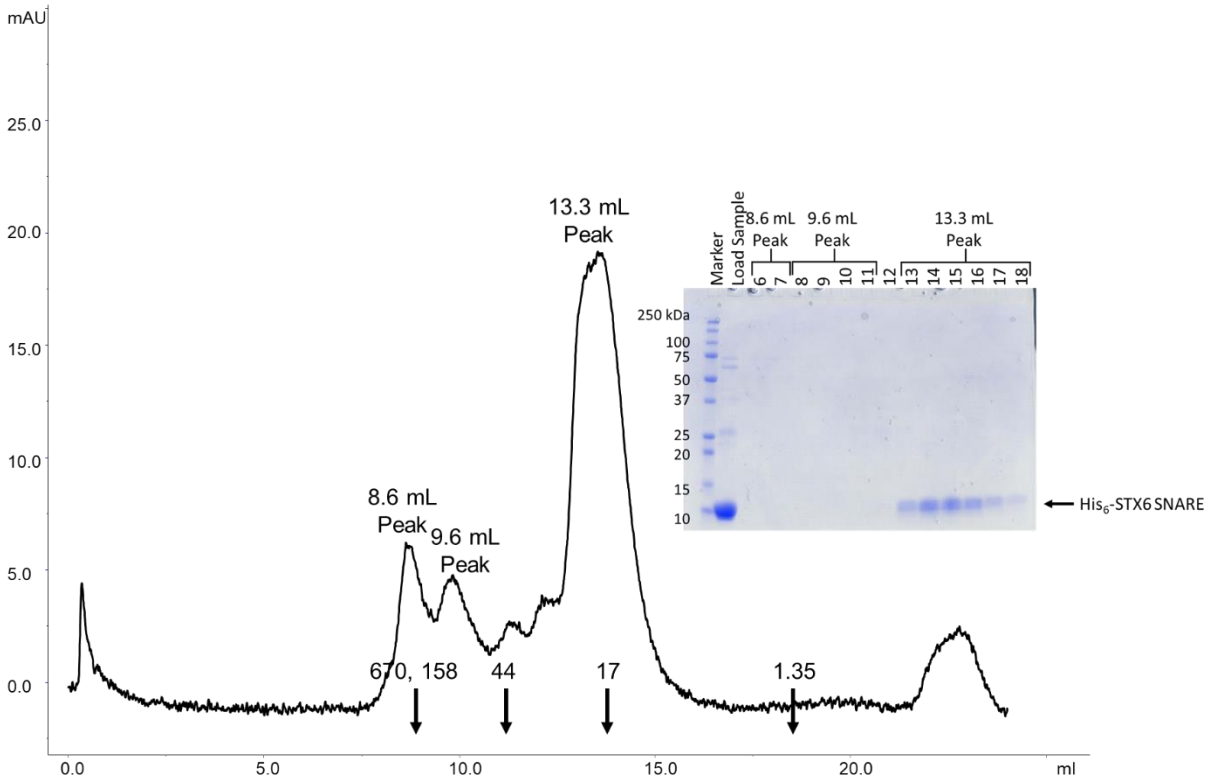

Figure 5.1: Size exclusion chromatogram and Coomassie-stained SDS-PAGE gel of His_6-STX6 SNARE. The elution positions of SEC Superdex 75 increase 10/300 standards are indicated by arrows and corresponding molecular weight.

The molecular weight of the His_6-STX6 SNARE calculated based on the elution volume of 13.3 mL from SEC is 16.8 kD, which is ~1.8 times larger than the theoretical molecular weight of 9.5 kD for the His_6-STX6 SNARE monomer calculated from the amino acid sequence. This suggests that His_6-STX6 SNARE is either a homodimer or an elongated protein. The final yield of the purified His_6-STX6 SNARE obtained from one liter of bacterial culture was 24.3 mg. 95% pure, homogenous, His_6-STX6 SNARE was obtained after SEC, with a yield of 23.4 mg/ liter of culture. However, the His_6-STX6 SNARE was not stable by itself and tended to precipitate.

MBP-STX6 SNARE fusion protein was purified by amylose affinity chromatography followed by SEC. The SEC elution profile contains two overlapping peaks (Figure 5.2).

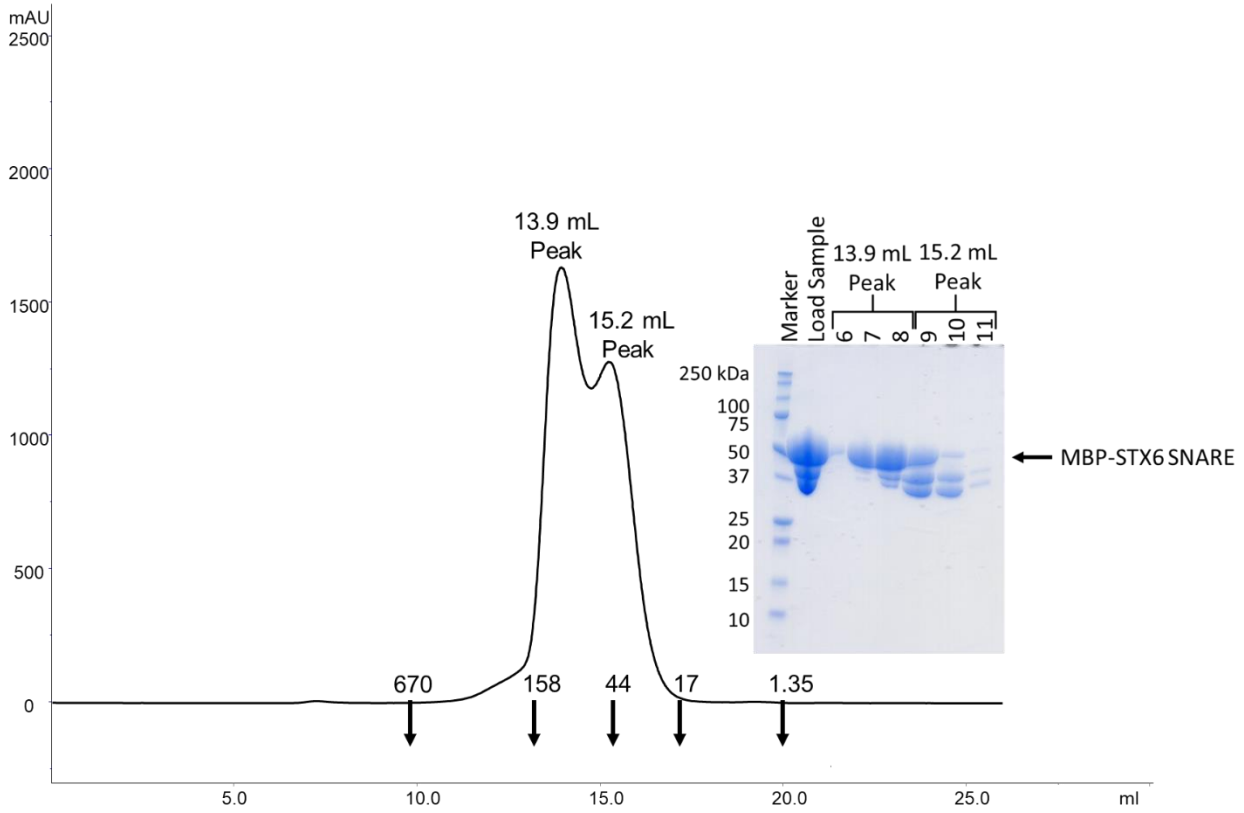

Figure 5.2: Size exclusion chromatogram and Coomassie-stained SDS-PAGE gel of MBP-STX6 SNARE. The elution positions of SEC Superdex 200 increase 10/300 standards are indicated by arrows and corresponding molecular weight.

SDS-PAGE shows that MBP-STX6 SNARE elutes within the first peak, while the second peak includes MBP-STX6 SNARE and lower molecular mass contaminants. The molecular weight of the MBP-STX6 SNARE calculated based on the elution volume of 13.9 mL from SEC is 77.5 kD which is ~1.5 times larger than the theoretical molecular weight of 52 kD for the MBP-STX6 SNARE monomer calculated from the amino acid sequence. This suggests that MBP-STX6 SNARE is an elongated protein or less likely a homodimer. The final yield of the purified MBP-STX6 SNARE obtained from one liter of bacterial culture was 5.2 mg.

5.3.2. Purification of BECN2 CCD Constructs

MBP-BECN2 CCD fusion protein was purified by amylose affinity chromatography followed by SEC. The SEC elution profile contains two main peaks (Figure 5.3).

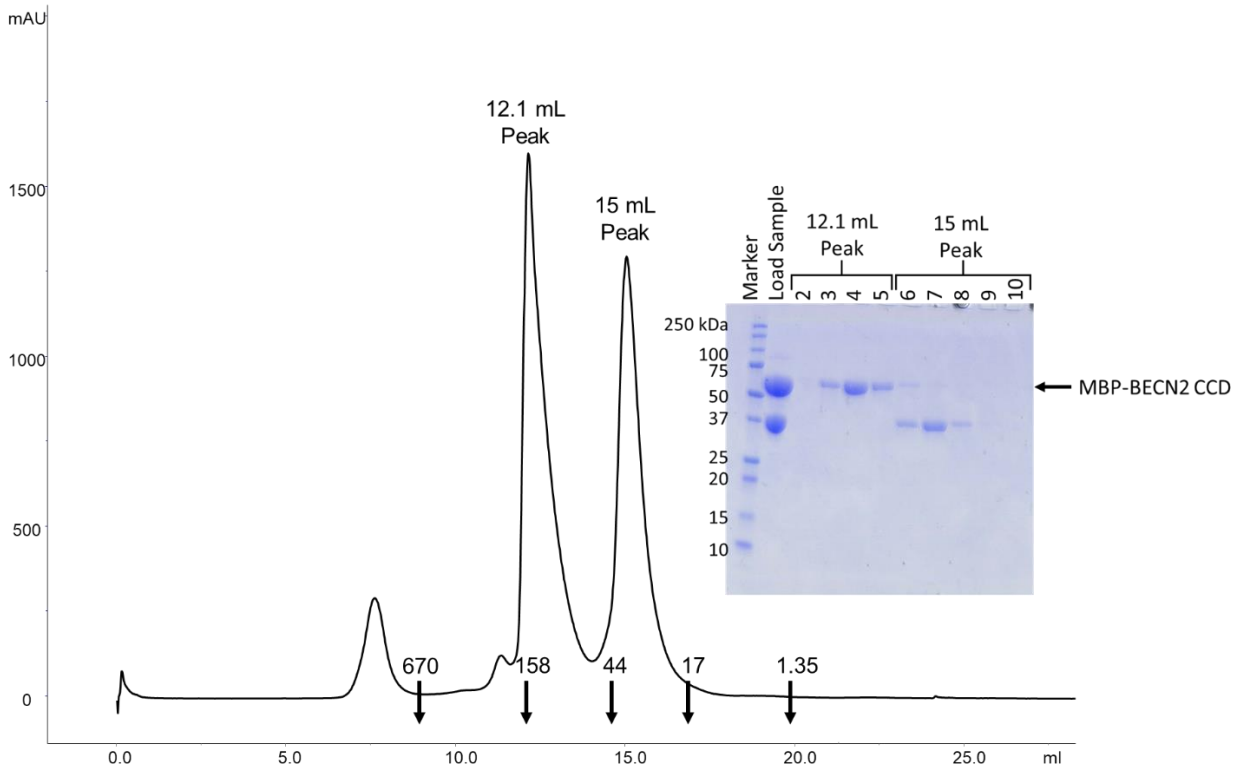

Figure 5.3: Size exclusion chromatogram and Coomassie-stained SDS-PAGE gel of MBP-BECN2 CCD. The elution positions of SEC Superdex 200 increase 10/300 standards are indicated by arrows and corresponding molecular weight.

SDS-PAGE shows that the first peak contains MBP-BECN2 CCD, and the second peak contains lower molecular weight contaminants. The molecular weight of the MBP-BECN2 CCD, calculated based on the elution volume from SEC is 138.3 kD, which is ~1.3 times larger than the theoretical molecular weight of 104 kD for a MBP-BECN2 CCD homodimer calculated from the amino acid sequence. This suggests that MBP-BECN2 CCD is likely an elongated homodimer. The final yield of the purified MBP-BECN2 CCD was 6.7 mg from one liter of bacterial culture.

5.3.3. Purification of BECN2 CCD:His_6-STX6 SNARE Complexes

MBP-BECN2 CCD:His_6-STX6 SNARE fusion protein was purified by Ni^{++}-NTA affinity chromatography and amylose affinity chromatography followed by SEC. The SEC elution profile contains one peak with a trailing -edge shoulder (Figure 5.4). SDS-PAGE shows

that MBP-BECN2 CCD:His_6-STX6 SNARE elutes in the main peak, while the shoulder contains excess MBP-BECN2 CCD and an unknown contaminant.

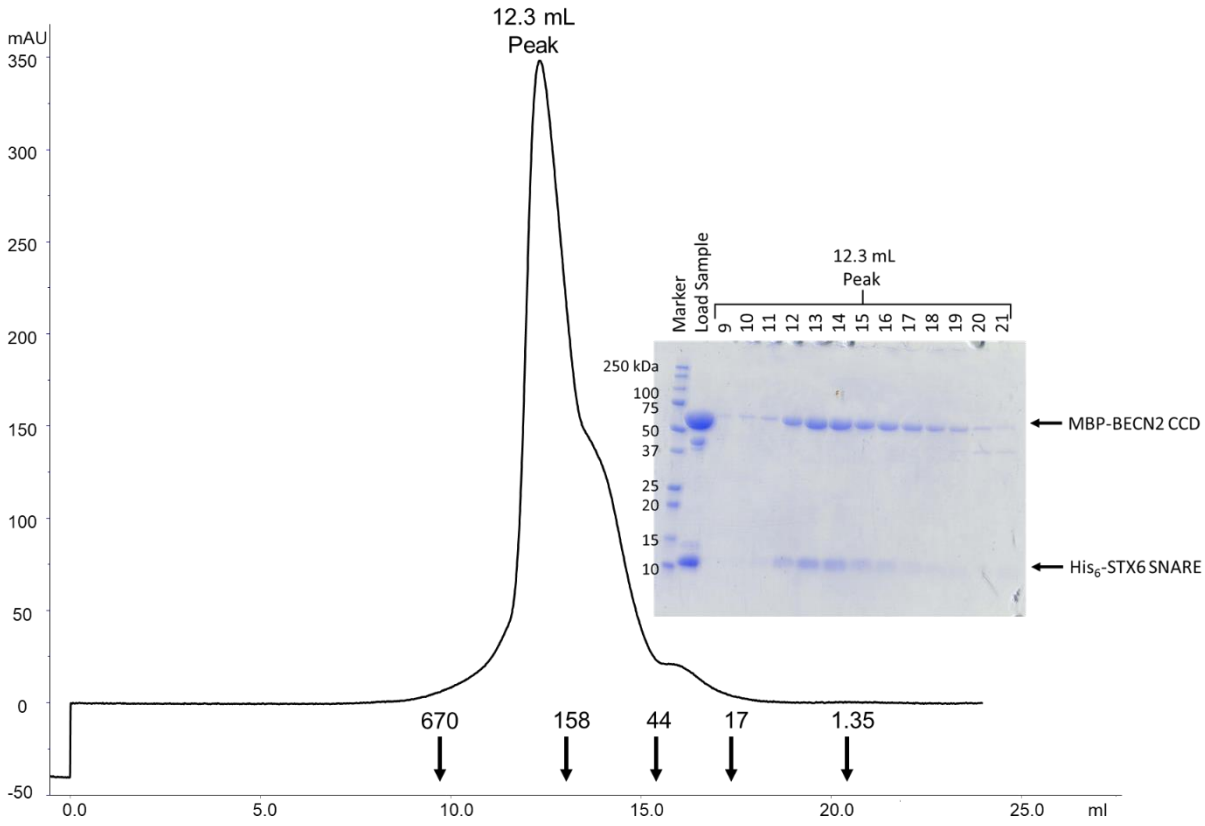

Figure 5.4: Size exclusion chromatogram and Coomassie-stained SDS-PAGE gel of MBP-BECN2 CCD:His_6-STX6 SNARE. The elution positions of SEC Superdex 200 increase 10/300 standards are indicated by arrows and corresponding molecular weight.

The molecular weight of the MBP-BECN2 CCD:His_6-STX6 SNARE, calculated based on the elution volume of 12.3 mL from SEC is 124.4 kD, which is ~2.0 times larger than the theoretical molecular weight of 61.5 kD for the MBP-BECN2 CCD:His_6-STX6 SNARE heterodimer calculated from the amino acid sequence. This suggests that MBP-BECN2 CCD:His_6-STX6 SNARE is an elongated heterodimer or a higher order oligomeric complex. The final yield of the purified MBP-BECN2 CCD:His_6-STX6 SNARE obtained from one liter of bacterial culture was 2.5 mg.

5.3.4. STX6 SNARE Interacts with BECN2 but Not with BECN1

Affinity pull-downs were initially performed by mixing the individually purified MBP-BECN2 CCD and His_6-STX6 SNARE and allowing them to incubate for 1 hour. Despite some evidence of interaction, the complex tended to precipitate during the incubation, likely because the His_6-STX6 SNARE is unstable. Therefore, we attempted to co-express and co-purify the two proteins. This resulted in a much more stable complex that we successfully used for affinity pull-down assays that unambiguously showed interaction (Figure 5.5). As MBP-BECN2 CCD expresses better relative to His_6-STX6 SNARE, we first performed Ni^{++}-NTA affinity purification to eliminate excess MBP-BECN2 CCD, followed by amylose affinity pull-downs to purify the complex. Notably, equivalent experiments (Figure 5.6) using the BECN1 CCD, indicate that the BECN1 CCD does not interact with the STX6 SNARE.

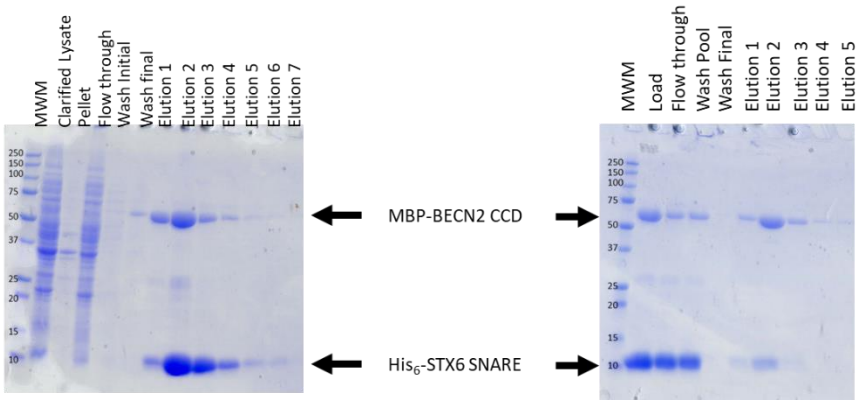

Figure 5.5: SDS-PAGE of affinity pull-downs for MBP-BECN2 CCD:His_6-STX6 SNARE left Ni^{++}-NTA, right Amylose.

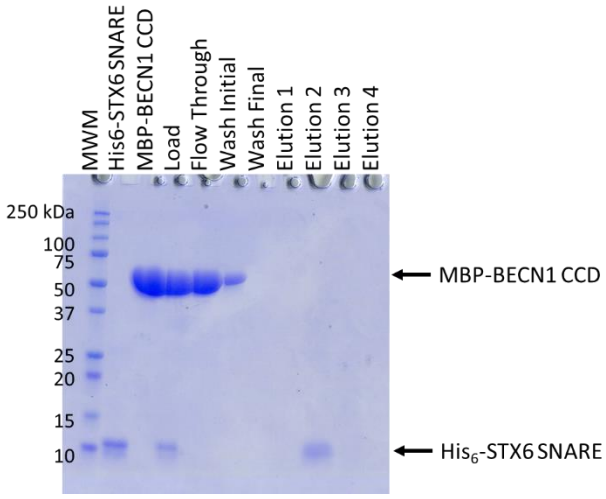

Figure 5.6: SDS-PAGE of affinity pull-downs for MBP-BECN1 CCD and His6-STX6 SNARE.

5.3.5. Purification of BECN2 CCD:His_6-STX6 SNARE Complex

For biophysical and structural experiments, the BECN2 CCD:His_6-STX6 SNARE complex was co-expressed and co-purified as described above, except that the N-terminal MBP tag on the BECN2 CCD was cleaved off on the amylose resin. The SEC profile of BECN2 CCD:His_6-STX6 SNARE complex contains a single peak, and SDS-PAGE indicates that the peak contains both BECN2 CCD and His_6-STX6 SNARE (Figure 5.7). The yield of the complex was 0.5 mg/ liter of culture.

BECN2 CCD:His_6-STX6 SNARE fusion protein was purified by Ni^{++}-NTA affinity, amylose affinity chromatography, and SEC. The SEC elution profile contains two peaks (Figure 5.7). SDS-PAGE indicates the first peak contains the BECN2 CCD:His_6-STX6 SNARE complex and the second peak contains excess, uncomplexed His_6-STX6 SNARE.

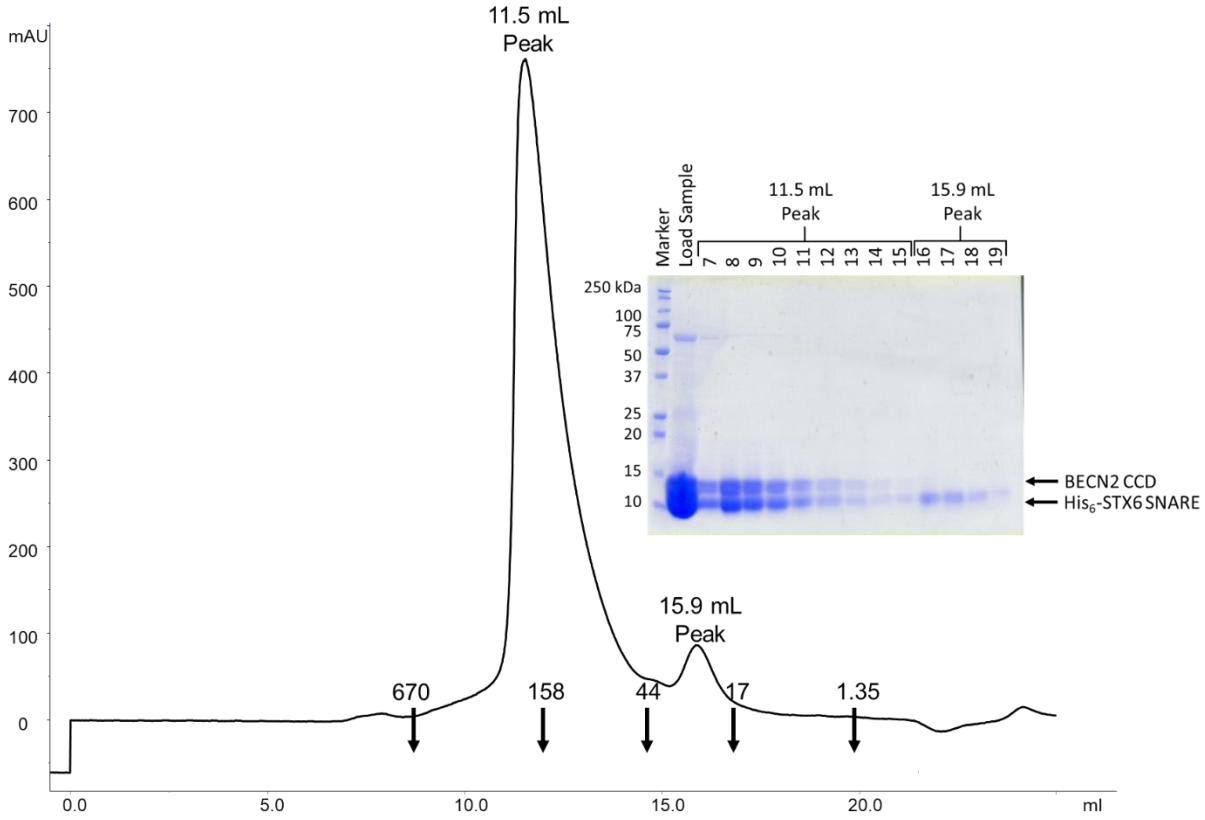

Figure 5.7: Size exclusion chromatogram and Coomassie-stained SDS-PAGE gel of BECN2 CCD:His6-STX6 SNARE. The elution positions of SEC Superdex 200 increase 10/300 standards are indicated by arrows and corresponding molecular weight.

The molecular weight of the BECN2 CCD:His_6-STX6 SNARE calculated based on the elution volume of 12 mL from SEC is 193.1 kD which is ~9.4 times larger than the theoretical molecular weight of 20.5 kD for the BECN2 CCD:His_6-STX6 SNARE heterodimer calculated from the amino acid sequence. This suggests that BECN2 CCD:His_6-STX6 SNARE is an elongated heterodimer or a significantly higher order complex. The final yield of the purified BECN2 CCD:His_6-STX6 SNARE obtained from one liter of bacterial culture was 0.5 mg.

5.3.6. The Disordered STX6 SNARE is Stabilized in a Helical Complex with the BECN2 CCD

We used CD to estimate and compare the secondary structure of the STX6 SNARE, the BECN2 CCD and the BECN2 CCD:STX6 SNARE complex in solution. CD spectra of α-helical

proteins have two minima at wavelengths 208 and 222 nm, while disordered proteins have a negative peak at 195 nm and little ellipticity above 210 nm. Analysis of the CD spectrum of the STX6 SNARE alone indicates the protein is largely disordered with no helical content, as the ~3 residues estimated to be in helical conformation are insufficient to form a single stable helical turn (Figure 5.8 and Table 5.1). In contrast, analysis of the BECN2 CCD CD spectrum indicates that ~55 residues are estimated to be in a helical conformation (Figure 5.8 and Table 5.1). This is consistent with previously reported CD analyses[20]. However, this is significantly lower than the 172 residues observed in helical conformation in the BECN2 homodimer crystal structure[20]. Presumably, the low concentrations required for CD prevent, a significant fraction of the BECN2 CCD forming homodimers, which is required for stabilization of helical conformation[20]. Importantly, the CD spectrum of BECN2 CCD:STX6 SNARE complex has a helical profile, with ~99 residues being in helical conformation, which is greater than the sum of the residues in helical conformation for the two individual proteins. (Figure 5.8 and Table 5.1). Thus, it appears that STX6 becomes more helical upon interacting with BECN2 CCD.

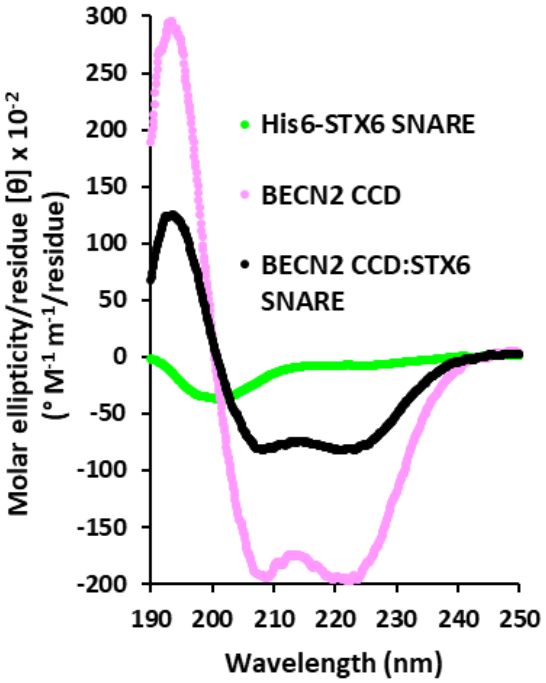

Figure 5.8: CD Spectra at 4 °C of A) His_6-STX6 SNARE (green), BECN2 CCD (violet), BECN2 CCD:His_6-STX6 SNARE (black).

Table 5.1: Summary of Secondary structure content in number of residues and percent for His_6-STX6 SNARE, BECN2 CCD, BECN2 CCD:His_6-STX6 SNARE, BECN2(181-250), BECN2(181-250):His_6-STX6 SNARE.

	Number of Residues (Percent)			
Protein	Helix	Strand	Coil + Turn	Total
His_6-STX6 SNARE	2.8 ± 1.3 (3.2)	30.0 ± 5.0 (35.2)	51.8 ± 5.8 (60.9)	84.6 (99.3)
BECN2 CCD	54.9 ± 2.2 (56)	5.9 ± 1.2 (6)	37.0 ± 3.6 (37.7)	97.8 (99.7)
BECN2 CCD:His_6-STX6 SNARE complex	98.6 ± 0.4 (53.9)	12.1 ± 1.6 (6.6)	72.1 ± 1.3 (39.4)	182.8 (99.9)
BECN2 CCD:2 His_6-STX6 SNARE complex	104.8 ± 4.3 (39.1)	32.2 ± 5.6 (12)	131.5 ± 0.9 (49)	268.5 (100.1)
BECN2(181-250)	37.3 ± 0.1 (49.7)	5.9 ± 1.4 (7.8)	31.9 ± 1.5 (42.5)	75.1 (100)
BECN2(181-250):2 His_6-STX6 SNARE complex	151.5 ± 3.3 (61.8)	20.5 ± 15.8 (8.3)	74.8 ± 10.7 (30.5)	246.8 (100.6)

We also assessed and compared the structural stability of the BECN2 CCD, and the BECN2 CCD:STX6 SNARE complex using thermal denaturation coupled to CD measurements at wavelength 222 nm to quantify melting temperature (T_m). Thermal denaturation is not applicable to the STX6 SNARE, as it is disordered. The BECN2 CCD has a T_m of 14.2 °C and a reverse, cooling T_m of 15.3 °C (Figure 5.9A and Table 5.2). However, as we are unable to record the complete sigmoidal curve for the forward, heating experiment (due to instrument limitations we cannot record a curve lower than 4°C), it is likely that the heating T_m is less accurate and is actually more similar to the cooling T_m. The BECN2 CCD:STX6 SNARE complex has a heating T_m of 28.1 °C and a cooling T_m of 19.5 °C (Figure 5.9B and Table 5.2). The cooling T_m of the complex is likely not very accurate due to precipitation of STX6 SNARE during the heating experiment. These results unambiguously show that the BECN2 CCD:STX6 SNARE complex is more stable than either of the individual proteins by themselves.

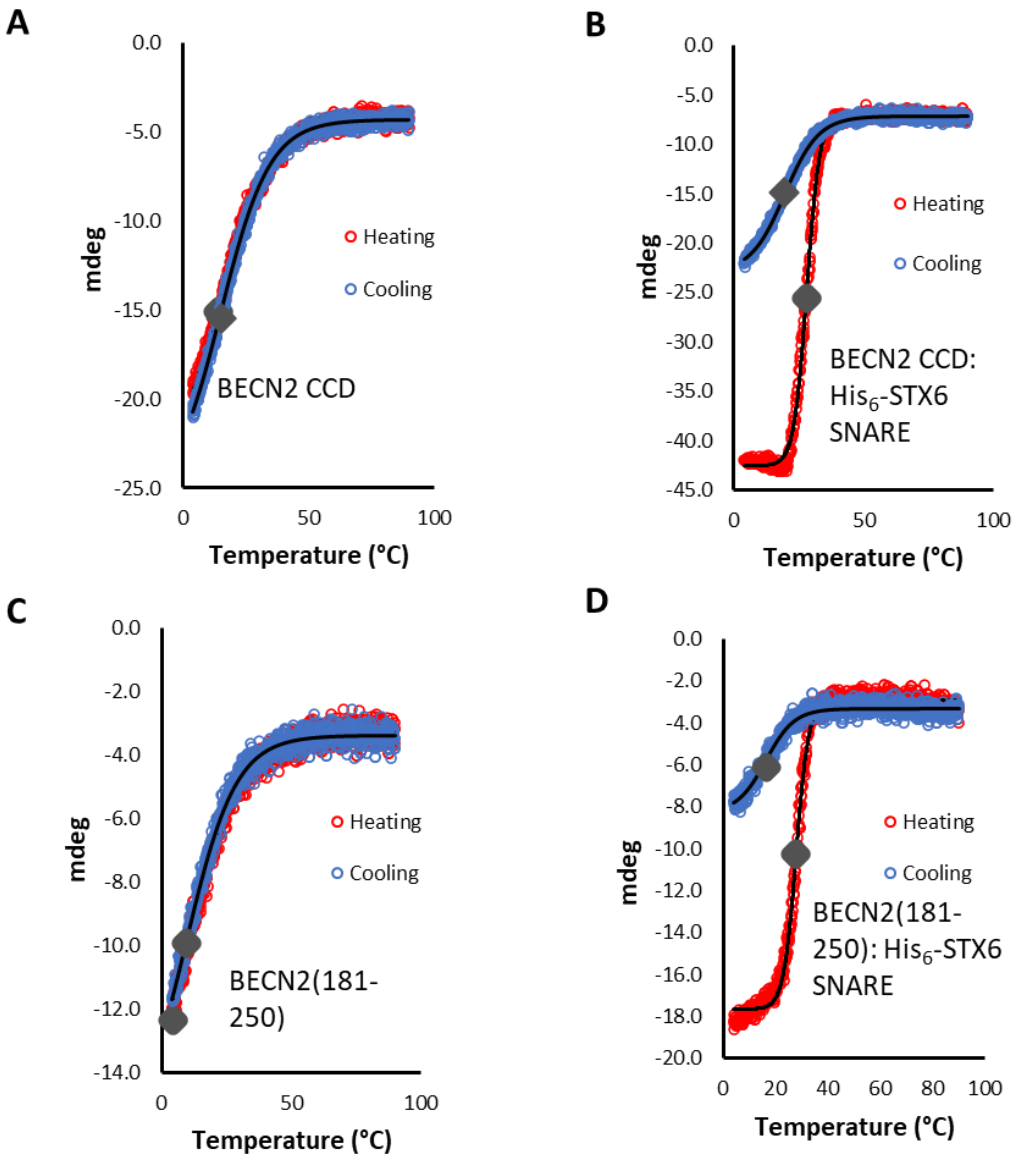

Figure 5.9: Thermal denaturation curves of A) BECN2 CCD. B) BECN2 CCD:His6-STX6 SNARE. C) BECN2(181-250). D) BECN2(181-250):His6-STX6 SNARE. Heating (unfolding) red circles, cooling (refolding) blue circles.

Table 5.2: Summary of T_m's for BECN2, BECN2 CCD:His_6-STX6 SNARE, BECN2(181-250), and BECN2(181-250):His_6-STX6 SNARE.

Protein	T_m (°C) Heating	T_m (°C) Cooling
BECN2 CCD	14.2	15.3
BECN2 CCD: 2His_6-STX6 SNARE	28.1	19.5
BECN2(181-250)	4.6	9.6
BECN2(181-250): 2His_6-STX6 SNARE	27.8	16.3

5.3.7. SEC-SAXS Shows that MBP-BECN2 CCD:His$_6$-STX6 SNARE Complex Forms a Well-Folded Elongated Complex

We used SEC-SAXS to obtain low resolution structural information such as size and shape of the MBP-BECN2 CCD:His$_6$-STX6 SNARE complex. The integrated scattering intensity across different scattering frames (Figure 5.10A) trends similar to the SEC profile, including the presence of a trailing edge shoulder on the main peak. The uniform R_g distribution across the scattering frames corresponding to the peak, indicates a homogenous species (Figure 5.10B). These scattering frames were used for further analysis. The molecular weight calculated from the V_c is ~73.7 kD which is ~ 1.04 times the theoretical molecular weight of 71 kD for the complex. This suggests that the complex may be a heterotrimer in solution. The R_g of the MBP-BECN2 CCD:His$_6$-STX6 SNARE estimated from the Guinier plot and P(r) distribution is ~41 Å (Figure 5.10C and D). Further, the shape of the P(r) distribution curve indicates that the MBP-BECN2 CCD:His$_6$-STX6 SNARE complex has an elongated shape with a D_{max} of ~246 Å (Figure 5.10E). The Kratky plot indicates that MBP-BECN2 CCD:His$_6$-STX6 SNARE is well-folded, (Figure 5.10E).

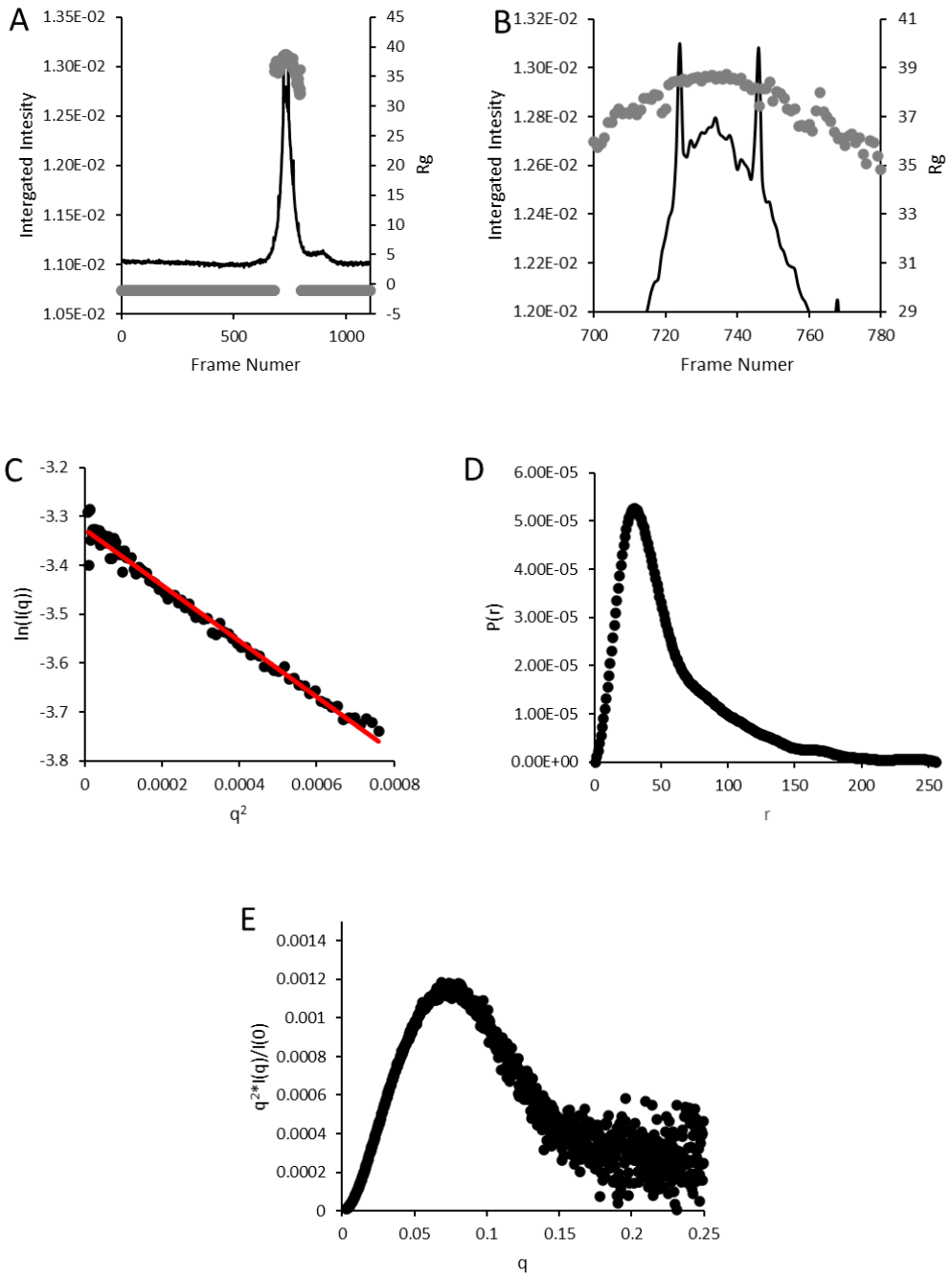

Figure 5.10: SAXS analysis of MBP-BECN2 CCD:His_6-STX6 SNARE. A) Integrated intensity vs frame number in black and Rg vs frame number in grey. B) Zoomed in of (A) to show Rg values over top of peak. C) Guinier plot. D) P(r) pairwise distribution. E) Kratky plot.

We also used SEC-SAXS to investigate the size, shape, and the structure of the BECN2 CCD:His_6-STX6 SNARE complex. The low sample concentration used resulted in low SAXS intensities. The integrated scattering intensity across different scattering frames (Figure 5.11 A)

trends similar to the SEC profile, including the presence of a trailing edge shoulder on the main peak. The uniform R_g distribution across the scattering frames corresponding to the peak, indicates elution of a homogenous species (Figure 5.11 B). These scattering frames were used for further analysis. The molecular weight calculated from the V_c is ~14.9 kD which is ~ 0.48 times the theoretical molecular weight of 30.8 kD for the complex, this shows that BECN2 CCD: 2 His_6-STX6 SNARE may be a heterodimer in solution (Figure 5.11A and B). The R_g of the MBP-BECN2 CCD:His_6-STX6 SNARE estimated from the Guinier plot and P(r) distribution is ~28.2 Å (Figure 5.11C and D). Further, the shape of the P(r) distribution curve indicates that the BECN2 CCD:His_6-STX6 SNARE complex has an elongated shape with a D_{max} of ~150 Å (Figure 5.11E). The Kratky plot indicates that MBP-BECN2 CCD:His_6-STX6 SNARE is partially folded (Figure 5.11E).

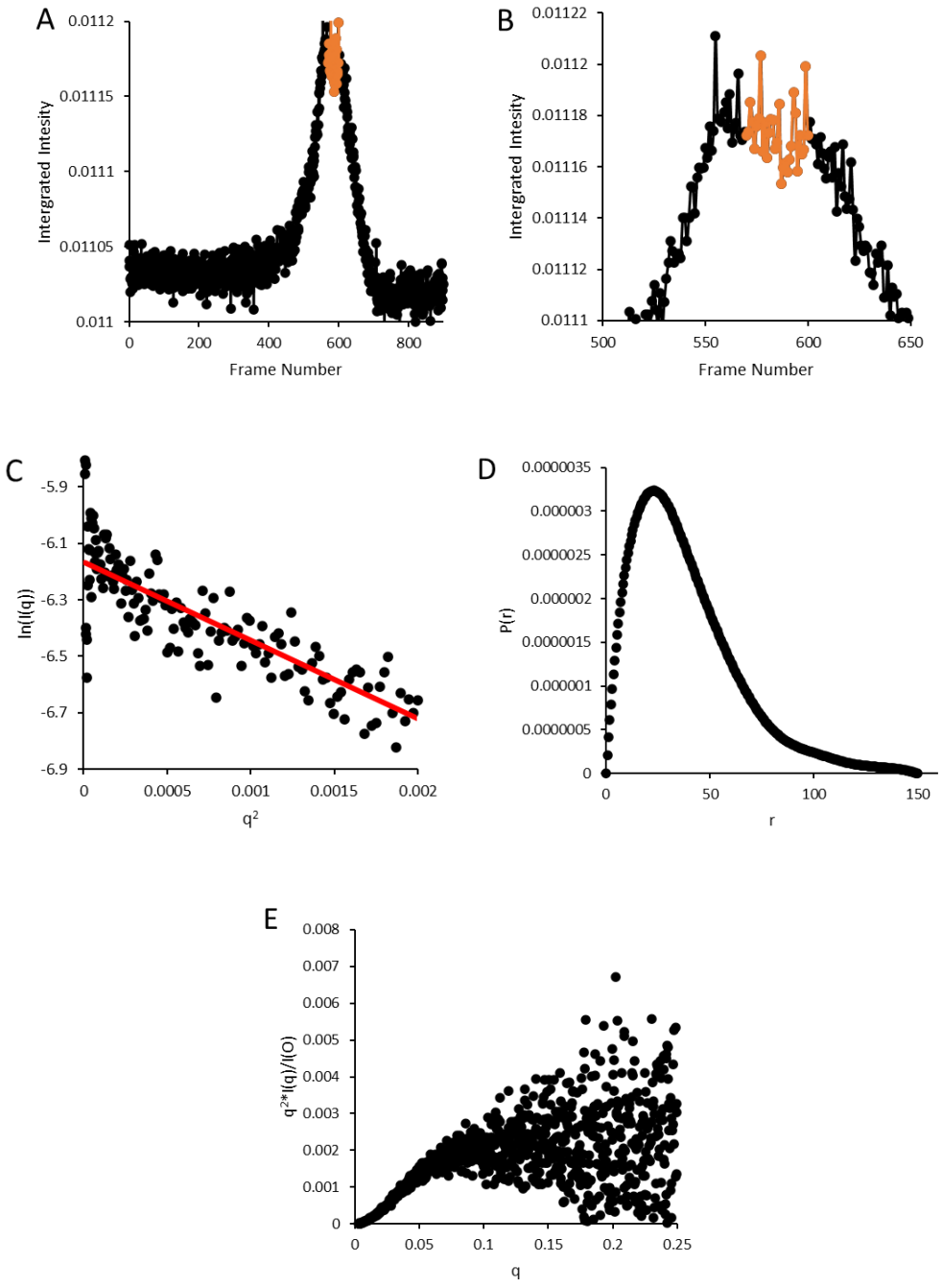

Figure 5.11: SAXS analysis of BECN2 CCD:His$_6$-STX6 SNARE. A) Integrated intensity vs frame number in black and Rg vs frame number in grey. B) Zoomed in of (A) to show Rg values over top of peak. C) Guinier plot. D) P(r) pairwise distribution. E) Kratky plot.

5.3.8. ITC of BECN2 CCD and STX6 SNARE

ITC was used to quantify the thermodynamics of the dissociation of STX6 SNARE constructs. When His$_6$-STX6 SNARE or MBP-STX6 SNARE were titrated into buffer, no heats

of dissociation were detected. We used the MBP-STX6 SNARE protein as it was more stable and enabled more accurate determination of concentration. This is either because when the STX6 SNARE dissociates it does not involve heat release or absorption within the detectable range of the ITC, or the STX6 SNARE does not form a homodimer (Figure 5.12). The second case is most likely, as we have shown that STX6 SNARE is disordered by itself, but becomes helical in complex with another protein, which means that STX6 SNARE is most likely a monomer in solution.

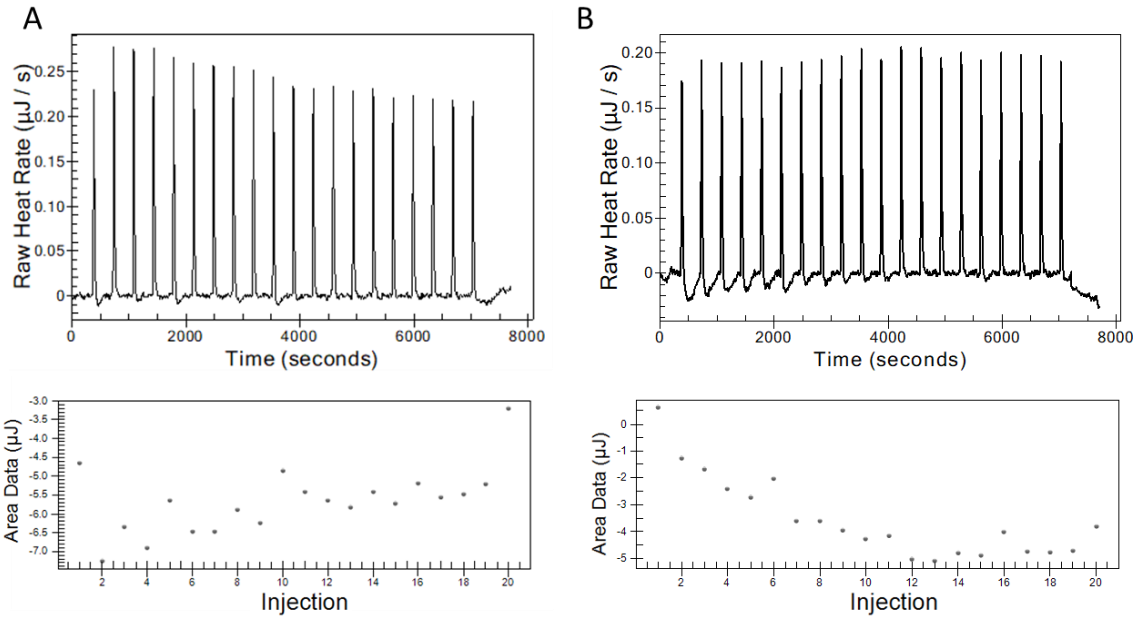

Figure 5.12: ITC binding profiles of the dissociation A) of MBP-STX6 SNARE B) of His6-STX6 SNARE.

We also used ITC to quantify the thermodynamics of binding of BECN2 CCD to STX6 SNARE. We did this by monitoring either the association of the two separate proteins or the dissociation of the heterodimer. For the dissociation of the BECN2 CCD:STX6 SNARE complex, no heats of dissociation were detected (Figure 5.13A), suggesting that either the interaction is very tight or that interaction does not involve heat release or absorption. However, titration of MBP-BECN2 CCD into His_6-STX6 SNARE, produced detectable heats of interaction

but the stoichiometry (n) was very low (Figure 5.13B and Table 5.3). This is likely due to the concentration of His_6-STX6 SNARE being unreliable, and perhaps also because at a concentration of 437 µM, the BECN2 CCD is a homodimer as shown in Chapter 4. Next, we attempted to titrate MBP-STX6 SNARE at a concentration of 614 µM into the BECN2 CCD at a concentration of 58 µM, to ensure that the BECN2 CCD concentration is below its homodimer dissociation constant. In this case we also detected heats of binding, and the n was near one, but we were unable to record the full sigmodal curve, most likely due to the type of interaction taking place (Figure 5.13C and Table 5.3). Therefore, ITC was not suitable for determining binding constants for the interaction between BECN2 CCD and STX6 SNARE.

Table 5.3: Thermodynamics of binding of MBP-BECN2 CCD:His_6-STX6 SNARE dissociation, MBP-BECN2 CCD into His_6-STX6 SNARE, MBP-STX6 SNARE into MBP-BECN2 CCD.

	Kd (µM)	N	ΔH (kJ/mol)	ΔS (J/mol *K)
MBP-BECN2 CCD:His_6-STX6 SNARE dissociation	No Detected			
MBP-BECN2 CCD into His_6-STX6 SNARE	30.7	0.1	-81.99	-193.3
MBP-STX6 SNARE into MBP-BECN2 CCD	49.7	0.965	-32.51	-28.51

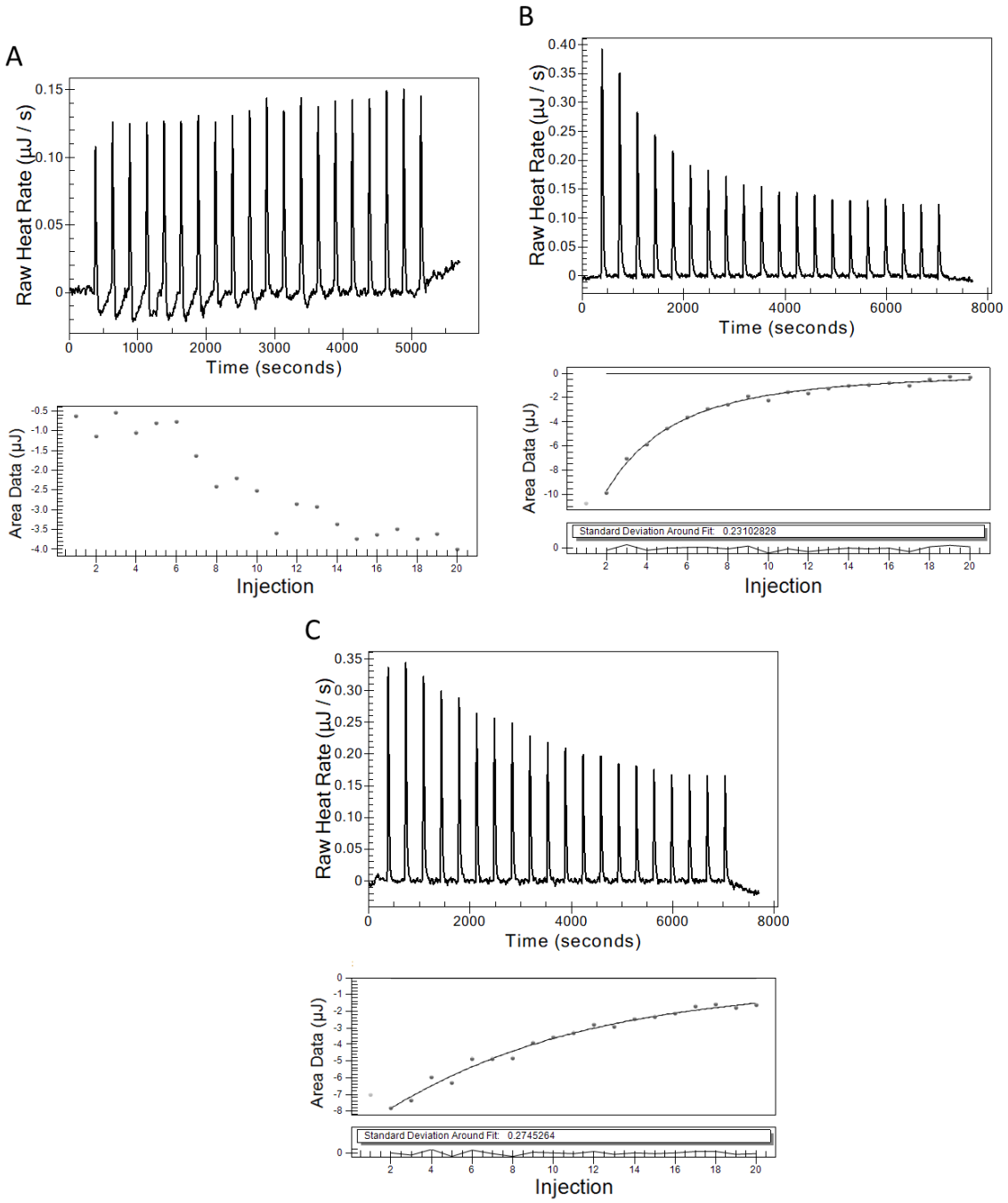

Figure 5.13: ITC binding profiles of A) MBP-BECN2 CCD:His_6-STX6 SNARE dissociation, B) MBP-BECN2 CCD into His_6-STX6 SNARE, C) MBP-STX6 SNARE into MBP-BECN2 CCD.

5.3.9. Crystals From Crystallization Screening for BECN2 CCD:STX6 SNARE

Robotic screening of the BECN2 CCD:STX6 SNARE complex with the MCSG1 and MCSG2 sparse matrix screens in 96-well plates incubated at 20 °C, produced potential crystallization hits that polarized light (Table 5.4). The initial hits from MCSG2 E2 with the

reservoir solution 0.1M Bis-Tris Propane: HCl pH 7, 3.2M Sodium Chloride were optimized, because this condition had the best quality crystals in terms of having a large, single crystals with no visible layering.

Table 5.4: Crystal hits from crystal screens for BECN2 CCD:STX6 SNARE.

Screen & condition	protein: well	Reservoir solution
MCSG1 D3	3:1, 1:1, 1:3	0.1 M Tris HCl pH 8.5, 0.2 M Magnesium Chloride, 30% v/v PEG 400
MCSG1 G3	3:1	0.1 M Bis-Tris Propane: HCl pH 7,1.5 M Ammonium Sulfate
MCSG1 E5	3:1, 1:1, 1:3	0.1 M MES: NaOH pH 6.5, 0.1 M MES: NaOH pH 6.5
MCSG1 C6	3:1, 1:1, 1:3	0.1 M HEPES: NaOH pH 7.5, 0.2 M Magnesium Chloride, 30% v/v PEG 400
MCSG1 G7	3:1	0.1 M Tris HCl pH 8.5, 25% (w/v) PEG 3350
MCSG1 G8	3:1	0.1 M Tris HCl pH 8.5, 0.2 M Ammonium Sulfate, 25% (w/v) PEG 3350
MCSG1 E8	3:1	0.1 M Tris HCl pH 8.5, 1.8 M Ammonium Sulfate
MCSG2 D1	3:1, 1:1	0.1M Tris HCl pH 8.5, 1.5M Ammonium Sulfate
MCSG2 F1	3:1, 1:1, 1:3	0.1M Imidazole HCl pH 8, 0.2M Sodium Chloride, 1M Ammonium Phosphate Dibasic
MCSG2 H1	3:1	0.1M Bis-Tris: HCl pH 6.5, 0.2M Calcium Chloride, 45% MPD
MCSG2 E2	3:1, 1:1, 1:3	0.1M Bis-Tris Propane: HCl pH 7, 3.2M Sodium Chloride
MCSG2 H4	3:1	0.1M Tris HCl pH 8.5, 0.2M Ammonium Acetate, 25% (w/v) PEG 3350
MCSG2 G5	3:1, 1:1, 1:3	0.1M CHES: NaOH pH 9.5, 0.2M Sodium Chloride, 1.26M Ammonium Sulfate
MCSG2 G6	3:1, 1:1	0.1M Sodium Citrate pH 5.5, 0.2M Sodium Chloride, 1M Ammonium Phosphate Dibasic
MCSG2 E6	3:1, 1:1, 1:3	0.1M Sodium Acetate pH 4.5, 1M Ammonium Phosphate Dibasic
MCSG2 C7	3:1	0.1M Tris HCl pH 8.5, 1.5M Ammonium Phosphate Dibasic
MCSG2 B9	3:1, 1:1	0.1M Bis-Tris HCl pH 5.5, 1M Ammonium Sulfate, 1% (w/v) PEG 3350

5.3.10. The BECN2 CCD:STX6 SNARE Complex Forms a Three-Helix Bundle

We determined the 3.1 Å X-ray crystal structure of the BECN2 CCD:STX6 SNARE complex. Data collection and refinement statistics are reported in Table 5.5. Crystals of the BECN2 CCD:STX6 SNARE belong to the $P6_122$ space group, with one copy of the complex in the unit cell. Contrary to our expectation that the two proteins would form a coiled-coil heterodimer, similar to previously characterized interactions of BECN homologs, the BECN2 CCD:STX6 SNARE complex forms a heterotrimeric helical bundle that contains one BECN2 CCD and two STX6 SNARE helices, which we will henceforth call the BECN2 CCD: 2STX6 SNARE 3-helix bundle. Of the two STX6 SNARE helices in this complex, one STX6 SNARE is parallel, and the other is anti-parallel, to the BECN2 CCD, which we will call the parallel STX6 SNARE and anti-parallel STX6 SNARE respectively (Figure 5.14). Electron density corresponding to 58 residues is visible for each STX6 SNARE; with the parallel STX6 SNARE having residues 170-228 visible, and the anti-parallel STX6 SNARE having residues 170-225 visible. BECN2 CCD residues 186-249, form the third helix in the 3-helix bundle, but there is no visible electron density corresponding to BECN2 residues 158-185, indicating that these residues are disordered. The presence of this large, disordered region may result in poor packing of molecules within the crystal, lowering diffraction resolution. Therefore, we decided to create a new BECN2 construct comprising residues 181-250 and attempt structural studies with that protein.

Table 5.5: Summary of X-ray Diffraction Data Collection and Refinement Statistics.

	BECN2 CCD: 2His$_6$-STX6 SNARE
Data Collection Statistics	
Wavelength (Å)	0.97918
Data range (Å)	109.41-3.07 (3.28-3.07)
Space group	$P6_122$
Unit cell parameters	a=126.34, b=126.34, c=158.50
Unique reflections	14575 (2558)
Average multiplicity	37.1 (41.2)
Completeness (%)	100.0 (100.0)
CC1/2	0.999 (0.538)
R_{meas}[a]	0.338 (3.566)
I/σ_I	16.5 (1.5)
Refinement Statistics	
Model	
Chain A (BECN2)	64
Chain B (Parallel STX6)	58
Chain C (Anti-parallel STX6)	59
Water	36
Data range (Å)	109.41-3.07
R_{work}[b](%)	29.12
R_{free}[b,c] (%)	30.26
Average B-values (Å^2)	
Macromolecules	109.9
Water	
RMSDs from target values	
Bond lengths (Å)	0.013
Bond Angles (°)	2.621
Ramachandran favored (%)	91.5
Ramachandran outliers (%)	0

Values in parentheses pertain to the outermost shell of data.

[a] $R_{meas} = \sum_{hkl}(n/n-1)^{1/2} \sum_{h,i} | I_{hkl,i} - \langle I_{hkkl} \rangle | / \sum_{hkl} \sum_{h,i} I_{hkl,i}$

[b] R factor = $\sum_h \big| |F_{obs}| - |F_{calc}| \big| / \sum_h |F_{obs}|$

[c] Test set for R_{free} consisted of 5% of data.

Figure 5.14: X-ray crystal structure of the BECN2 CCD: 2STX6 SNARE heterotrimer helical bundle

5.3.11. Expression and Purification of BECN2(181-250) Constructs

The MBP-BECN2(181-250) fusion protein was purified by amylose affinity chromatography followed by SEC. The SEC elution profile contains one peak with 2 shoulders (Figure 5.15). SDS-PAGE shows that both, the peak and the leading-edge shoulder contain MBP-BECN2(181-250), suggesting that the MBP-BECN2(181-250) eluting in the leading-edge shoulder contains is likely an oligomer, while the trailing-edge shoulder contains MBP-BECN2(181-250) as well as lower molecular weight contaminants. The molecular weight of the MBP-BECN2(181-250) calculated based on the elution volume of 11.74 mL from SEC is 154 kD which is ~1.5 times larger than the theoretical molecular weight of 100 kD for a MBP-BECN2(181-250) homodimer calculated from the amino acid sequence. This suggests that MBP-BECN2(181-250) is an elongated dimer. The final yield of the purified MBP-BECN2(181-250) was 7.2 mg from one liter of bacterial culture.

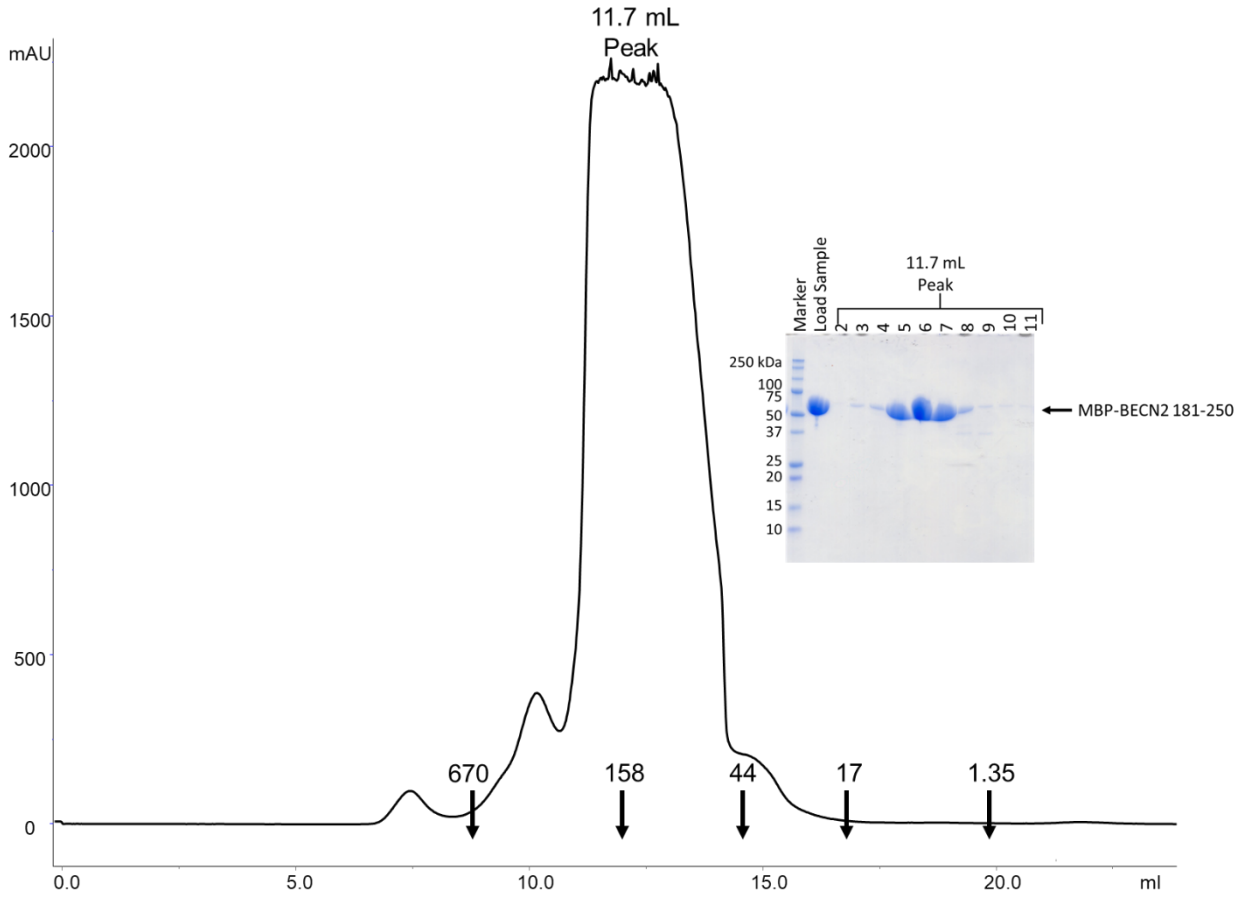

Figure 5.15: Size exclusion chromatogram and Coomassie-stained SDS-PAGE gel of MBP-BECN2(181-250). The elution positions of SEC Superdex 200 increase 10/300 standards are indicated by arrows and corresponding molecular weight.

BECN2(181-250) was purified by amylose affinity chromatography and ion exchange followed by SEC. The SEC elution profile contains one peak with a leading-edge shoulder (Figure 5.16). The SDS-PAGE shows that the main peak contains BECN2(181-250) while the shoulder contains a higher molecular weight contaminant. The molecular weight of BECN2(181-250) calculated based on the elution volume of 14.2 mL from SEC is 43.7 kD, which is ~2.5 times larger than the theoretical molecular weight of 17.2 kD for the BECN2(181-250) homodimer calculated from the amino acid sequence. This suggests that BECN2(181-250) is an elongated homodimer. The final yield of the purified BECN2(181-250) obtained from one liter of bacterial culture was 1.2 mg.

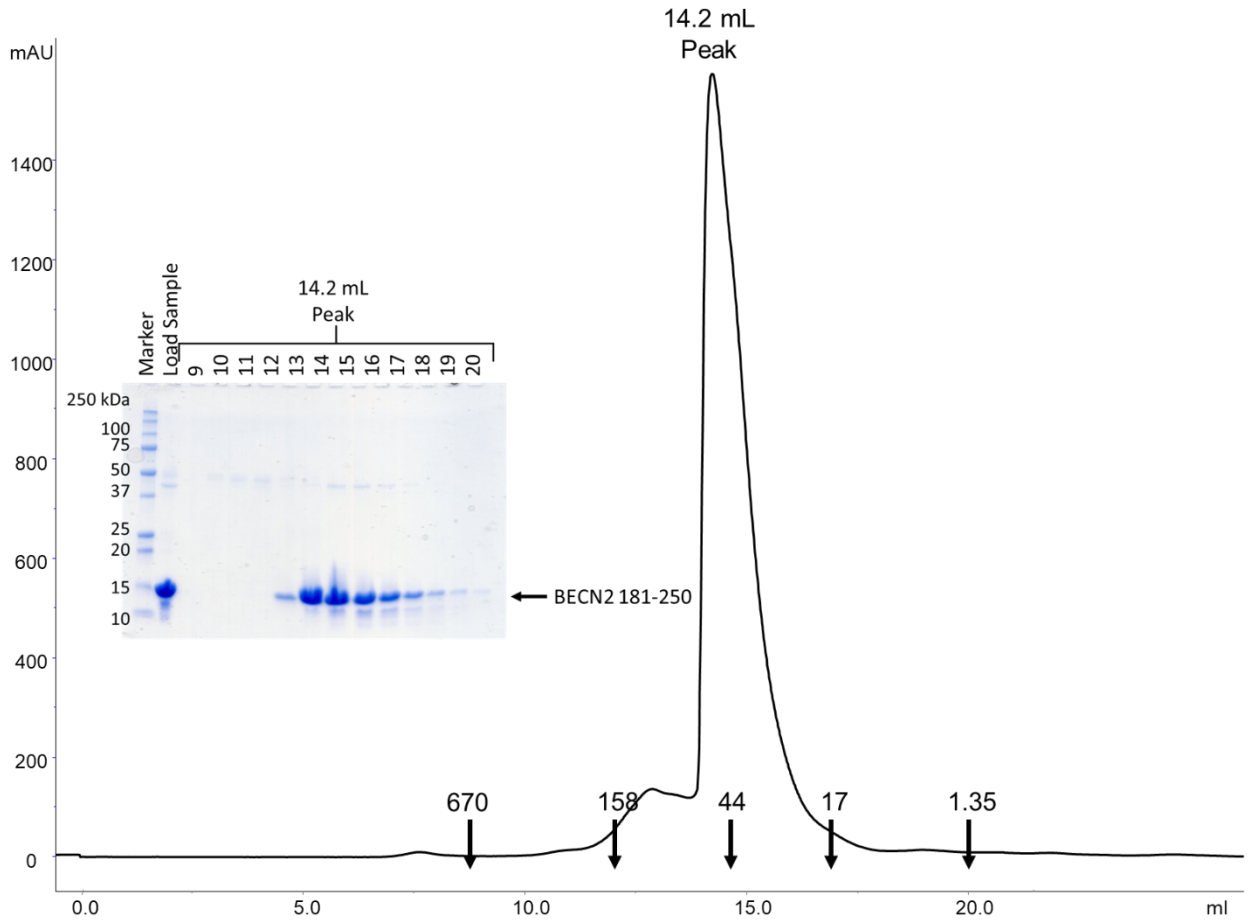

Figure 5.16: Size exclusion chromatogram and Coomassie-stained SDS-PAGE gel of BECN2(181-250). The elution positions of SEC Superdex 200 increase 10/300 standards are indicated by arrows and corresponding molecular weight.

5.3.12. Expression and Purification of BECN2(181-250):His_6-STX6 SNARE Complexes

BECN2(181-250):His_6-STX6 SNARE fusion protein was purified by Ni^{++}-NTA affinity, amylose affinity chromatography, and SEC. The SEC elution profile has one main peak (Figure 5.17), and SDS-PAGE shows the peak contains BECN2(181-250):His_6-STX6 SNARE.

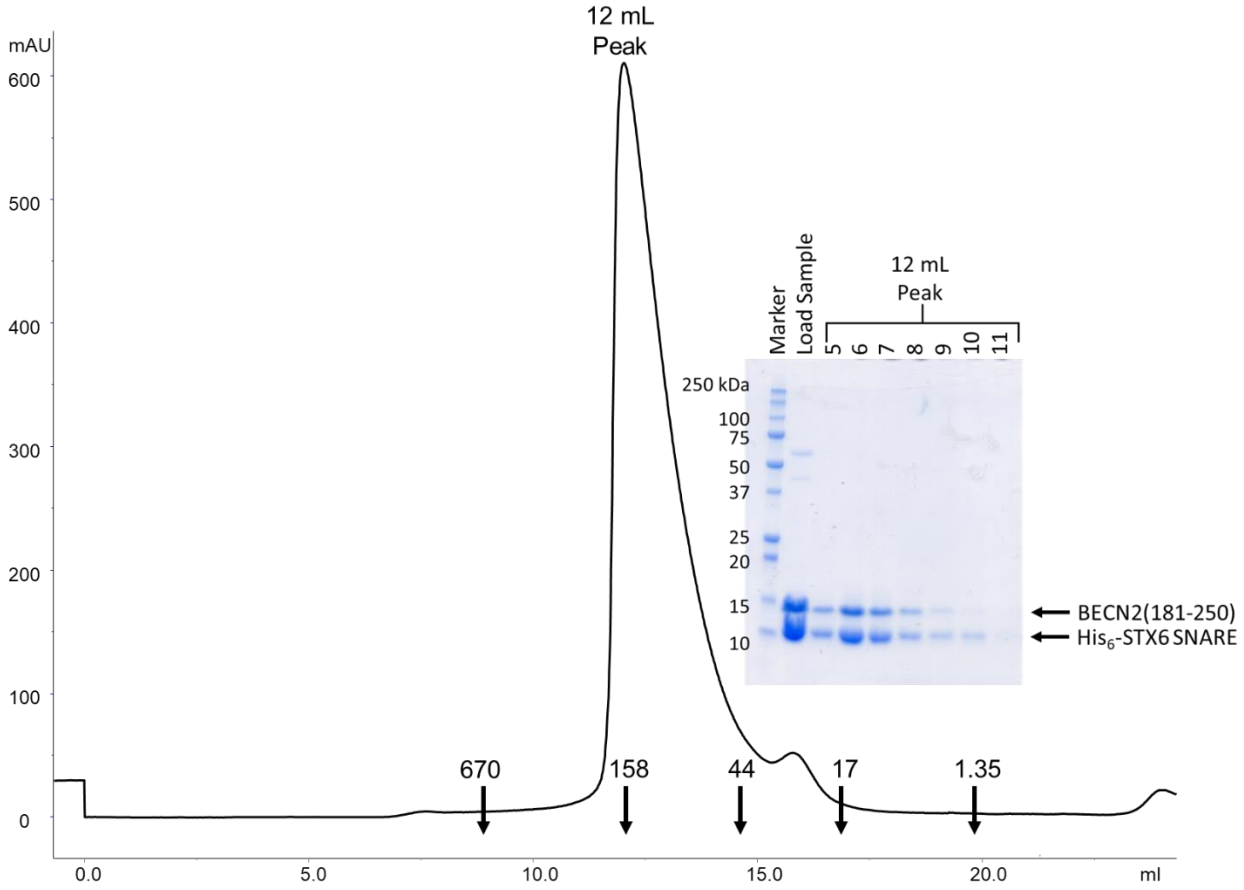

Figure 5.17: Size exclusion chromatogram and Coomassie-stained SDS-PAGE gel of BECN2(181-250):His6-STX6 SNARE. The elution positions of SEC Superdex 200 increase 10/300 standards are indicated by arrows and corresponding molecular weight.

The molecular weight of the BECN2(181-250):His_6-STX6 SNARE calculated based on the elution volume from SEC is 148.6 kD which is ~8.2 times larger than the theoretical molecular weight of 18.2 kD for the BECN2(181-250):His_6-STX6 SNARE heterodimer calculated from the amino acid sequence. This suggests that BECN2(181-250):His_6-STX6 SNARE is an elongated heterodimer protein. The final yield of the purified BECN2(181-250):His_6-STX6 SNARE obtained from one liter of bacterial culture was 0.5 mg. Notably, both the yield of purified BECN2 CCD: 2STX6 SNARE complex and BECN2(181-250): 2STX6 SNARE complex is comparable, indicating they have comparable stability.

5.3.13. Relative to the BECN2 CCD, the BECN2(181-250) is Less Helical and Stable, While the Complex with SNARE has Increased Helical Content and Stability

Analysis of the CD spectrum (Figure 5.18) of BECN2(181-250) indicates that, of a total of ~75 residues, only ~37 adopt a helical conformation (Figure 5.18), which is lower than the ~55 residues in helical conformation in the BECN2 CCD, likely because the shorter construct homodimerizes more weakly than the CCD, and homodimerization is required for stabilization of helical conformation.

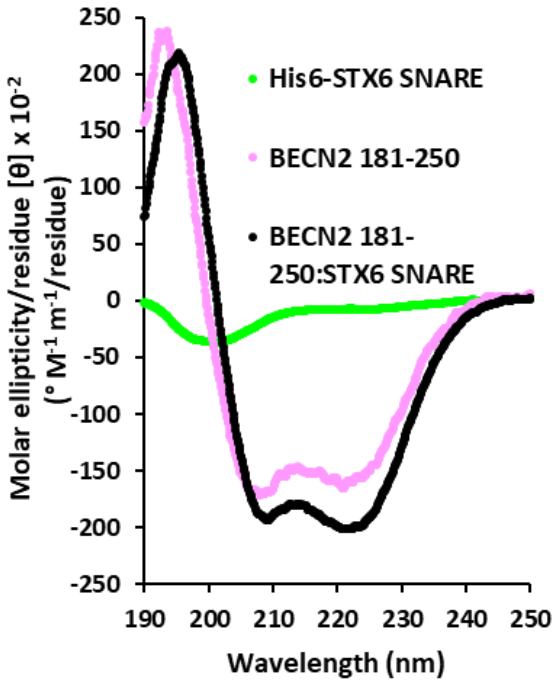

Figure 5.18: CD Spectra at 4 °C of A) His_6-STX6 SNARE (green), BECN2(181-250) (violet), BECN2(181-250): $2His_6$-STX6 SNARE (black).

In contrast, the helical content estimated from analysis of the CD spectrum (Figure 5.18) of the BECN2(181-250): 2STX6 SNARE complex indicates that ~152 residues adopt a helical conformation (Figure 5.18 and Table 5.1), which is substantially more residues in helical conformation than either BECN2(181-250) or the STX6 SNARE alone, and similar to the

number observed for the STX6 SNARE complex with the full-length BECN2 CCD. Notably however, the fraction of residues in helical conformation in the BECN2(181-250):STX6 SNARE complex is higher than that estimated for the STX6 SNARE complex with the complete BECN2 CCD, likely this complex does not include the disordered BECN2 region comprising residues 158-180, which were observed in the 3.1 Å crystal structure.

Quantification of T_m using thermal denaturation coupled to CD measurements at wavelength 222 nm shows that BECN2(181-250) has a T_m of 4.6 °C, as calculated from the forward, heating curve, and a reverse, cooling T_m of 9.6 °C (Figure 5.9C and Table 5.3). As for the BECN2 CCD, we were unable to record the complete sigmoidal curve for the heating experiment. Therefore, it is likely that the heating T_m is inaccurate, and is actually more similar to the cooling T_m. Notably, the T_m of this shorter construct is markedly lower than the T_m of the BECN2 CCD, consistent with the reduced helical content of the shorter construct, confirming that the BECN2(181-250) homodimerizes more weakly than the BECN2 CCD, and that homodimerization is required to stabilize helical structure of this region.

The BECN2(181-250): 2STX6 SNARE complex has a heating T_m of 27.8 °C and a cooling T_m of 16.3 °C (Figure 5.9D and Table 5.2). The cooling, T_m of the complex is likely inaccurate due to precipitation of STX6 SNARE during the experiment, similar to that observed for experiments with the BECN2 CCD:STX6 SNARE complex. The BECN2(181-250):STX6 SNARE complex is significantly more stable than either of the individual proteins by themselves. Importantly however, the T_m of both the BECN2(181-250): 2STX6 SNARE and the BECN2(181-250): 2STX6 SNARE complexes is similar, indicating that the additional residues comprising the BECN2 CCD do not contribute to the interaction.

5.3.14. CD with TFE

TFE induces a disorder to helix transition, the effects of TFE on BECN2(181-250) were determined. With the addition of 10% and 25% TFE there was an increase in the helicity of BECN2(181-250) to approximately 87% helical, as compared to approximately 50% helical content in no TFE (Figure 5.19, Table 5.6). However, at 40% TFE, the helical content does not increase, which is likely due to that concentration of TFE not having an effect on helical content (Figure 5.19, Table 5.6).

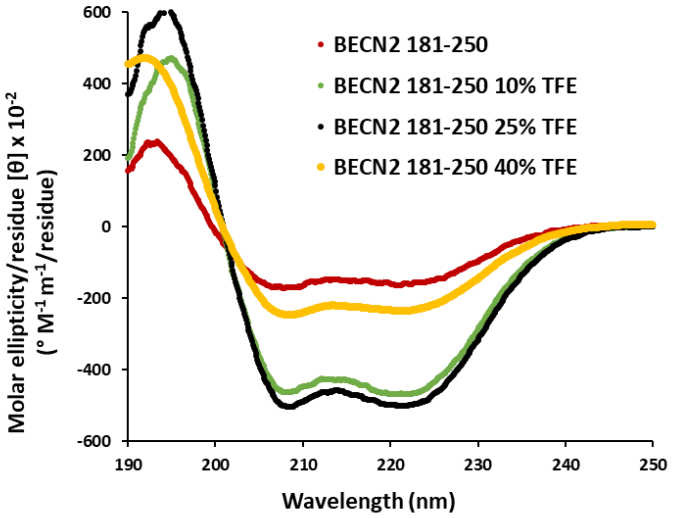

Figure 5.19: CD Spectra for BECN2(181-250) in different concentrations of TFE.

Table 5.6: The estimated secondary structure of BECN2(181-250) in different concentrations of TFE.

TFE Concentration	Residues (Percent)			
	Helix	Strand	Coil + Turn	Total
0%	37.3 ± 0.1 (49.7)	5.9 ± 1.4 (7.8)	31.9 ± 1.5 (42.5)	75.1 (100)
10% TFE	65.2 ± 9.8 (86.9)	3.9 ± 3.9 (5.2)	5.9 ± 5.9 (7.9)	75 (99.7)
25% TFE	65.9 ± 9.2 (87.8)	3.4 ± 3.4 (4.5)	5.9 ± 5.9 (7.8)	75.2 (100.1)
40% TFE	51.7 ± 2.7 (68.9)	2.4 ± 0.2 (3.2)	21.2 ± 2.7 (28.3)	75.3 (100.4)

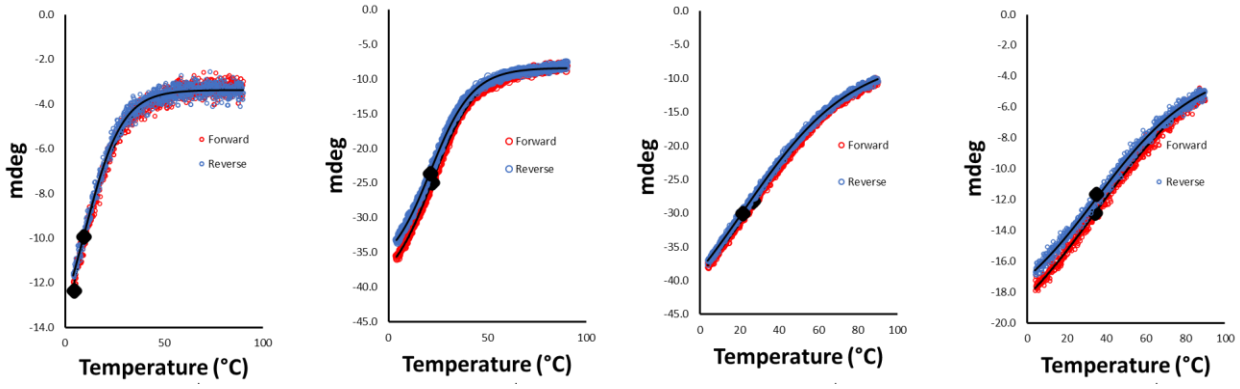

Figure 5.20: Melting temperature of BECN2(181-250) in different concentrations of TFE. Forward is shown in red circles and reverse in blue circles.

Table 5.7: Melting temperature of BECN2(181-250) in different concentrations of TFE for forward and reverse.

Protein	Forward Tm (°C)	Reverse Tm (°C)
BECN2(181-250)	4.6	9.6
BECN2(181-250) 10% TFE	22.2	21.2
BECN2(181-250) 25% TFE	26.8	21.8
BECN2(181-250) 40% TFE	34.4	35.1

The melting temperatures are measured in increasing amounts of TFE. This shows an increase in the T_m from 4.6 °C with 0% TFE, to 22.2 °C with 10% TFE, 26.8 °C with 25% TFE, and 34.4 °C with 40% TFE (Figure 5.20, Table 5.7). This shows that 10% and 25% TFE increases helicity of BECN2(181-250) and also increases the melting temperature, leading to an increase in the stability of the BECN2(181-250) to be used for other biophysical experiments.

5.3.15. ITC using BECN2(181-250)

Using the shorter construct that we made based on the 3.1 Å X-ray crystal structure we first determined the dissociation constant of the homodimer of the BECN2(181-250). We found that the BECN2(181-250) homodimer has a dissociation constant of 327.5 µM which is significantly weaker than the dissociation constant of 138 µM for the BECN2 CCD[20] (Figure 5.21A and Table 5.8). We also attempted to quantify the binding of MBP-STX6 SNARE and

MBP-BECN2(181-250), but no heats of binding detected (Figure 5.21B and Table 5.8). This shows that the interaction between BECN2(181-250) and STX6 SNARE interaction does not involve heat release or absorption. Therefore, ITC was not suitable for determining binding constants for the interaction between BECN2(181-250) and STX6 SNARE.

Table 5.8: Thermodynamics of binding of BECN2(181-250) dissociation, MBP-STX6 SNARE into MBP-BECN2(181-250).

	Kd (μM)	ΔH (kJ/mol)	ΔS (J/mol *K)
BECN2(181-250) dissociation	327.5 ± 16.2	106.1 ± 4.4	295.5 ± 15.5
MBP-STX6 SNARE into MBP-BECN2(181-250)	No Binding Detected		

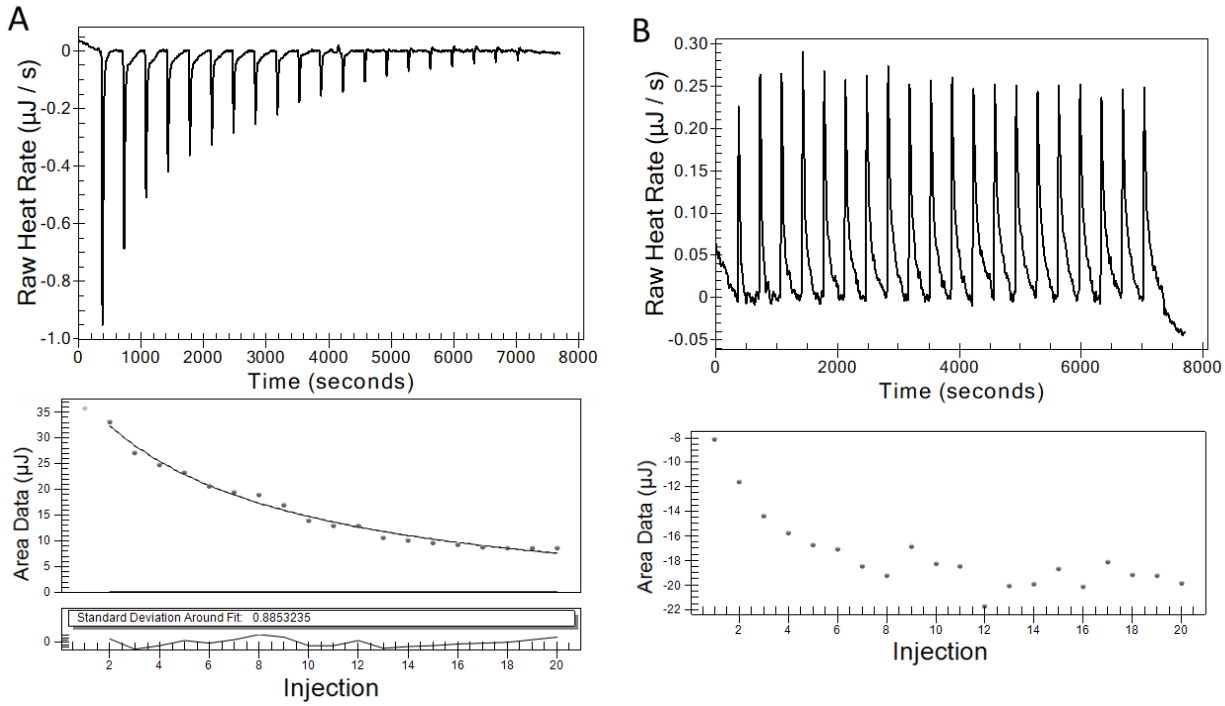

Figure 5.21: ITC binding profiles of A) BECN2(181-250) dissociation, B) MBP-STX6 SNARE into MBP-BECN2(181-250).

5.3.16. MST

We used MST to determine the binding constant of MBP-BECN2(181-250) and MBP-STX6 SNARE. Our initial experiments showed that our interaction might have a double binding event, as indicated by the maximum in the middle and decreasing values on both sides of the

curve (Figure 5.22A). We started by analyzing both events, with the binding event at the lower concentrations having a Kd of 81.2 nM (Figure 5.22B). With the second binding event at the higher concentrations having a Kd of 59.1 µM (Figure 5.22C). In order to determine if this is a true double-binding event we tested different concentrations of MBP-STX6 SNARE as the ligand. We tested lower concentrations of MBP-STX6 SNARE with the starting concentration being 78 µM (Figure 5.22D) and 39 µM (Figure 5.22E). From these lower concentrations of MBP-STX6 SNARE, we were not able to detect binding (Figure 5.22D and 5.22E). We also tested MBP-STX6 SNARE with the starting concentration at 82.5 µM and a higher concentration of TWEEN 20 at 0.1% (v/v) (Figure 5.22F and 5.22G). From this, we found that there was higher aggregation in the samples (Figure 5.22F) and that when analyzed with the aggregation it has a Kd of 53.7 µM (Figure 5.22G). Based on the melting temperature of the complex and BECN2(181-250) we determined that we needed to find a way to increase the stability of the proteins to perform MST and get good binding affinities.

In order to increase the stability of the MBP-BECN2(181-250) we used 10% TFE in the experiments, as we determined with CD that 10% TFE does increase the stability of BECN2(181-250). Using the 10% TFE in the initial binding check caused a lot of aggregation in the samples (Figure 5.22H). We tested one binding affinity to see if we could still calculate the binding of the interaction. We found that six of the 16 capillaries had aggregation and if we removed them, we were unable to detect binding (Figure 5.22I). From this, we determined that MST would not work to determine the binding affinities of MBP-BECN2(181-250) and MBP-STX6 SNARE.

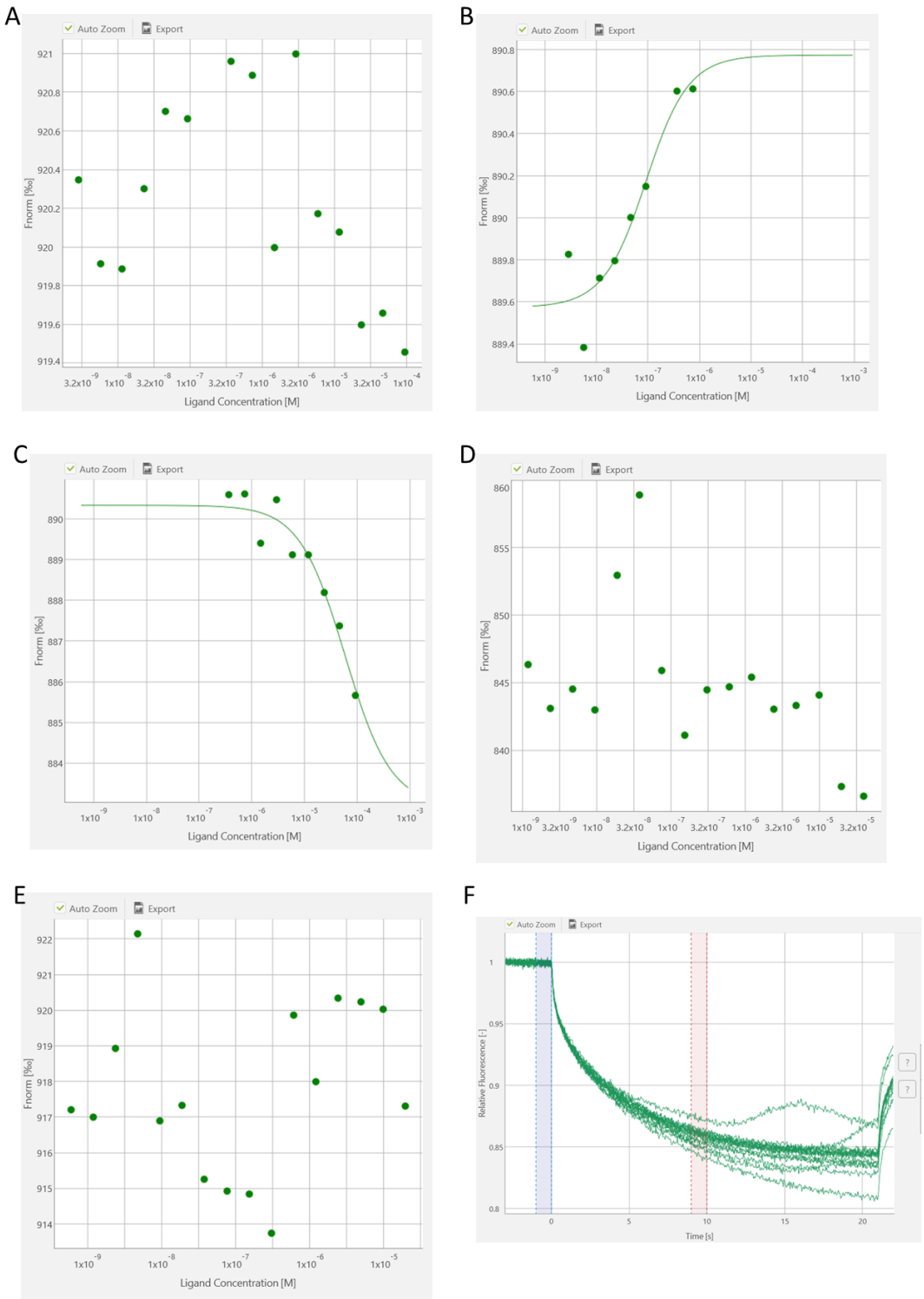

Figure 5.22: MST experiments. A) Initial experiments showing possible double binding. B) Lower concentration binding event from A. C) Higher concentration binding event from A. D-E) Testing lower concentrations of MBP-STX6 SNARE. F-G) Testing higher concentrations of MBP-STX6 SNARE with a higher concentration of TWEEN-20. H) Initial binding check using 10% TFE. I) Binding affinity experiment using 10% TFE.

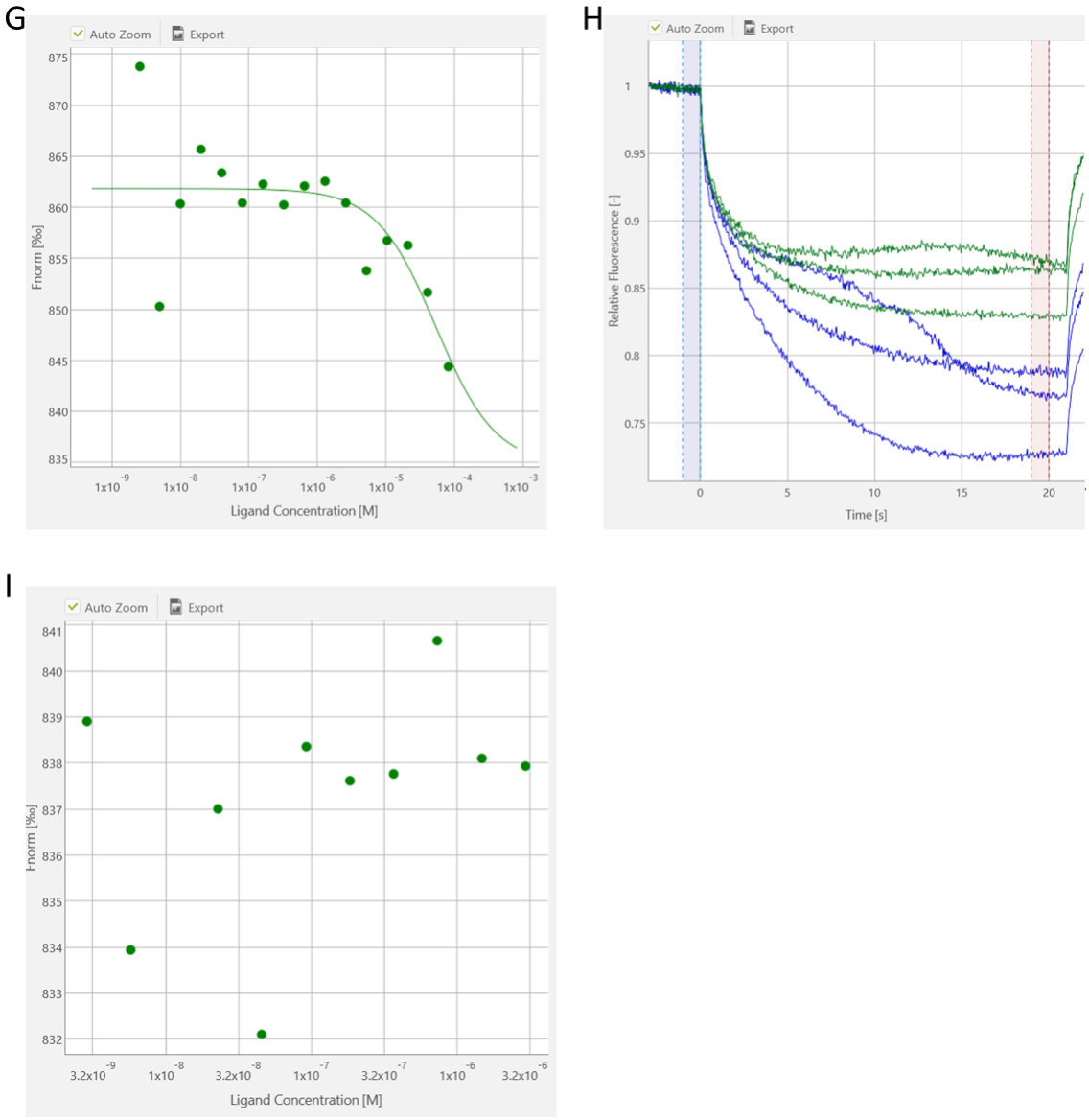

Figure 5.22 Continued: MST experiments. A) Initial experiments showing possible double binding. B) Lower concentration binding event from A. C) Higher concentration binding event from A. D-E) Testing lower concentrations of MBP-STX6 SNARE. F-G) Testing higher concentrations of MBP-STX6 SNARE with a higher concentration of TWEEN-20. H) Initial binding check using 10% TFE. I) Binding affinity experiment using 10% TFE.

5.3.17. Crystallization of the BECN2(181-250):STX6 SNARE Complex

Robotic screening of the BECN2(181-250):STX6 SNARE complex with the MCSG1 and MCSG2 sparse matrix screens in 96-well plates incubated at 20 °C, produced potential crystallization hits that polarized light (Table 5.9).

Table 5.9: Crystal hits from crystal screens for BECN2(181-250):STX6 SNARE.

Screen condition	protein: well	Reservoir solution
MCSG2 D2	3:1, 1:1, 1:3	0.2M Potassium Acetate, 20% w/v PEG 3350
MCSG2 E2	3:1, 1:1, 1:3	0.1M Bis-Tris Propane: HCl pH 7, 3.2M Sodium Chloride
MCSG2 H5	3:1	0.1M Tris HCl pH 8.5, 3.2 M Sodium Chloride
MCSG2 B12	3:1	0.1M Bis-Tris: HCl pH 5.5, 0.2M Sodium Chloride

A few potential hits were optimized using manual trays. The crystals used to collect the best diffraction data were grown in a 3:1 ratio of protein stock:reservoir solution comprising 0.1 M Tris pH 7.5 and 2.8 M NaCl.

5.3.18. Structure of the BECN2(181-250): 2STX6 SNARE Heterotrimeric Complex

Crystals of the BECN2(181-250): 2STX6 SNARE complex also belonged to the $P6_122$ space group, with a unit cell that is isomorphous to the crystals of the complex including the complete BECN2 CCD. The BECN2(181-250): 2STX6 SNARE complex crystals diffracted to an improved resolution of 2.65 Å (Table 5.10). Similar to the crystal structure of the BECN2 CCD: 2STX6 SNARE complex, the structure of BECN2(181-250): 2STX6 SNARE complex consists of a heterotrimeric helical bundle that contains one BECN2(181-250) and two STX6 SNAREs, with one STX6 SNARE parallel and the other anti-parallel to BECN2(181-250) (Figure 5.23). Electron density corresponding to 62 BECN2 CCD residues, residues 185-247, is visible, very similar to what was observed when the complete BECN2 CCD was used for crystallization. The parallel and anti-parallel STX6 SNAREs include 60 and 59 residues respectively, comprising residues 170-227 and 170-226 respectively, as well as three residues, Ser-His-Met, from the linker preceding the SNARE domains.

Table 5.10: X-ray Diffraction Data Collection and Structure Refinement Statistics.

	BECN2 CCD: 2His$_6$-STX6 SNARE (wrong)	BECN2 CCD: His$_6$-STX6 SNARE (correct)	BECN2 181-250: His$_6$-STX6 SNARE
Data Collection Statistics			
Wavelength (Å)	0.97918		1.03317
Data range (Å)	109.41-3.07 (3.28-3.07)		108.21-2.65 (2.69-2.65)
Space group	P6$_1$22		P6$_1$22
Unit cell parameters	a=126.34, b=126.34, c=158.50		a=124.95, b=124.95, c=159.03
Unique reflections	14575 (2558)		21904 (1061)
Average multiplicity	37.1 (41.2)		20.0 (19.5)
Completeness (%)	100.0 (100.0)		100.0 (100.0)
CC1/2	0.999 (0.538)		0.999 (0.383)
R_{meas}[a]	0.338 (3.566)		0.154 (5.950)
I/σ_I	16.5 (1.5)		13.3 (0.7)
Refinement Statistics			
Model			
Chain A (BECN2)	64	64	61
Chain B (Parallel STX6)	58	58	60
Chain C (Anti-parallel STX6)	59	59	59
Water	36	36	65
Data range (Å)	109.41-3.07	109.41-3.07	108.21-2.65
R_{work}[b](%)	29.12	25.3	21.62
R_{free}[b,c] (%)	30.26	28.3	25.27
Average B-values (Å^2)			
Macromolecules	109.9	115.805	87.177
Water		99.958	88.509
RMSDs from target values			
Bond lengths (Å)	0.013	0.0118	0.0107
Bond Angles (°)	2.621	2.283	2.0021
Ramachandran favored (%)	91.5	94.7	98.3
Ramachandran outliers (%)	0	0	0

Values in parentheses pertain to the outermost shell of data.

[a] $R_{meas} = \sum_{hkl}(n/n-1)^{1/2} \sum_{h,i} | I_{hkl,i} - \langle I_{hkkl} \rangle | / \sum_{hkl} \sum_{h,i} I_{hkl,i}$

[b] R factor = $\sum_h \big| |F_{obs}| - |F_{calc}| \big| / \sum_h |F_{obs}|$

[c] Test set for R_{free} consisted of 5% of data.

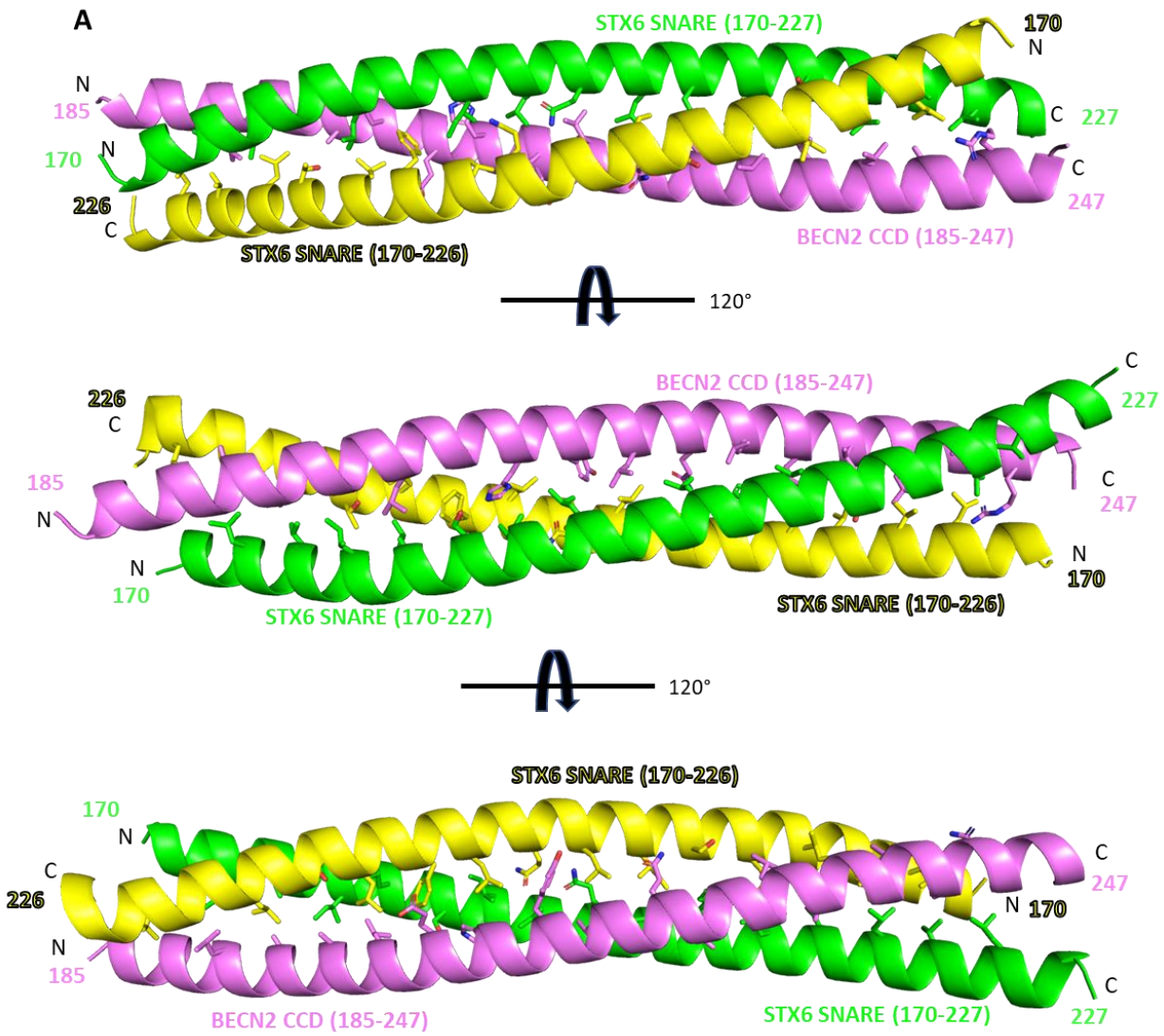

Figure 5.23: X-ray crystal structure of the BECN2(181-250):STX6 SNARE heterotrimer helical bundle: A: Three views of the complex rotated 120° about the X-axis. BECN2(181-250) is violet, the parallel STX6 SNARE is green and the anti-parallel STX6 SNARE is yellow. Interface residues are shown as stick, with atoms colored by type- oxygen: red, nitrogen: blue, sulfur: orange, and carbon: according to protein.

5.3.19. Shift in the 3.1 Å Structure

Comparing the structure of the BECN2(181-250): 2STX6 SNARE complex at 2.65 Å, to the 3.1 Å structure of BECN2 CCD: 2STX6 SNARE, we found that the anti-parallel STX6 SNARE in the 3.1 Å structure was offset by one helical turn toward the N terminal (Figure 5.25). The improved 2.65 Å electron density map showed that a tyrosine and histidine were placed in

wrong positions. Since the higher resolution structure was more likely to be correct- we fit the high-resolution structure into the electron density maps for the 3.1 Å data and redid the refinement. This improved the refinement statistics (Table 5.10) and improved the fit to the electron density (Figure 5.24). This clearly indicates that the structure built with only the low-resolution data was incorrect. The RMSD between the wrong structure and the correct structure is 0.386 (Figure 5.25).

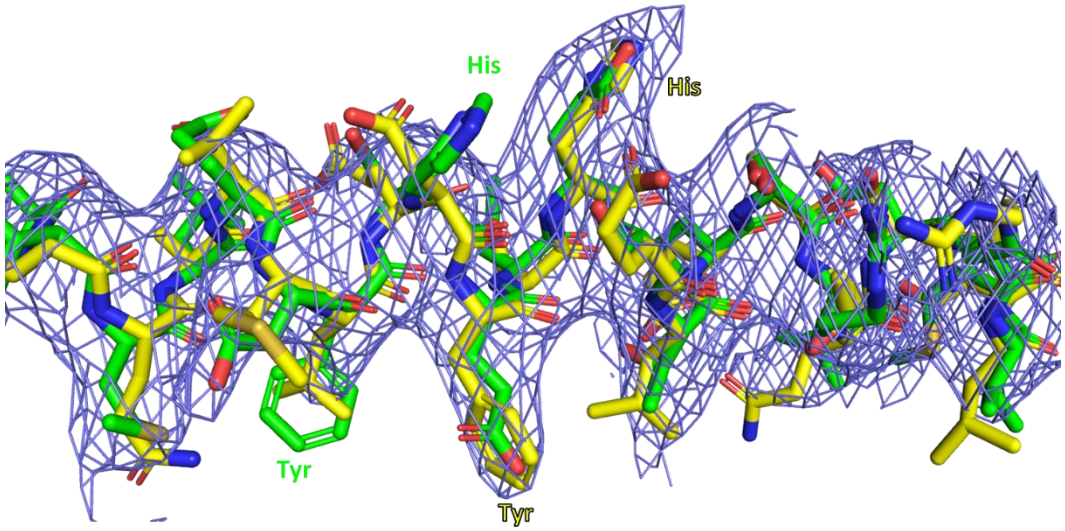

Figure 5.24: Illustration of how the correct structure (yellow) fits better than the wrong structure (green) to the electron density in blue mash.

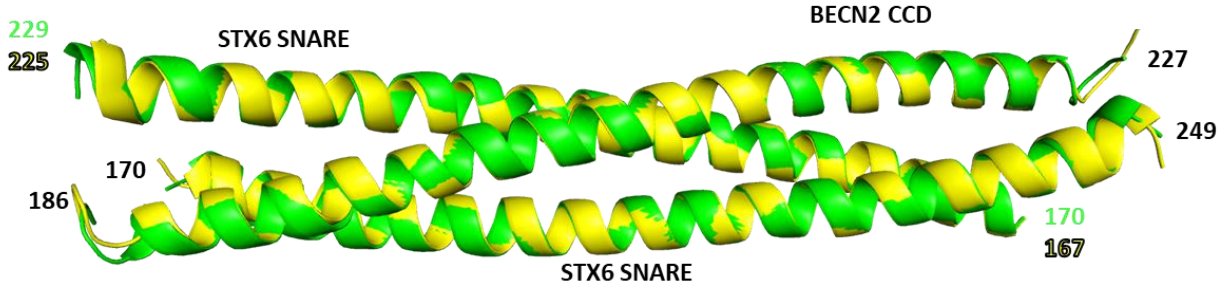

Figure 5.25: Superimposed X-ray crystal structures of the BECN2 CCD: STX6 SNARE wrong structure (green) and the BECN2 CCD:STX6 SNARE correct structure (yellow).

The structure of the BECN2(181-250): 2STX6 SNARE complex is almost identical to that of the corrected BECN2 CCD: 2STX6 SNARE complex, superimposing with an RMSD of 0.286 Å over 182 Ca atoms (Figure 5.26).

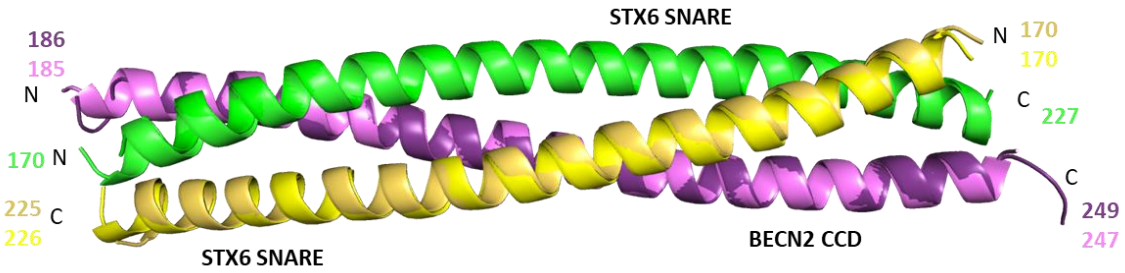

Figure 5.26: Superimposed X-ray crystal structures of the BECN2 CCD: STX6 SNARE and the BECN2(181-250):STX6 SNARE heterotrimer helical bundles. For the BECN2 CCD: STX6 SNARE heterotrimer, the BECN2 CCD is dark violet, the parallel STX6 SNARE is dark green, and the anti-parallel STX6 SNARE is dark yellow. In the BECN2(181-250): STX6 SNARE heterotrimer, BECN2 CCD is violet, the parallel STX6 SNARE is dark green, and the anti-parallel STX6 SNARE is yellow.

The electrostatic surface of BECN2(181-250): 2STX6 SNARE heterotrimer is relatively neutral except the central region, which is relatively negative charged (Figure 5.27), suggesting that this may serve as a pocket for binding a basic residue such as Arginine from an R-SNARE.

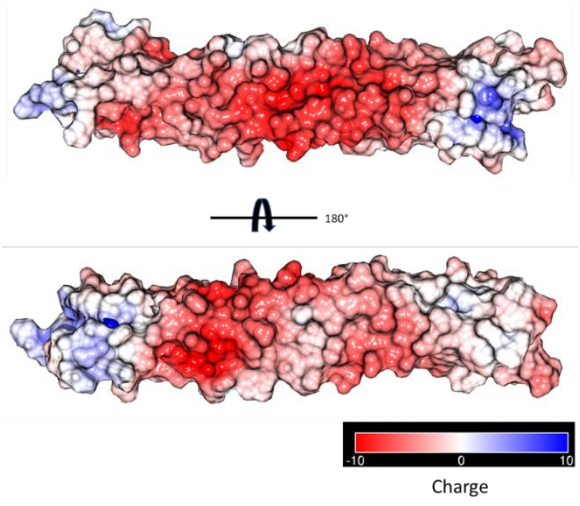

Figure 5.27: Electrostatic surface of the BECN2(181-250):STX6 SNARE complex generated by APBS.

5.3.20. The BECN2(181-250): 2STX6 SNARE Interface

The buried surface area of the heterotrimer is 6784.9 $Å^2$, which constitutes ~37.7% of the combined surface area of the three helices of the heterotrimer. The parallel and anti-parallel STX6 SNARE have buried surface areas of 2347.9 $Å^2$ and 2314.5 $Å^2$ respectively, corresponding to ~ 39.6% and ~40.2% of the total surface area of each helix. The BECN2(181-250) has a buried surface area of 2122.4 $Å^2$, which is ~33.7% of its total surface area. Notably, this is larger than the 1569.23 $Å^2$ of surface area of the equivalent residues buried upon BECN2 CCD homodimerization, wherein BECN2 residues 181-250 pack against BECN2 residues 160-222 from the partner CCD.

These "packing" residues are located at the "a" and "d" positions of heptad amino-acid repeats (*a-b-c-d-e-f-g*), similar to the arrangement of interacting residues that stabilize CCDs[90] (Figure 5.28). The three-helix bundle is stabilized by 15 layers of three packed residues, one contributed by each helix (Figure 5.28A). The BECN2 residues that pack against the STX6 helices are L194, A197, A201, L204, E208, H211, Y215, L218, Q222, L225, L229, V232, L236, A239, and R243, all of which are also involved in the BECN2 CCD homodimer interface[20]. Both the parallel and anti-parallel STX6 helices contribute the same residues to the packing interface: L173, V176, I180, L183, S187, I190, L194, Q197, L201, F204, L208, T211, L215, V218, and L222.

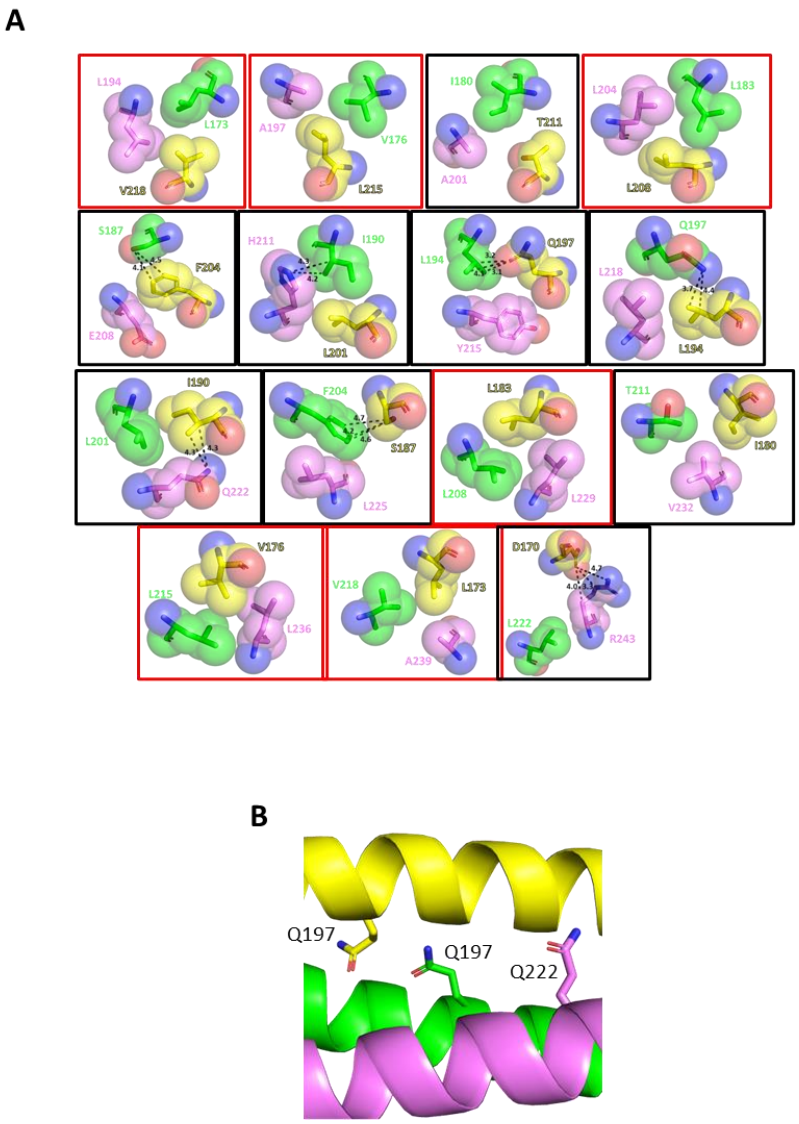

Figure 5.28: Interacting residue layers stabilizing the complex of BECN2(181-250):STX6 SNARE. A) Close-up of each packing interface layer. Proteins and atoms are colored as in Figure 5.24. Polar bonds are indicated by dashed lines. Hydrophobic layers are boxed in red.

Of the 15 layers of packed residue triplets, six are comprised of hydrophobic residues, including two layers of triplet leucines (Figure 5.28A). The remaining nine layers of packed residue triplets are partly hydrophobic, comprised of two hydrophobic residues and one polar residue (Figure 5.28A). Thus, unlike the layers of packed residue stabilizing four-helix SNARE complexes, most of the layers in the BECN2(181-250): 2STX6 SNARE are not completely hydrophobic. 4-helix SNARE complexes have an ionic “0” layer at the center that sets the

register for the packing of the 4 helices[75, 76]. This ionic layer typically consists of three glutamine's from three Q-SNAREs and an arginine from an R-SNARE. The three-helix bundle does not contain this ionic layer. Notably however, each of the three helices contributes a glutamine to the packing interface, Gln 222 from BECN2(181-250) and Gln 197 from each STX6 SNARE, that are arranged one layer apart from each other in this structure (Figure 5.28B), suggesting that a shift in register, stabilized by an arginine from a R-SNARE, would allow these residues to form the "ionic layer". This is consistent with STX6 being classified as a Q-SNARE[80]. Based on the data presented here, we suggest that BECN2 functions as a Q-SNARE in the context of potential SNARE complexes.

5.3.21. Purifications of Point Mutations for MBP-STX6 SNARE and MBP-BECN2(181-250)

In order to assess the importance of the hydrophobic layers in stabilizing the three-helix bundle we individually mutated each of the residues contributing to these layers to aspartates, and assessed the impact on interaction using affinity pulldowns. Each of the six BECN2 mutations; L194D, A197D, L204D, L229D, L236D, and A239D; impacts only one hydrophobic layer, but because the two STX6 chains have anti-parallel arrangements, each of the six STX6 mutations; L173D, V176D, L183D, L208D, L215D, and V218D; impacts the packing of two hydrophobic layers.

Site-directed mutagenesis was used to create each of the L173D, V176D, L183D, L208D, L215D, and V218D mutants in the MBP-STX6 SNARE construct. Each of the mutants were purified using the same protocol as the wild-type MBP-STX6 SNARE. The yields of the pure MBP-STX6 SNARE mutants are worse than wild type, likely due to the mutations destabilizing the protein and therefore making the expression worse (Table 5.11). Similar to wild type, the

SEC chromatograms for each of the mutants have multiple peaks (Figure 5.29). SDS-PAGE shows that in each case the main SEC peak contains the MBP-STX6 SNARE mutant with the peaks and shoulders containing contaminants, most likely degrading protein as it is less stable. The theoretical molecular weight of all of the MBP-STX6 SNARE mutants is 52 kD calculated from the amino acid sequence, showing the mutants behave similar to wild type on SEC.

Table 5.11: Protein yield of single point mutations of the MBP-STX6 SNARE of L173D, V176D, L183D, L208D, L215D, and V218D.

Mutants	Yield
WT	23.4 mg/L
L173D	6.7 mg/L
V176D	12.8 mg/L
L183D	4.6 mg/L
L208D	0.6 mg/L
L215D	4.1 mg/L
V218D	8 mg/L

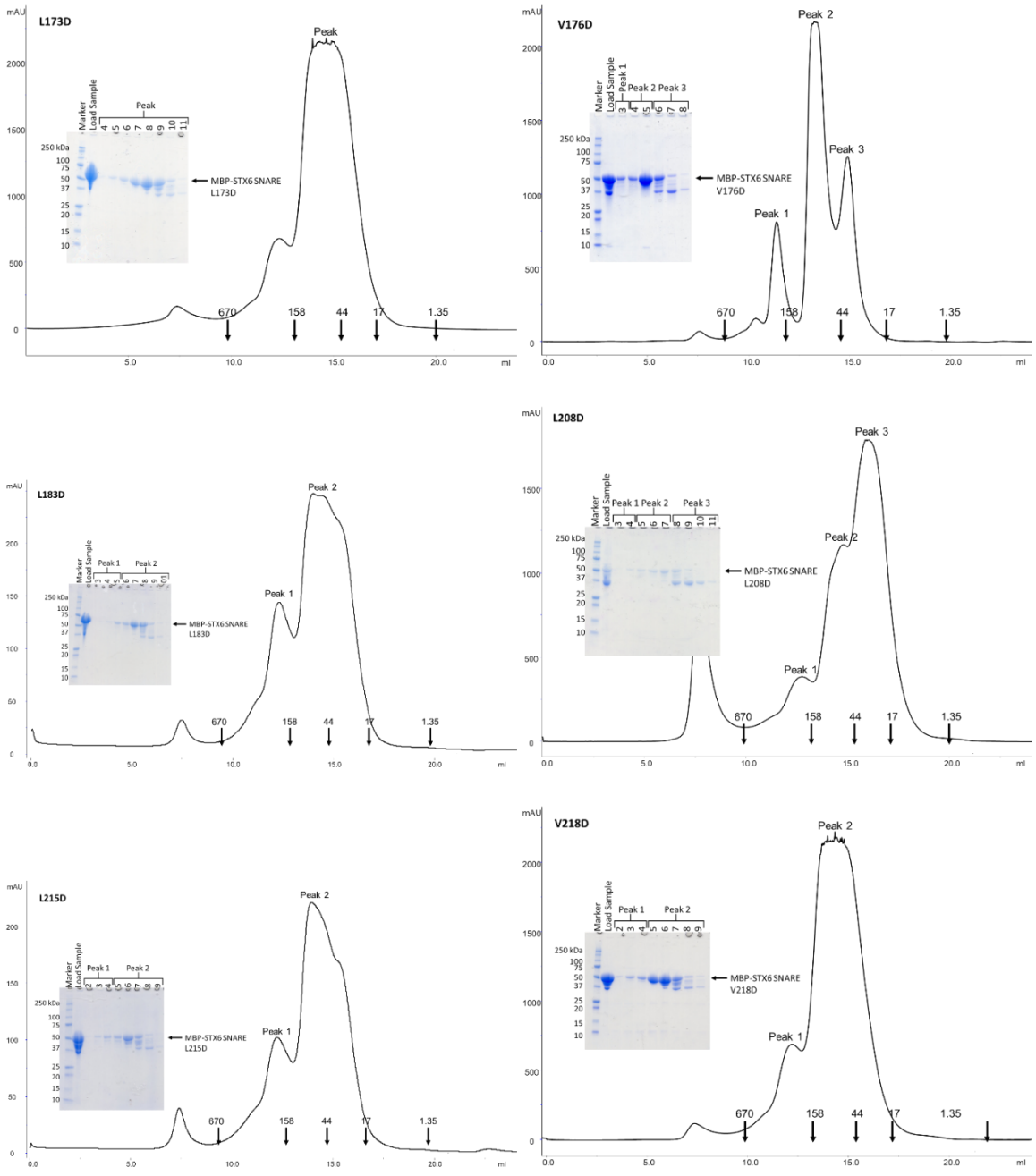

Figure 5.29: Size exclusion chromatogram and the corresponding SDS-PAGE of MBP-STX6 SNARE single point mutations: L173D, V176D, L183D, L208D, L215D, and V218D. The elution positions of SEC Superdex 200 increase 10/300 standards are indicated by arrows.

Site-directed mutagenesis was used to create each of the L194D, A197D, L204D, L229D, L236D, and A239D mutants in the MBP-BECN2(181-250) construct. Each of the mutants were purified using the same protocol as the wild-type MBP-BECN2(181-250). Relative to MBP-

BECN2(181-250), all the mutants, except for the A197D and A239D mutants, had lower yields (Table 5.12), suggesting that the leucines stabilized the protein, likely by stabilizing the homodimer. Similar to wild-type the SEC chromatograms for all of the mutants, have multiple peaks with the main peak containing the MBP-BECN2(181-250) mutants and the other peaks or shoulders containing contaminates and likely degraded protein, as indicated by SDS-PAGE (Figure 5.30). The theoretical molecular weight of all of the MBP-BECN2(181-250) mutants is 49.5 kD calculated from the amino acid sequence.

Table 5.12: Yields of protein of the single point mutations of MBP-BECN2(181-250) L194D, A197D, L204D, L229D, L236D, and A239D.

Mutants	Yield
WT	7.3 mg/L
L194D	4.6 mg/L
A197D	21.1 mg/L
L204D	1.7 mg/L
L229D	1.9 mg/L
L236D	2.8 mg/L
A239D	9.4 mg/L

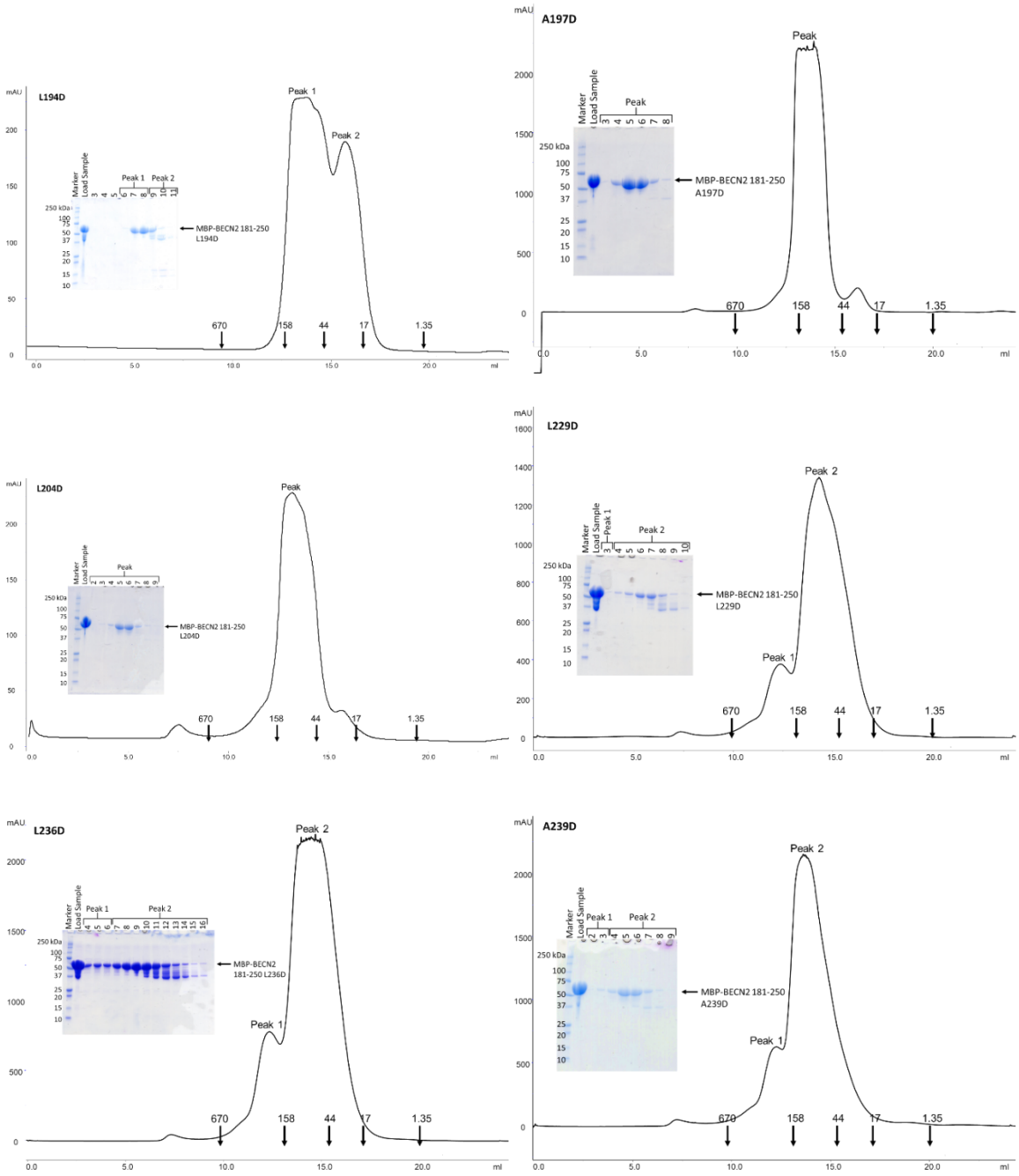

Figure 5.30: Size exclusion chromatogram and the corresponding SDS-PAGE of MBP-BECN2(181-250) single point mutants: L194D, A197D, L204D, L229D, L236D, and A239D. The elution positions of SEC Superdex 200 increase 10/300 standards are indicated by arrows.

5.3.22. Mutations of the Hydrophobic Layers Disrupt the BECN2(181-250): 2STX6 SNARE Interaction

SDS-PAGE analysis of the Ni^{++}-NTA resin affinity pulldowns (Figure 5.31A) demonstrate that, as expected, WT STX6 SNARE pulls-down MBP-tagged BECN2(181-250), and when this eluate is run over amylose resin, MBP-tagged BECN2(181-250) pulls down STX6 SNARE. However, SDS-PAGE indicates that none of the STX6 SNARE mutants pull down BECN2(181-250) (Figure 5.31A), and this is quantitatively verified by the dramatically reduced yield of protein eluted from the Ni^{++}-NTA pulldowns for each of the mutants compared to the wild-type (Table 5.13). Thus, simultaneous disruption of two hydrophobic layers by each STX6 SNARE mutation abrogates formation of the three-helix bundle.

SDS-PAGE analysis of the Ni^{++}-NTA resin affinity pulldowns demonstrate that of the six BECN2(181-250) mutants (Figure 5.31B and Table 5.13), STX6 SNARE does not pull down two BECN2 mutants, L204D and L229D, indicating that these mutations completely disrupt interaction with STX6. Notably, these mutations disrupt the center of the 3-helix bundle. STX6 SNARE weakly pulls down three of the BECN2(181-250)mutants, L194D, A197D, and A239D, but there is minimal co-elution from the amylose resin, indicating that the BECN2:STX6 interaction is substantially weakened by these mutations. Lastly, the L236D mutation also has somewhat reduced pull-down by the STX6 SNARE, followed by reduced co-elution of complex eluted from amylose resin, indicating that this mutation also hampers interaction but not as much as the other mutations.

Together, these results indicate that the hydrophobic layers are important for stabilization of the BECN2(181-250): 2STX6 SNARE 3-helix bundle.

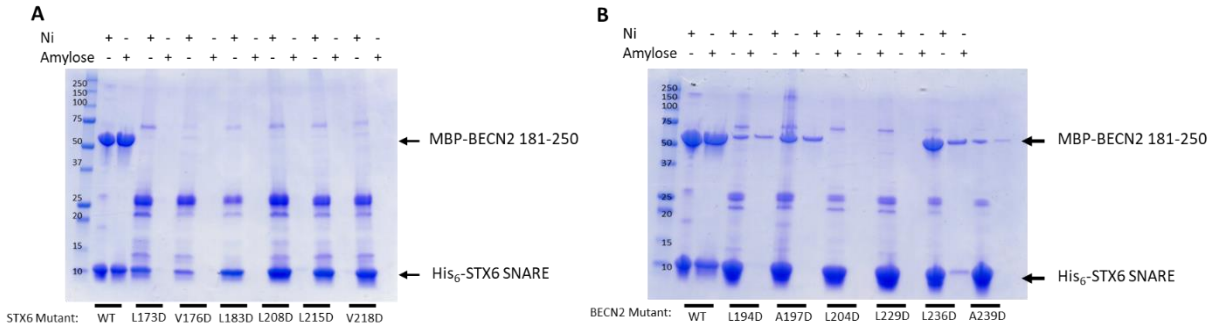

Figure 5.31: Affinity pulldown assays to assess impact of point mutations of hydrophobic layers on the on BECN2(181-250) and STX6 SNARE interaction. A) His_6-STX6 SNARE mutants. B) MBP-BECN2(181-250) mutants. Each mutant is indicated below the gel. The resin used for the pull-down assay is indicated above the gel. Molecular masses for markers run in the first lane are indicated.

Table 5.13: Yield of WT and mutant MBP-BECN2(181-250):His_6-STX6 SNARE complexes after Ni^{++}-NTA affinity pull-down.

Complex	Yield (mg/L cells)
MBP-BECN2(181-250): 2His_6-STX6 SNARE	38.3
MBP-BECN2(181-250): 2His_6-STX6 SNARE L173D	1.6
MBP-BECN2(181-250): 2His_6-STX6 SNARE V176D	1.0
MBP-BECN2(181-250): 2His_6-STX6 SNARE L183D	1.6
MBP-BECN2(181-250): 2His_6-STX6 SNARE L208D	1.5
MBP-BECN2(181-250): 2His_6-STX6 SNARE L215D	3.0
MBP-BECN2(181-250): 2His_6-STX6 SNARE V218D	3.2
MBP-BECN2(181-250) L194D: 2His_6-STX6 SNARE	17.3
MBP-BECN2(181-250) A197D: 2His_6-STX6 SNARE	13.2
MBP-BECN2(181-250) L204D: 2His_6-STX6 SNARE	7.6
MBP-BECN2(181-250) L229D: 2His_6-STX6 SNARE	13.2
MBP-BECN2(181-250) L236D: 2His_6-STX6 SNARE	22.2
MBP-BECN2(181-250) A239D: 2His_6-STX6 SNARE	14.9

5.3.23. Comparison of STX6 SNARE-Containing Early Endosomal Complex and the BECN2(181-250): 2STX6 SNARE Complex

The structure of STX6 SNARE had previously been solved in complex with the SNARE domains of STX13, Vti1a, and VAMP4 (PDB ID: 2NPS). This quaternary SNARE complex mediates early endosomal fusion[74]. We evaluated the individual superposition of the helices of

the BECN2(181-250): 2STX6 SNARE 3-helix bundle on selected helices of the early endosomal SNARE complex. The parallel STX6 SNARE from the BECN2(181-250): 2STX6 SNARE heterotrimer superimposes onto the STX6 SNARE of the early endosomal SNARE complex with an RMSD of 1.108 Å over the 52 Ca atoms superimposed out of a total of 60 Ca atoms, as there may be a slight change in the curvature (Table 5.14, Figure 5.32). Notably, 2931.9 $Å^2$, comprising 48.2% of the total surface area of the STX6 SNARE is buried in the early endosomal complex, which is larger than the 2347.9 $Å^2$ of the STX6 SNARE buried in the 3-helix bundle.

Table 5.14: RMSD upon superposition of selected helices of the BECN2(181-250): 2STX6 SNARE 3-helix bundle onto different helices of the early endosomal SNARE complex.

Helices selected for superposition from				
BECN2(181-250): 2STX6 SNARE 3-helix bundle	Early Endosomal complex	RMSD of overlay of other helixes after superposition indicated:	Number of atoms aligned	RMSD (Å)
Parallel STX6	STX6		52 out of 60	1.108
		Anti STX6 to Vti1a	60 out of 60	2.9
		BECN2 to STX13	62 out of 62	5.2
		BECN2 to VAMP4	58 out of 58	5.7
Anti-parallel STX6	STX6		51 out of 59	1.003
Anti-parallel STX6	Vti1a		49 out of 59	1.857
BECN2	STX13		61 out of 61	2.172
BECN2	VAMP4		61 out of 61	3.444
BECN2 and Parallel STX6	VAMP4 and STX6		117 out of 121	3.354
BECN2 and Parallel STX6	STX13 and STX6		117 out of 121	3.593

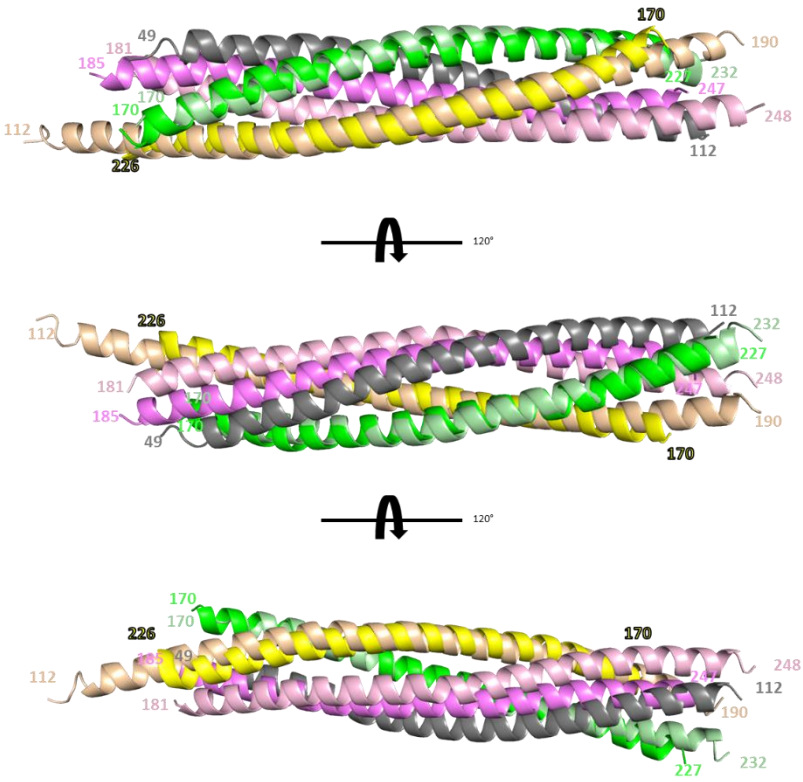

Figure 5.32: Superposition of the BECN2(181-250):STX6 SNARE 3-helix bundle and the early endosomal SNARE complex (PBD ID 2NPS). The three views represent 120° rotations about the X-axis. The BECN2(181-250):STX6 is colored as in Figure 5.23. The early endosomal SNARE complex consists of VAMP4 (gray), Syntaxin 13 (light pink), vti1a (wheat), and STX6 (pale green).

Based on the superposition of the parallel STX6 SNARE from the BECN2(181-250): 2STX6 SNARE 3-helix bundle on the STX6 SNARE of the early endosomal complex, we find that the anti-parallel STX6 SNARE from the BECN2(181-250): 2STX6 SNARE 3-helix bundle closely overlays Vti1a, a Q-SNARE, from the early endosomal SNARE complex with an RMSD of 2.9 Å over 60 Ca atoms (Table 5.14, Figure 5.32). The BECN2(181-250) from the BECN2(181-250): 2STX6 SNARE 3-helix bundle lies in between the STX13, a Q-SNARE, and the VAMP4, an R-SNARE, helices of the early endosomal SNARE complex, albeit somewhat closer to the STX13, with RMSDs of 5.2 Å over 62 Ca atoms and 5.7 Å over Ca atoms respectively (Table 5.14, Figure 5.32).

The anti-parallel STX6 SNARE from the BECN2(181-250): 2STX6 SNARE heterotrimer superimposes onto the STX6 SNARE of the early endosomal SNARE complex with an RMSD of 1.003 Å for 51 Ca atoms superimposed out of a total of 95 Ca atoms (Table 5.14), and onto Vti1a from the early endosomal SNARE complex with an RMSD of 1.857 Å for 49 Ca atoms superimposed out of a total of 59 Ca atoms (Table 5.14). As expected, the anti-parallel STX6 SNARE superimposes best on the STX6 SNARE of the early endosomal complex, and unexpectedly, it superimposes marginally better than the parallel STX6 SNARE (Table 5.14). However, the superimposes of the anti-STX6 SNARE to the STX6 SNARE of the early endosomal SNARE complex cause the parallel STX6 SNARE and the BECN2(181-250) to be anti-parallel to the other helices in the early endosomal SNARE complex. The BECN2(181-250) from the BECN2(181-250): 2STX6 SNARE heterotrimer superimposes onto STX13 and VAMP4 from the early endosomal SNARE complex with RMSDs of 2.172 Å and 3.444 Å respectively, over all 61 Ca atoms available in each case (Table 5.14). This shows that the BECN2(181-250) from the BECN2(181-250): 2STX6 SNARE complex is structurally more similar to STX13 which is a Q-SNARE, rather than to VAMP4 which is an R-SNARE.

We also evaluated the simultaneous superposition of the parallel STX6 SNARE and BECN2(181-250) from the BECN2(181-250): 2STX6 SNARE complex onto the STX6 and either the STX13 or the VAMP4 from the early endosomal complex. The parallel STX6 SNARE and BECN2(181-250) from the BECN2(181-250): 2STX6 SNARE complex superimpose on the early endosomal SNARE complex STX6 and STX13 respectively with an RMSD of 3.354 Å over all 121 Ca atoms available; which is slightly better than the superposition on the early endosomal SNARE complex STX6 and VAMP4 respectively with an RMSD of 3.593 Å over 117 Ca atoms out of the 121 total Ca atoms available (Table 5.14). Thus, it appears likely that

the parallel STX6 SNARE and the BECN2(181-250) in the three-bundle correspond to Q-SNARES in a functional SNARE complex.

A comparison of the packing layers that stabilize the early endosomal complex and the BECN2(181-250): 2STX6 SNARE complex (Figure 5.33) shows that the early endosomal complex has 16 packing layers[74], while the BECN2(181-250): 2STX6 SNARE complex has 15 layers[74]. However, the same 15 STX6 residues contribute to the interface in both complexes. Canonical SNARE complexes have a central ionic "0" layer at layer 0 that consists of three glutamines and one arginine, with each residue contributed by a different helix. The early endosomal SNARE complex does have an ionic layer but contains atypical residues: two glutamines, one each from STX6 SNARE and STX13 SNARE, an arginine from the VAMP4 SNARE, and an aspartate from the vti1a SNARE, instead of a third glutamine (Figure 5.34A). The glutamine from the STX6 SNARE in the early endosomal SNARE complex and the parallel STX6 SNARE in the BECN2(181-250): 2STX6 SNARE complex superimpose well. However, as discussed above, the glutamines from the other two helices are offset by a turn (Figure 5.28B), and so the BECN2(181-250): 2STX6 SNARE 3-helix bundle lacks a proper ionic "0" layer (Figure 5.34B).

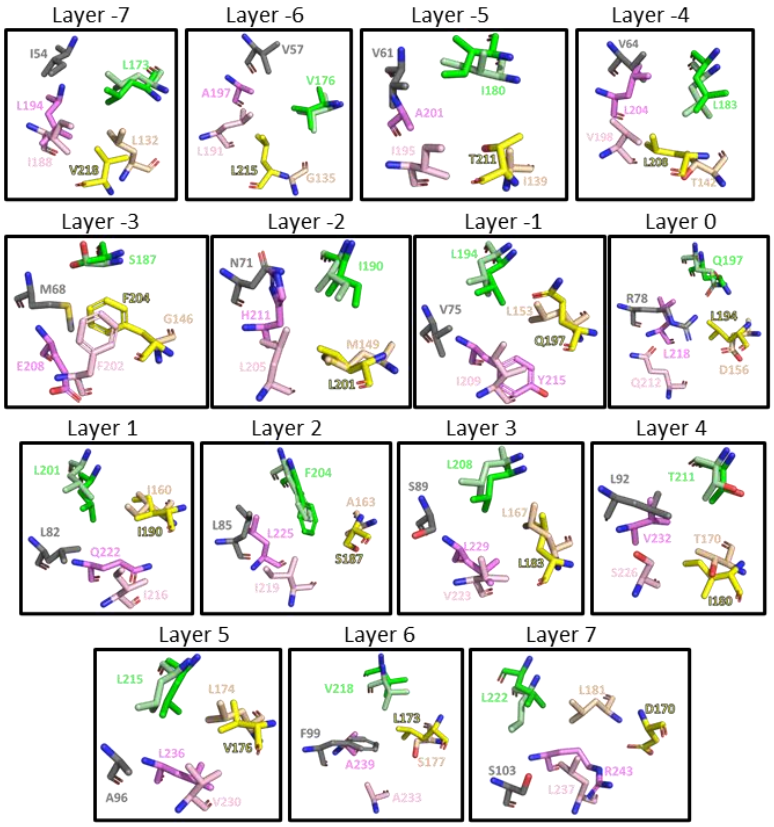

Figure 5.33: Interacting residue layers stabilizing the early endosomal SNARE complex (PBD ID 2NPS) superimposed upon those of the BECN2(181-250):STX6 SNARE 3-helix. Proteins are colored as in Figure 5.31. Interface residues are shown as stick, with atoms colored by type-oxygen: red, nitrogen: blue, sulfur: orange, and carbon: according to protein.

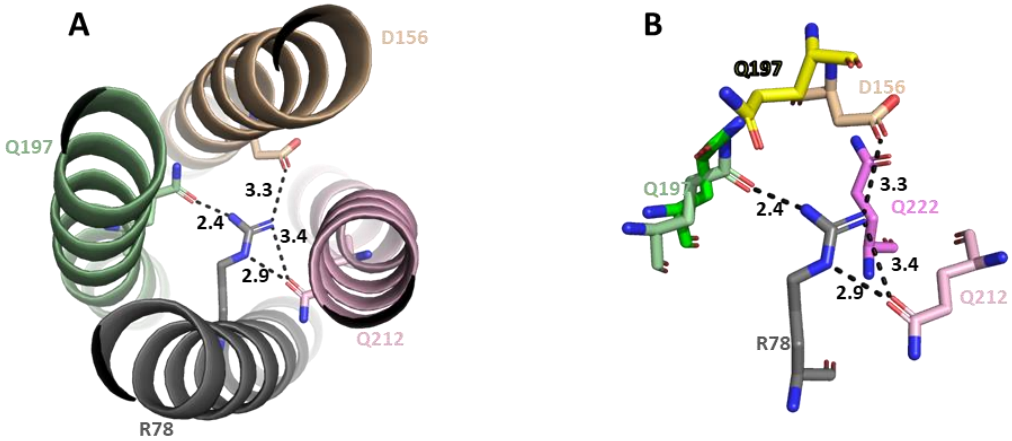

Figure 5.34: The central "0" ionic layer of SNARE bundles. Proteins and atoms are colored as in Figure 5.32. A) The central "0" ionic layer of the early endosomal SNARE complex. Polar interactions are shown as dashed lines and bond lengths are indicated. B) Arrangement of the ionic layer of the early endosomal SNARE complex relative to the three glutamines from the BECN2(181-250):STX6 SNARE complex (shown in Fig. 5.28b).

Seven of the 16 layers stabilizing the early endosomal SNARE complex are completely hydrophobic (layers -7, -6, -5, -1, 1, 2, and 5)[74], compared to six out of 15 layers in the BECN2(181-250): 2STX6 SNARE complex. Three of the hydrophobic layers, corresponding to early endosomal SNARE complex layers -7, -6, and 5, coincide in the two complexes. All the interface residues contributed to the interface by the early endosomal complex STX6 SNARE and the parallel STX6 SNARE from the 3-helix bundle superimpose well. Further, the anti-parallel STX6 SNARE from the BECN2(181-250): 2STX6 SNARE complex closely overlays the vti1a SNARE of the early endosomal complex, and the interface residues from the two helices superimpose fairly well even though the residues themselves are different. Lastly, as the BECN2(181-250) helix from the BECN2(181-250): 2STX6 SNARE complex lies in between STX13 and VAMP4 from the early endosomal SNARE complex, the residues contributed to the interface of both complexes are not only different, but also occupy significantly different positions. Thus, it is likely that the BECN2(181-250): 2STX6 SNARE complex crystallized here serves as a kinetic intermediate in the process of the assembly of a ternary SNARE complex

5.4. Conclusions and Discussion

Our detailed structural and biophysical study paired with our mutational analysis of the interaction of BECN2 and STX6 show how these proteins interact through the BECN2 CCD and STX6 SNARE domains. We show that the STX6 SNARE domain is disordered without a binding partner but becomes helical when in complex with BECN2 CCD or BECN2(181-250). Further, we show that the BECN2 CCD:STX6 SNARE and BECN2(181-250): 2STX6 SNARE complexes have comparable stability, indicating that BECN2 CCD residues preceding residues 181 do not contribute to the interaction with STX6 SNARE. We also find that the complexes are more stable than either the BECN2 CCD, BECN2(181-250) or STX6 SNARE by themselves.

The 3.1 Å X-ray crystal structure of the BECN2 CCD: 2STX6 SNARE complex, clearly indicates that residues 158-185 are disordered, supporting the conclusions drawn from the CD and melting curve experiments. Thus, BECN2(181-250) is the minimal region that interacts with the STX6 SNARE domain.

Crystallizing the complex with the shorter BECN2(181-250) allowed us to improve crystal packing, enabling us to determine the 2.65 Å X-ray crystal structure of the BECN2(181-250): 2STX6 SNARE complex. The complex of BECN2(181-250) and STX6 SNARE forms a heterotrimeric helical bundle with one BECN2(181-250) and two STX6 SNAREs that are anti-parallel to each other. The heterotrimer is stabilized by 15 packing layers, six of which are hydrophobic, including two leucine-only layers. Amongst the hydrophobic residues constituting these layers, we find that aspartate mutagenesis of the hydrophobic residues contributed by STX6 SNARE completely abrogates formation of the 3-helix bundle, likely because each mutation disrupts two interface resiudes. In contrast, amongst the 6 hydrophobic interface BECN2 residues mutated to aspartate, mutating the two most central residues, L204D and L229D, abrogates formation of the 3-helix bundle, while mutating the remaining residues, L194D, A197D, L236D, and A239D, weakens the complex to varying degrees.

STX6 is a Q-SNARE[80] and in the BECN2(181-250): 2STX6 SNARE three-helix bundle, both the parallel and anti-parallel STX6 SNARES contribute Glutamines to the interface. BECN2 in the BECN2(181-250): 2STX6 SNARE also contributes a glutamine to the interface. This strongly suggests that BECN2 acts as a Q-SNARE. However, the 3 glutamines contributed by each helix in this complex are arranged one helical turn apart, with the glutamine contributed by the parallel in STX6 in the center, indicating that this is likely not the arrangement of packing residues that will be found in a functional SNARE complex. Our structural comparisons of the

BECN2(181-250): 2STX6 SNARE three-helical bundle and the STX6 SNARE-containing early endosomal complex also indicate that BECN2 is structurally most similar to a Q-SNARE in that complex. Notably, the electrostatic surface of BECN2(181-250): 2STX6 SNARE heterotrimer is relatively neutral except the central region, which is negatively charged. This strongly supports our conclusion that BECN2 is a Q-SNARE, and that a hitherto unknown R-SNARE would contribute an arginine to the ionic layer to form a more stable 4-helix SNARE complex.

Unlike most SNARE complexes, which are four-helix bundles, the BECN2(181-250): 2STX6 SNARE complex is a three-helix bundle. 3-helix SNARE bundles have previously been formed using optical tweezers to extract the v-SNARE (r-SNARE), synaptobrevin, from a complete 4-helix SNARE bundle, leaving an intact "Target-SNARE" or T-SNARE complex comprised of three t-SNAREs (Q-SNAREs), wherein one helix is provided by STX and two by SNAP25[91, 92]. In that T-SNARE complex, 61 amino acids of the STX were shown to be helical, indicating that the complex is fully folded[93]. Further, addition of the R-SNARE, synaptobrevin, to the 3-helix t-SNARE bundle allows it to rapidly bind or "zip" into the T-SNARE complex from the N-terminus to C-terminus, to reassemble the 4-helical SNARE bundle [91-93]. As the formation of the full SNARE complex leads to the vesicle and target membranes being pulled together, it is likely that the t-SNARES can exist in a pre-formed T-SNARE complex. Thus, our 3-helix BECN2(181-250): 2STX6 SNARE bundle could represent an intermediate T-SNARE complex preceding formation of a full SNARE complex. The orientation and packing of the three helices in the T-SNARE complex is unknown as the structure of this type of complex has not been explored.

To date, anti-parallel helices have not been found in four-helix SNARE bundles whose structures have been determined. However, fluorescence resonance energy transfer experiments

have shown that in solution, 76% of STX and synaptobrevin are in anti-parallel configurations[94]. Importantly, the disassembly factor, ATPase N-ethylmaleimide-sensitive factor, disassembles anti-parallel SNARE configuration faster than the parallel configurations[95], indicating that the parallel configuration is significantly more stable than the antiparallel configuration. Currently, it is thought that the anti-parallel configuration does not lead to membrane fusion, rather it represents an off state or a state that cannot function in membrane fusion[94]. Therefore, our crystallized BECN2(181-250): 2STX6 SNARE 3-helix bundle most likely corresponds to an off-state or transient / intermediate state T-SNARE complex, that would be disassembled during the assembly of a functional 4-helix bundle that leads to the fusion of the membranes.

It is likely that an on-state T-SNARE complex that includes BECN2(181-250) and the STX6 SNARE, would include one helix from each of these proteins as well as another Q-SNARE. A likely candidate for the third t-SNARE is STX5, which has been shown to interact with BECN2. STX5 is also required for the BECN2-mediated degradation of MEKK3, and the knock-down of both STX6 and STX5 completely blocks the degradation of MEKK3[11, 24]. However, there are various other possible candidates. STX7, STX8, VTI1B, and STX17, all of which have been shown to interact with BECN2 in COIP experiments[11, 25], are all potential candidates for the third Q-SNARE. Other possible Q-SNAREs could be the Q-SNAREs that have been shown to interact with STX6, including Vti1a, and STX13[74]. Lastly, other possibilities for Q-SNAREs could be CCDs that has been shown to interact with BECN2 and function in autophagy, including ATG14[20] or UV radiation resistance-associated gene[60].

Formation of a functional 4-helix SNARE complex would require incorporation of an R-SNARE. Perhaps the most likely R-SNARE is VAMP8, which has been shown to interact with BECN2 through CoIPs[11, 25]. VAMP8 has also been found to function in the SNARE complex

which leads to the fusion of the autophagosome to the endolysosome[96]. Other possible candidate R-SNAREs that have been shown to interact with BECN2 include SEC22A, and VAMP7[11, 25]. Possible R-SNAREs that have been shown to interact with STX6 include VAMP4 and VAMP3[97].

Thus, the complex of BECN2(181-250): 2STX6 SNARE is most likely an intermediate of the SNARE complex that facilitates the fusion of ATG9A-bearing vesicles with the growing autophagosome, thereby providing lipids to the autophagosome. ATG9 has been shown to be a lipid scramblase[98], and likely redistributes lipids between the two leaflets of the double-membrane autophagosome. Thus, this newly identified function of BECN2 as a Q-SNARE is critical to building autophagosomes in non-canonical autophagy.

CHAPTER 6. CONCLUSIONS AND FUTURE DIRECTIONS

The work presented in this dissertation aims to understand the interacting partners of the BECN proteins, and how they differ between the BECN proteins, as a foundation to understanding how they function in canonical and non-canonical autophagy. It is important to start understanding why mammals have two BECN homologs, while lower eukaryotes have only one. The focus of the research reported in chapter 2 was to investigate an interacting partner of BECN1 and in chapters 3-5 was to investigate interacting partners of BECN2. The focus of the research reported in chapters 2-4 investigates the interacting partners of the BECN proteins that function in canonical autophagy and chapter 5 investigates an interacting partner of BECN2 that may function in non-canonical autophagy. Overall, this helps us start understanding why mammals have two BECNs instead of one and the role of BECN2 interactions in canonical and non-canonical autophagy.

In chapter 2 it was shown that MBP-BECN1$^{(\Delta 31\text{-}104)AFM}$:M11 complex is able to be used for cryo-EM. Using the complex of MBP-BECN1$^{(\Delta 31\text{-}104)AFM}$:M11 for cryo-EM micrographs were obtained and individual particles were visible, and 2D classes were analyzed. However, the 2D classes didn't match the SAXS envelope previously obtained. Therefore the structure of the MBP-BECN1$^{(\Delta 31\text{-}104)AFM}$:M11 complex was not solved. This work was a continuation of work done by Dr. Yue Li and reported in Dr. Yue Li's dissertation. This work would help explain how M11 inhibits autophagy, as there may be a conformational change that is leading to the down regulation of autophagy. Further work will need to be done to obtain the structure of MBP-BECN1$^{(\Delta 31\text{-}104)AFM}$:M11 in order to understand the possible conformational change that takes place and leads to the down regulations of autophagy. One possible way to get this structure is to attach the protein complex to an antibody.

In chapter 3, the interaction between BECN2 CCD and UVRAG CCD was investigated. BECN2 CCD interacts with UVRAG CCD via affinity pull-downs and initial ITC results also show that BECN2 CCD and UVRAG CCD interact. However, the BECN2 CCD:UVRAG CCD complex fell apart on SEC, therefore further biophysical techniques like SAXS or X-ray crystallography were unable to be pursued. As this research was in progress, Sheuai Wu et al 2018[60] published a paper with the solved structure of UVRAG CCD and BECN1 CCD, which were tethered by a $(Glycine\text{-}Serine)_5$ linker. They were also able to determine the binding affinity of the interaction of UVRAG CCD and BECN1 CCD[60]. As this was published while our research was ongoing, our work was not continued. However, this may show a difference in BECN2 compared to BECN1 as the BECN1 CCD with UVRAG CCD structure was solved but as it was solved with a linker region this could cause the complex to be more favorable. However, it has been shown that the interaction with BECN1 and UVRAG has shown to function in autophagy and that UVRAG is a part of the PI3KC3 complex 2[57-59]. This shows that there is likely a difference in the interaction between UVRAG with either BECN1 or BECN2.

In chapter 4 it was shown that BECN2 CCD interacts with TAB2 CCD. The binding constant was determined of the interaction between BECN2 CCD and TAB2 CCD. Based on the binding constant the BECN2 CCD:TAB2 CCD forms a tighter heterodimer than the BECN2 CCD homodimer. The TAB2 CCD:His_6-BECN2 CCD forms a partially-folded elongated heterodimer. However, diffraction-quality crystals to be used for X-ray crystallography, were not obtained. Therefore, the crystal structure of the BECN2 CCD:TAB2 CCD complex was not solved. This however shows that BECN2 interacts with TAB2 similarly to BECN1 as TAB2 interacts with the CCD of BECN2. As the interaction of BECN1 with TAB2 inhibits autophagy,

this research shows that the interaction between BECN2 and TAB2 may also inhibit autophagy in a similar manner.

Also in chapter 4, it was shown that BECN2 CCD also interacts with TAB3 CCD but not as tight as TAB2 CCD, this was shown by the interaction falling apart over SEC. Therefore, the same biophysical techniques used for the BECN2 CCD:TAB2 CCD interaction were unable to be performed. Initial ITC data were obtained, but this was just preliminary results and would need to be optimized. Therefore, it was found that BECN2 does interact with TAB2 similar to BECN1 but BECN2 does not interact with TAB3 very well unlike BECN1. This shows a difference in the binding partners between BECN1 and BECN2.

In chapter 5 it was shown that BECN2 CCD interacts with STX6 SNARE. STX6 SNARE is disordered by itself but becomes helical when in complex with BECN2 CCD. BECN2 CCD:STX6 SNARE complex is more stable than BECN2 CCD by itself. The structure of the BECN2 CCD:STX6 SNARE complex was solved to a resolution of 3.1 Å and found to form an anti-parallel heterotrimer with one BECN2 CCD and two STX6 SNARE that are anti-parallel to each other. From this structure, we found that residues 158-180 of BECN2 CCD are disordered.

Also in chapter 5, with removal of the disordered residues from BECN2 CCD to make the construct of BECN2(181-250). STX6 SNARE becomes helical when in complex with BECN2(181-250) similar to BECN2 CCD. The complex of BECN2(181-250):STX6 SNARE is more stable than BECN2(181-250) but BECN2(181-250) is less stable than BECN2 CCD. There was an improvement of the crystal structure to a resolution of 2.65 Å from the previous 3.1 Å using the shorter construct of BECN2. The structure of BECN2(181-250):STX6 SNARE also forms an anti-parallel heterotrimer, with one BECN2(181-250) and two STX6 SNARE that are

anti-parallel to each other. In a comparison of the structure of BECN2 CCD:STX6 SNARE and the structure of BECN2(181-250):STX6 SNARE they overlay with an RMSD of 0.286 Å.

Using this structure, it was found that within the core of the helical bundle, there are 15 layers. Of the 15 layers, six are hydrophobic interactions and two of which are leucine-only layers. The effects of the hydrophobic interactions were determined, by doing single-point mutation of the different hydrophobic residues. All of the mutations of SNARE completely disrupt the interaction between BECN2(181-250) and STX6 SNARE. All but one of the mutations for BECN2(181-250) either significantly or completely disrupts the interaction between BECN2(181-250) and STX6 SNARE. It makes sense that the mutations of the STX6 SNARE have a bigger effect on the interaction as one mutation affects two layers, and the mutations of BECN2(181-250) only affect one layer at a time. This shows that the interaction between BECN2(181-250) and STX6 SNARE is mostly hydrophobic.

In chapter 5 it was also investigated on how our complex of BECN2(181-250):STX6 SNARE compares to the structure of the early endosomal SNARE complex. The early endosomal SNARE complex is made of STX6, STX13, vti1a, and VAMP4. The parallel STX6 SNARE from our complex aligns with the STX6 SNARE found in the early endosomal SNARE complex. This leads to the anti-parallel STX6 SNARE following relatively close to the Vti1a SNARE of the early endosomal SNARE complex and the BECN2(181-250) falls in between the other two helices of the early endosomal SNARE complex. As the BECN2(181-250) is aligned closer to the STX13 which is a Q-SNARE and that there is a glutamine that is close to what could be the ionic layer, shows that BECN2(181-250) is acting as a Q-SNARE.

To determine the binding affinity of the BECN2(181-250) and STX6 SNARE interaction, the dissociation of the complex was measured and no heats of dissociation were detected using

ITC. Next the association of the individual proteins were tested and no heats of interaction were detected. This is most likely due to the fact that the interaction is mostly hydrophobic. The binding affinity of the interaction were investigated using MST. As the melting temperature of the complex is ~27 °C, when the IR laser increases the temperature, it may be close to or above the melting temperature making the results inconsistent. So, in an attempt to increase the melting temperature of the proteins by using TFE which did increase the melting temperature. However, the TFE caused the protein to aggregate, and the binding affinities of the interaction between BECN2(181-250) and STX6 SNARE were unable to be obtained. Therefore, the effect of the point mutations on the binding affinity were not able to be determined.

In chapter 5 the structure of BECN2(181-250):STX6 SNARE, is a heterotrimer helical bundle. This could be an example of a T-SNARE complex, which is an intermediate of the full SNARE complex. This possible T-SNARE complex helps show how BECN2(181-250) and STX6 SNARE function in the degradations of proteins through the ATG9A-bearing vesicles through non-canonical autophagy. As this possible T-SNARE complex could being the ATG9A-bearing vesicles to the growing isolation membrane and incorporate lipids into the growing membrane, as ATG9 is a scramblase[98].

To fully understand the function of BECN2(181-250) and STX6 SNARE in non-canonical autophagy the full SNARE complex will need to be solved. To make the full SNARE complex the correct T-SNAREs in the complex will need to be determined, it is possible this could be BECN2, STX6, and STX5. This could help get the T-SNARE complex in a parallel orientation. The missing R-SNARE will also need to be determined, which the possible candidates that have been shown to interact with BECN2 include SEC22A, VAMP7, and VAMP8[25, 74]. Possible R-SNAREs that have been shown to interact with STX6 include VAMP4

and VAMP3[97]. The most likely candidate is VAMP8. This would make the full SNARE complex BECN2, STX6, STX5, and VAMP8. The formation of the full SNARE complex would hopefully form the ionic layer and eliminate the negative charge in the middle region of the BECN2(181-250): 2STX6 SNARE complex.

The interactions that were studied in this dissertation start to help explain BECN2 role in canonical and non-canonical autophagy. This is shown by BECN2 interacting with TAB2 and UVRAG, as both have been shown to function in autophagy. It was shown that BECN2 may function in non-canonical autophagy when interacting with STX6. These studies start to help show the difference between BECN1 and BECN2, as the interacting partners are not the same. UVRAG and TAB3 interact better with BECN1 than BECN2. TAB2 interacts in a similar manner to BECN1 and BECN2. STX6 only interacts with BECN2. This starts showing a difference between BECN1 and BECN2. This may be a start to understanding why mammals have two BECN homologs, when eukaryotes have only one.

REFERENCES

1. Su, M.; Mei, Y.; Sinha, S., Role of the Crosstalk between Autophagy and Apoptosis in Cancer. *Journal of oncology* **2013,** *2013*.

2. Yang, Z.; Klionsky, D. J., Mammalian autophagy: core molecular machinery and signaling regulation. *Current opinion in cell biology* **2010,** *22* (2).

3. Shintani, T.; Klionsky, D. J., Autophagy in health and disease: a double-edged sword. *Science (New York, N.Y.)* **2004,** *306* (5698).

4. Saha, S.; Panigrahi, D. P.; Patil, S.; Bhutia, S. K., Autophagy in health and disease: A comprehensive review. *Biomedicine & pharmacotherapy = Biomedecine & pharmacotherapie* **2018,** *104*.

5. Alicia, M.; Beth, L., Autophagy in C. elegans. **2018**.

6. Parzych, K. R.; Klionsky, D. J., An Overview of Autophagy: Morphology, Mechanism, and Regulation. In *Antioxid Redox Signal*, 2014; Vol. 20, pp 460-73.

7. Aman, Y.; Schmauck-Medina, T.; Hansen, M.; Morimoto, R. I.; Simon, A. K.; Bjedov, I.; Palikaras, K.; Simonsen, A.; Johansen, T.; Tavernarakis, N.; Rubinsztein, D. C.; Partridge, L.; Kroemer, G.; Labbadia, J.; Fang, E. F., Autophagy in healthy aging and disease. *Nature Aging* **2021,** *1* (8), 634-650.

8. Yu, L.; Chen, Y.; Tooze, S. A., Autophagy pathway: Cellular and molecular mechanisms. In *Autophagy*, 2018; Vol. 14, pp 207-15.

9. Dupont, N.; Codogno, P., Non-canonical Autophagy: Facts and Prospects. *Current Pathobiology Reports* **2013,** *1* (4), 263-271.

10. Codogno, P.; Mehrpour, M.; Proikas-Cezanne, T., Canonical and non-canonical autophagy: variations on a common theme of self-eating? *Nature reviews. Molecular cell biology* **2011,** *13* (1).

11. Zhu, M.; Deng, G.; Xing, C.; Nie, G.; Wang, R. F., BECN2 (beclin 2)-mediated non-canonical autophagy in innate immune signaling and tumor development. *Autophagy* **2020,** *16* (12).

12. Liang, X. H.; Kleeman, L. K.; Jiang, H. H.; Gordon, G.; Goldman, J. E.; Berry, G.; Herman, B.; Levine, B., Protection against fatal Sindbis virus encephalitis by beclin, a novel Bcl-2-interacting protein. *J Virol* **1998,** *72* (11), 8586-96.

13. Liang, X. H.; Jackson, S.; Seaman, M.; Brown, K.; Kempkes, B.; Hibshoosh, H.; Levine, B., Induction of autophagy and inhibition of tumorigenesis by beclin 1. *Nature* **1999,** *402*, 672-676.

14. Mei, Y.; Glover, K.; Su, M.; Sinha, S. C., Conformational flexibility of BECN1: Essential to its key role in autophagy and beyond. In *Protein Sci*, 2016; Vol. 25, pp 1767-85.

15. Sinha, S.; Colbert, C. L.; Becker, N.; Wei, Y.; Levine, B., Molecular basis of the regulation of Beclin 1-dependent autophagy by the gamma-herpesvirus 68 Bcl-2 homolog M11. *Autophagy* **2008,** *4* (8).

16. Li, X.; He, L.; Che, K. H.; Funderburk, S. F.; Pan, L.; Pan, N.; Zhang, M.; Yue, Z.; Zhao, Y., Imperfect interface of Beclin1 coiled-coil domain regulates homodimer and heterodimer formation with Atg14L and UVRAG. *Nature communications* **2012,** *3*.

17. Criollo, A.; Niso-Santano, M.; Malik, S. A.; Michaud, M.; Morselli, E.; Mariño, G.; Lachkar, S.; Arkhipenko, A. V.; Harper, F.; Pierron, G.; Rain, J. C.; Ninomiya-Tsuji, J.; Fuentes, J. M.; Lavandero, S.; Galluzzi, L.; Maiuri, M. C.; Kroemer, G., Inhibition of autophagy by TAB2 and TAB3. *The EMBO journal* **2011,** *30* (24).

18. Noda, N. N.; Kobayashi, T.; Adachi, W.; Fujioka, Y.; Ohsumi, Y.; Inagaki, F., Structure of the novel C-terminal domain of vacuolar protein sorting 30/autophagy-related protein 6 and its specific role in autophagy. *The Journal of biological chemistry* **2012,** *287* (20).

19. Glover, K.; Li, Y.; Mukhopadhyay, S.; Leuthner, Z.; Chakravarthy, S.; Colbert, C. L.; Sinha, S. C., Structural transitions in conserved, ordered Beclin 1 domains essential to regulating autophagy. *J Biol Chem* **2017,** *292* (39), 16235-16248.

20. Su, M.; Li, Y.; Wyborny, S.; Neau, D.; Chakravarthy, S.; Levine, B.; Colbert, C. L.; Sinha, S. C., BECN2 interacts with ATG14 through a metastable coiled-coil to mediate autophagy. *Protein Sci* **2017**.

21. He, C. C.; Wei, Y. J.; Sun, K.; Li, B. H.; Dong, X. N.; Zou, Z. J.; Liu, Y.; Kinch, L. N.; Khan, S.; Sinha, S.; Xavier, R. J.; Grishin, N. V.; Xiao, G. H.; Eskelinen, E. L.; Scherer, P. E.; Whistler, J. L.; Levine, B., Beclin 2 Functions in Autophagy, Degradation of G Protein-Coupled Receptors, and Metabolism. *Cell* **2013,** *154* (5), 1085-1099.

22. Dong, X.; Cheng, A.; Zou, Z.; Yang, Y. S.; Sumpter, R. M.; Huang, C. L.; Bhagat, G.; Virgin, H. W.; Lira, S. A.; Levine, B., Endolysosomal trafficking of viral G protein-coupled receptor functions in innate immunity and control of viral oncogenesis. *Proceedings of the National Academy of Sciences of the United States of America* **2016,** *113* (11).

23. Kim, Y. J.; Kong, Q.; Yamamoto, S.; Kuramoto, K.; Huang, M.; Wang, N.; Hong, J. H.; Xiao, T.; Levine, B.; Qiu, X.; Zhao, Y.; Miller, R. J.; Dong, H.; Meltzer, H. Y.; Xu, M.; He, C., An autophagy-related protein Becn2 regulates cocaine reward behaviors in the dopaminergic system. *Science advances* **2021,** *7* (8).

24. Zhu, M.; Deng, G.; Tan, P.; Xing, C.; Guan, C.; Jiang, C.; Zhang, Y.; Ning, B.; Li, C.; Yin, B.; Chen, K.; Zhao, Y.; Wang, H. Y.; Levine, B.; Nie, G.; Wang, R. F.,

Beclin 2 negatively regulates innate immune signaling and tumor development. *The Journal of clinical investigation* **2020,** *130* (10).

25. Deng, G.; Li, C.; Chen, L.; Xing, C.; Fu, C.; Qian, C.; Liu, X.; Wang, H. Y.; Zhu, M.; Wang, R. F., BECN2 (beclin 2) Negatively Regulates Inflammasome Sensors Through ATG9A-Dependent but ATG16L1- and LC3-Independent Non-Canonical Autophagy. *Autophagy* **2022,** *18* (2).

26. Luis. García-Fuentes; Ramiro. Téllez-Sanz; Indalecio. Quesada-Soriano; Carmen. Barón, Thermodynamics of Molecular Recognition by Calorimetry. **2011**.

27. Zhou, X.; Kini, R. M.; Sivaraman, J., Application of isothermal titration calorimetry and column chromatography for identification of biomolecular targets. *Nature protocols* **2011,** *6* (2).

28. Song, C.; Zhang, S.; Huang, H., Choosing a suitable method for the identification of replication origins in microbial genomes. *Frontiers in microbiology* **2015,** *6*.

29. Jerabek-Willemsen, M.; Wienken, C. J.; Braun, D.; Baaske, P.; Duhr, S., Molecular interaction studies using microscale thermophoresis. *Assay and drug development technologies* **2011,** *9* (4).

30. Jerabek-Willemsen, M.; André, T.; Wanner, R.; Roth, H. M.; Duhr, S.; Baaske, P.; Breitsprecher, D., MicroScale Thermophoresis: Interaction analysis and beyond. *Journal of Molecular Structure* **2014,** *1077*, 101-113.

31. Greenfield, N. J., Using circular dichroism spectra to estimate protein secondary structure. *Nature protocols* **2006,** *1* (6).

32. Sreerama, N.; Woody, R. W., Estimation of protein secondary structure from circular dichroism spectra: comparison of CONTIN, SELCON, and CDSSTR methods with an expanded reference set. *Analytical biochemistry* **2000,** *287* (2).

33. Greenfield, N. J., Using circular dichroism collected as a function of temperature to determine the thermodynamics of protein unfolding and binding interactions. *Nature protocols* **2006,** *1* (6).

34. Putnam, C. D.; Hammel, M.; Hura, G. L.; Tainer, J. A., X-ray solution scattering (SAXS) combined with crystallography and computation: defining accurate macromolecular structures, conformations and assemblies in solution. *Quarterly reviews of biophysics* **2007,** *40* (3).

35. Dmitri. I. Svergun; Michel. H. J. Koch, Small-angle scattering studies of biological macromolecules in solution - IOPscience. *Reports on Progress in Physics* **2003,** *66* (10), 1735-1782.

36. Kikhney, A. G.; Svergun, D. I., A practical guide to small angle X-ray scattering (SAXS) of flexible and intrinsically disordered proteins. *FEBS letters* **2015,** *589* (19 Pt A).

37. Franke, D.; Svergun, D. I., DAMMIF, a program for rapid ab-initio shape determination in small-angle scattering. *Journal of applied crystallography* **2009,** *42* (Pt 2).

38. Volkov, V. V.; Svergun, D. I.; IUCr, Uniqueness of ab initio shape determination in small-angle scattering. *Journal of Applied Crystallography* **2003,** *36* (3), 860-864.

39. Kozin, M. B.; Svergun, D. I.; IUCr, Automated matching of high- and low-resolution structural models. *Journal of Applied Crystallography* **2001,** *34* (1), 33-41.

40. Parker, M. W., Protein Structure from X-Ray Diffraction. *Journal of Biological Physics* **2022,** *29* (4), 341-362.

41. M. S. Smyth; J. H. J. Martin, x Ray crystallography. **2000**.

42. Karplus, P. A.; Diederichs, K., Assessing and maximizing data quality in macromolecular crystallography. *Current opinion in structural biology* **2015,** *34*.

43. Taylor, G. L., Introduction to phasing. *Acta crystallographica. Section D, Biological crystallography* **2010,** *66* (Pt 4).

44. Adams, P. D.; Afonine, P. V.; Bunkoczi, G.; Chen, V. B.; Echols, N.; Headd, J. J.; Hung, L. W.; Jain, S.; Kapral, G. J.; Grosse Kunstleve, R. W.; McCoy, A. J.; Moriarty, N. W.; Oeffner, R. D.; Read, R. J.; Richardson, D. C.; Richardson, J. S.; Terwilliger, T. C.; Zwart, P. H., The Phenix software for automated determination of macromolecular structures. *Methods* **2011,** *55* (1), 94-106.

45. Winn, M. D.; Ballard, C. C.; Cowtan, K. D.; Dodson, E. J.; Emsley, P.; Evans, P. R.; Keegan, R. M.; Krissinel, E. B.; Leslie, A. G.; McCoy, A.; McNicholas, S. J.; Murshudov, G. N.; Pannu, N. S.; Potterton, E. A.; Powell, H. R.; Read, R. J.; Vagin, A.; Wilson, K. S., Overview of the CCP4 suite and current developments. *Acta crystallographica. Section D, Biological crystallography* **2011,** *67* (Pt 4).

46. Kleywegt, G. J.; Brünger, A. T., Checking your imagination: applications of the free R value. *Structure (London, England : 1993)* **1996,** *4* (8).

47. Herzik, M. A., Cryo-electron microscopy reaches atomic resolution. *Nature* **2020,** *587* (7832).

48. Milne, J. L.; Borgnia, M. J.; Bartesaghi, A.; Tran, E. E.; Earl, L. A.; Schauder, D. M.; Lengyel, J.; Pierson, J.; Patwardhan, A.; Subramaniam, S., Cryo-electron microscopy--a primer for the non-microscopist. *The FEBS journal* **2013,** *280* (1).

49. Thompson, R. F.; Walker, M.; Siebert, C. A.; Muench, S. P.; Ranson, N. A., An introduction to sample preparation and imaging by cryo-electron microscopy for structural biology. *Methods (San Diego, Calif.)* **2016,** *100*.

50. Doerr, A., Single-particle cryo-electron microscopy. *Nature Methods* **2015,** *13* (1), 23-23.

51. Jasenko. Zivanov; Takanori. Nakane; Sjors. H.W. Scheres, Estimation of High-Order Aberrations and Anisotropic Magnification from Cryo-EM Datasets in RELION-3.1. **2019**.

52. Fernandez-Leiro, R.; Scheres, S. H. W., A pipeline approach to single-particle processing in RELION. *Acta crystallographica. Section D, Structural biology* **2017,** *73* (Pt 6).

53. Pattingre, S.; Tassa, A.; Qu, X.; Garuti, R.; Liang, X. H.; Mizushima, N.; Packer, M.; Schneider, M. D.; Levine, B., Bcl-2 antiapoptotic proteins inhibit Beclin 1-dependent autophagy. *Cell* **2005,** *122* (6).

54. Maiuri, M. C.; Le Toumelin, G.; Criollo, A.; Rain, J. C.; Gautier, F.; Juin, P.; Tasdemir, E.; Pierron, G.; Troulinaki, K.; Tavernarakis, N.; Hickman, J. A.; Geneste, O.; Kroemer, G., Functional and physical interaction between Bcl-X(L) and a BH3-like domain in Beclin-1. *The EMBO journal* **2007,** *26* (10).

55. Kvansakul, M.; Hinds, M. G., Structural biology of the Bcl-2 family and its mimicry by viral proteins. *Cell death & disease* **2013,** *4* (11).

56. Zivanov, J.; Nakane, T.; Forsberg, B. O.; Kimanius, D.; Hagen, W. J.; Lindahl, E.; Scheres, S. H., New tools for automated high-resolution cryo-EM structure determination in RELION-3. **2018**.

57. Afzal, S.; Hao, Z.; Itsumi, M.; Abouelkheer, Y.; Brenner, D.; Gao, Y.; Wakeham, A.; Hong, C.; Li, W. Y.; Sylvester, J.; Gilani, S. O.; Brustle, A.; Haight, J.; You-Ten, A. J.; Lin, G. H.; Inoue, S.; Mak, T. W., Autophagy-independent functions of UVRAG are essential for peripheral naive T-cell homeostasis. *Proc Natl Acad Sci U S A* **2015,** *112* (4), 1119-24.

58. Liang, C.; Feng, P.; Ku, B.; Dotan, I.; Canaani, D.; Oh, B.-H.; Jung, J. U., Autophagic and tumour suppressor activity of a novel Beclin1-binding protein UVRAG. *Nature Cell Biology* **2006,** *8* (7), 688-698.

59. Itakura, E.; Kishi, C.; Inoue, K.; Mizushima, N., Beclin 1 forms two distinct phosphatidylinositol 3-kinase complexes with mammalian Atg14 and UVRAG. *Molecular biology of the cell* **2008,** *19* (12).

60. Wu, S.; He, Y.; Qiu, X.; Yang, W.; Liu, W.; Li, X.; Li, Y.; Shen, H. M.; Wang, R.; Yue, Z.; Zhao, Y., Targeting the potent Beclin 1-UVRAG coiled-coil interaction with designed peptides enhances autophagy and endolysosomal trafficking. *Proceedings of the National Academy of Sciences of the United States of America* **2018,** *115* (25).

61. Takaesu, G.; Kobayashi, T.; Yoshimura, A., TGFβ-activated kinase 1 (TAK1)-binding proteins (TAB) 2 and 3 negatively regulate autophagy. *Journal of biochemistry* **2012,** *151* (2).

62. Besse, A.; Lamothe, B.; Campos, A. D.; Webster, W. K.; Maddineni, U.; Lin, S. C.; Wu, H.; Darnay, B. G., TAK1-dependent signaling requires functional interaction with TAB2/TAB3. *The Journal of biological chemistry* **2007,** *282* (6).

63. Takaesu, G.; Kishida, S.; Hiyama, A.; Yamaguchi, K.; Shibuya, H.; Irie, K.; Ninomiya-Tsuji, J.; Matsumoto, K., TAB2, a novel adaptor protein, mediates activation of TAK1 MAPKKK by linking TAK1 to TRAF6 in the IL-1 signal transduction pathway. *Molecular cell* **2000,** *5* (4).

64. Shibuya, H.; Yamaguchi, K.; Shirakabe, K.; Tonegawa, A.; Gotoh, Y.; Ueno, N.; Irie, K.; Nishida, E.; Matsumoto, K., TAB1: an activator of the TAK1 MAPKKK in TGF-beta signal transduction. *Science (New York, N.Y.)* **1996,** *272* (5265).

65. Ori, D.; Kato, H.; Sanjo, H.; Tartey, S.; Mino, T.; Akira, S.; Takeuchi, O., Essential roles of K63-linked polyubiquitin-binding proteins TAB2 and TAB3 in B cell activation via MAPKs. *Journal of immunology (Baltimore, Md. : 1950)* **2013,** *190* (8).

66. Niso-Santano, M.; Criollo, A.; Malik, S. A.; Michaud, M.; Morselli, E.; Marino, G.; Lachkar, S.; Galluzzi, L.; Maiuri, M. C.; Kroemer, G., Direct molecular interactions between Beclin 1 and the canonical NFkappaB activation pathway. *Autophagy* **2012,** *8* (2), 268-70.

67. Kirby, N.; Cowieson, N.; Hawley, A. M.; Mudie, S. T.; McGillivray, D. J.; Kusel, M.; Samardzic-Boban, V.; Ryan, T. M.; IUCr, Improved radiation dose efficiency in solution SAXS using a sheath flow sample environment. *Acta Crystallographica Section D: Structural Biology* **2016,** *72* (12), 1254-1266.

68. Franke, D.; Jeffries, C. M.; Svergun, D. I., Correlation Map, a goodness-of-fit test for one-dimensional X-ray scattering spectra. *Nature methods* **2015,** *12* (5).

69. Hopkins, J. B.; Gillilan, R. E.; Skou, S., BioXTAS RAW: improvements to a free open-source program for small-angle X-ray scattering data reduction and analysis. *Journal of applied crystallography* **2017,** *50* (Pt 5).

70. Durand, D.; Vivès, C.; Cannella, D.; Pérez, J.; Pebay-Peyroula, E.; Vachette, P.; Fieschi, F., NADPH oxidase activator p67(phox) behaves in solution as a multidomain protein with semi-flexible linkers. *Journal of structural biology* **2010,** *169* (1).

71. Svergun, D. I.; IUCr, Determination of the regularization parameter in indirect-transform methods using perceptual criteria. *Journal of Applied Crystallography* **1992,** *25* (4), 495-503.

72. Glatter, O., A new method for the evaluation of small-angle scattering data. *Journal of Applied Crystallography* **1977,** *10* (5), 415-421.

73. Jumper, J.; Evans, R.; Pritzel, A.; Green, T.; Figurnov, M.; Ronneberger, O.; Tunyasuvunakool, K.; Bates, R.; Žídek, A.; Potapenko, A.; Bridgland, A.; Meyer, C.; Kohl, S. A. A.; Ballard, A. J.; Cowie, A.; Romera-Paredes, B.; Nikolov, S.; Jain, R.;

Adler, J.; Back, T.; Petersen, S.; Reiman, D.; Clancy, E.; Zielinski, M.; Steinegger, M.; Pacholska, M.; Berghammer, T.; Bodenstein, S.; Silver, D.; Vinyals, O.; Senior, A. W.; Kavukcuoglu, K.; Kohli, P.; Hassabis, D., Highly accurate protein structure prediction with AlphaFold. *Nature* **2021,** *596* (7873), 583-589.

74. Zwilling, D.; Cypionka, A.; Pohl, W. H.; Fasshauer, D.; Walla, P. J.; Wahl, M. C.; Jahn, R., Early endosomal SNAREs form a structurally conserved SNARE complex and fuse liposomes with multiple topologies. *The EMBO journal* **2007,** *26* (1).

75. Fasshauer, D.; Sutton, R. B.; Brunger, A. T.; Jahn, R., Conserved structural features of the synaptic fusion complex: SNARE proteins reclassified as Q- and R-SNAREs. *Proceedings of the National Academy of Sciences of the United States of America* **1998,** *95* (26).

76. Sutton, R. B.; Fasshauer, D.; Jahn, R.; Brunger, A. T., Crystal structure of a SNARE complex involved in synaptic exocytosis at 2.4 Å resolution. *Nature* **1998,** *395* (6700), 347-353.

77. Hanson, P. I.; Heuser, J. E.; Jahn, R., Neurotransmitter release - four years of SNARE complexes. *Current opinion in neurobiology* **1997,** *7* (3).

78. Wendler, F.; Tooze, S., Syntaxin 6: the promiscuous behaviour of a SNARE protein. *Traffic (Copenhagen, Denmark)* **2001,** *2* (9).

79. Watson, R. T.; Pessin, J. E., Functional cooperation of two independent targeting domains in syntaxin 6 is required for its efficient localization in the trans-golgi network of 3T3L1 adipocytes. *The Journal of biological chemistry* **2000,** *275* (2).

80. Bock, J. B.; Lin, R. C.; Scheller, R. H., A new syntaxin family member implicated in targeting of intracellular transport vesicles. *The Journal of biological chemistry* **1996,** *271* (30).

81. Sreerama, N., CDPro- A Software Package for Analyzing Protein CD Spectra. 2004.

82. Franke, D.; Jeffries, C. M.; Svergun, D. I., Correlation Map, a goodness-of-fit test for one-dimensional X-ray scattering spectra. *Nat Methods* **2015,** *12* (5), 419-22.

83. Durand, D.; Vivès, C.; Cannella, D.; Pérez, J.; Pebay-Peyroula, E.; Vachette, P.; Fieschi, F., NADPH oxidase activator p67phox behaves in solution as a multidomain protein with semi-flexible linkers. *J Struct Biol* **2010,** *169* (1), 45-53.

84. Svergun, D. I., Determination of the regularization parameter in indirect-transform methods using perceptual criteria. *J. Appl. Crystallogr.* **1992,** *25* (4), 495-503.

85. Glatter, O., A new method for the evaluation of small-angle scattering data. *J Appl Crystallogr* **1977,** *10* (5), 415-421.

86. Rambo, R. P.; Tainer, J. A., Accurate assessment of mass, models and resolution by small-angle scattering. *Nature* **2013,** *496* (7446), 477-481.

87. Liebschner, D.; Afonine, P. V.; Baker, M. L.; Bunkóczi, G.; Chen, V. B.; Croll, T. I.; Hintze, B.; Hung, L. W.; Jain, S.; McCoy, A. J.; Moriarty, N. W.; Oeffner, R. D.; Poon, B. K.; Prisant, M. G.; Read, R. J.; Richardson, J. S.; Richardson, D. C.; Sammito, M. D.; Sobolev, O. V.; Stockwell, D. H.; Terwilliger, T. C.; Urzhumtsev, A. G.; Videau, L. L.; Williams, C. J.; Adams, P. D., Macromolecular structure determination using X-rays, neutrons and electrons: recent developments in Phenix. *Acta crystallographica. Section D, Structural biology* **2019,** *75* (Pt 10).

88. Schrodinger, L., The PyMOL Molecular Graphics System, Version 2.0. 2015 November.

89. Krissinel, E.; Henrick, K., Inference of macromolecular assemblies from crystalline state. *Journal of molecular biology* **2007,** *372* (3).

90. Mason, J. M.; Arndt, K. M., Coiled coil domains: stability, specificity, and biological implications. *Chembiochem : a European journal of chemical biology* **2004,** *5* (2).

91. Pobbati, A. V.; Stein, A.; Fasshauer, D., N- to C-terminal SNARE complex assembly promotes rapid membrane fusion. *Science (New York, N.Y.)* **2006,** *313* (5787).

92. Yoon, T. Y.; Munson, M., SNARE complex assembly and disassembly. *Current biology : CB* **2018,** *28* (8).

93. Gao, Y.; Zorman, S.; Gundersen, G.; Xi, Z.; Ma, L.; Sirinakis, G.; Rothman, J. E.; Zhang, Y., Single reconstituted neuronal SNARE complexes zipper in three distinct stages. *Science (New York, N.Y.)* **2012,** *337* (6100).

94. Weninger, K.; Bowen, M. E.; Chu, S.; Brunger, A. T., Single-molecule studies of SNARE complex assembly reveal parallel and antiparallel configurations. *Proceedings of the National Academy of Sciences of the United States of America* **2003,** *100* (25).

95. Choi, U. B.; Zhao, M.; White, K. I.; Pfuetzner, R. A.; Esquivies, L.; Zhou, Q.; Brunger, A. T., NSF-mediated disassembly of on- and off-pathway SNARE complexes and inhibition by complexin. *eLife* **2018,** *7*.

96. Diao, J.; Liu, R.; Rong, Y.; Zhao, M.; Zhang, J.; Lai, Y.; Zhou, Q.; Wilz, L. M.; Li, J.; Vivona, S.; Pfuetzner, R. A.; Brunger, A. T.; Zhong, Q., ATG14 promotes membrane tethering and fusion of autophagosomes to endolysosomes. *Nature* **2015,** *520* (7548).

97. Nozawa, T.; Minowa-Nozawa, A.; Aikawa, C.; Nakagawa, I., The STX6-VTI1B-VAMP3 complex facilitates xenophagy by regulating the fusion between recycling endosomes and autophagosomes. *Autophagy* **2017,** *13* (1).

98. Matoba, K.; Kotani, T.; Tsutsumi, A.; Tsuji, T.; Mori, T.; Noshiro, D.; Sugita, Y.; Nomura, N.; Iwata, S.; Ohsumi, Y.; Fujimoto, T.; Nakatogawa, H.; Kikkawa, M.;

Noda, N. N., Atg9 is a lipid scramblase that mediates autophagosomal membrane expansion. *Nature Structural & Molecular Biology* **2020,** *27* (12), 1185-1193.